# Lorenz gauge gravitational self-force calculations of eccentric binaries using a frequency domain procedure

Thomas Osburn, Erik Forseth, and Charles R. Evans

*Department of Physics and Astronomy, University of North Carolina,*
*Chapel Hill, North Carolina 27599, USA*

Seth Hopper

*Max-Planck-Institut für Gravitationsphysik, Albert-Einstein-Institut,*
*Am Mühlenberg 1, D-14476 Golm, Germany*

We present an algorithm for calculating the metric perturbations and gravitational self-force for extreme-mass-ratio inspirals (EMRIs) with eccentric orbits. The massive black hole is taken to be Schwarzschild, and metric perturbations are computed in Lorenz gauge. The perturbation equations are solved as coupled systems of ordinary differential equations in the frequency domain. Accurate local behavior of the metric is attained through use of the method of extended homogeneous solutions, and mode-sum regularization is used to find the self-force. We focus on calculating the self-force with sufficient accuracy to ensure its error contributions to the phase in a long-term orbital evolution will be $\delta\Phi \lesssim 10^{-2}$ rad. This requires the orbit-averaged force to have fractional errors $\lesssim 10^{-8}$ and the oscillatory part of the self-force to have errors $\lesssim 10^{-3}$ (a level frequently easily exceeded). Our code meets this error requirement in the oscillatory part, extending the reach to EMRIs with eccentricities of $e \lesssim 0.8$, if augmented by use of fluxes for the orbit-averaged force, or to eccentricities of $e \lesssim 0.5$ when used as a stand-alone code. Further, we demonstrate accurate calculations up to orbital separations of $a \simeq 100M$, beyond that required for EMRI models and useful for comparison with post-Newtonian theory. Our principal developments include (1) use of fully constrained field equations, (2) discovery of analytic solutions for even-parity static modes, (3) finding a preconditioning technique for outer homogeneous solutions, (4) adaptive use of quad precision, (5) jump conditions to handle near-static modes, and (6) a hybrid scheme for high eccentricities.

## I. INTRODUCTION

Merging compact binaries are thought to be a promising source of gravitational waves that may be found by ground-based or future space-based detectors. Theoretical models play a role in the experimental efforts, both in assisting detection and in allowing binary parameter estimation. Three principal theoretical approaches exist, numerical relativity [1,2], post-Newtonian (PN) theory [3], and gravitational self-force (GSF) calculations [4–6], with the effective-one-body formalism providing a synthesis of the three [7–9]. The GSF approach is relevant when the binary mass ratio $\varepsilon$ is sufficiently small that the motion and field of the smaller mass can be treated in a perturbation expansion. In this black hole perturbation theory, the background field is that of the heavier stationary black hole, and the zeroth-order motion of the small mass is a geodesic in this background. Then the perturbation in the metric is calculated to first order in the mass ratio, and the action of the field of the small body back on its own motion is computed (i.e., the first-order GSF) [10,11]. In principle, the calculation proceeds to second order [12,13] and beyond. Over the past 15 years, a number of key formal developments have been established [10,11,14–17].

Work on the GSF approach has been motivated in part by prospects of detecting extreme-mass-ratio inspirals (EMRIs) using a space-based gravitational wave detector like LISA or eLISA [18–20]. For a LISA-like detector with $f_{\min} \simeq 10^{-4}$ Hz, an EMRI consists of a small compact object of mass $\mu \simeq 1 - 10 M_\odot$ (neutron star or black hole) in orbit about a supermassive black hole (SMBH) of mass $M \sim 10^5 - 10^7 M_\odot$. The mass ratio would lie in the range $\varepsilon = \mu/M \simeq 10^{-7} - 10^{-4}$, small enough to allow a gradual, adiabatic inspiral and provide a natural application of perturbation theory. As the EMRI crosses the detector pass band prior to merger, its orbital motion accumulates a total change in phase of order $\varepsilon^{-1} \sim 10^4 - 10^7$ rad.

Less extreme mass ratios may also be important. A class of intermediate mass black holes (IMBHs) may exist with masses $M \sim 10^2 - 10^4 M_\odot$. These are suggested [21] by observations of ultraluminous x-ray sources and by theoretical simulations of globular cluster dynamical evolution. Stellar mass black holes or neutron stars spiralling into IMBHs with masses $M \sim 50 - 350 M_\odot$, referred to as intermediate-mass-ratio inspirals (IMRIs), would lie in the pass band of Advanced LIGO and are potentially promising sources [22,23]. An IMRI might also result from binaries composed of an IMBH and a SMBH [23],

which would appear as an eLISA source. While IMRIs execute fewer total orbits (i.e., $\varepsilon^{-1} \sim 10^2 - 10^3$) than EMRIs in making, say, a decade of frequency change, the theoretical approach is nearly the same. Detection of E/IMRIs would represent a strong field test of general relativity, and measurement of the primary's multipole structure would confirm or not the presence of a Kerr black hole [22,24,25].

In tandem with the more formal GSF developments have come a host of practical numerical calculations. The dominant approach to date takes the small body to be a point mass [5], computes the metric perturbation (MP) in the time domain (TD) [26–29] or frequency domain (FD) [30–32], and obtains a finite self-force from the divergent retarded field by mode-sum regularization [14,27,30,32–37]. Work on the gauge-dependent GSF has benefitted from analogous scalar field models [38–40]. Applications to Kerr EMRIs, both with scalar and gravitational self-force, have been made [41–48]. Availability of analytic mode-sum regularization parameters [49,50] has been beneficial. Calculations of perturbations and the GSF have now been made with very high accuracy, arbitrary precision arithmetic [51–54], allowing detailed comparison with PN theory (see also Refs. [30,55]). Finally, alternative means of calculating the self-force, both effective source calculations [56–58] and direct Green function calculations [59–61], are being developed.

This paper reports the development of a method and computer code for accurately calculating the GSF of Schwarzschild EMRIs with eccentric orbits. We use a point mass description for the stress-energy tensor of the small body and work in Lorenz gauge. Tensor spherical harmonic and Fourier decomposition are used, and the MP amplitudes are computed initially in the FD. These amplitudes are then transferred to the TD using a generalization of the method of extended homogeneous solutions (EHS) [31,40] for systems of equations [32,34,37,62,63]. The GSF is then calculated using standard mode-sum regularization. Our code was developed over the past several years and was reported in a series of talks at the 15th, 16th, and 17th Capra meetings [63]. A similar effort by a group in Southampton, initiated earlier [32] but developed in part concurrently with ours, has been reported in full elsewhere [37].

Our use of Lorenz gauge in the FD and generalization of EHS is in common with Ref. [37]. The FD is used to achieve high accuracy, and the method of EHS circumvents the Gibbs phenomenon in returning to the TD. We calculate also the "geodesic self-force;" that is, the GSF as a function of time along an undisturbed geodesic orbit. The intent is to provide GSF curves at points that densely cover a region of orbital parameter space (parametrized by eccentricity $e$ and dimensionless semilatus rectum $p$). As shown in Ref. [36], these data can then serve as an interpolated input to an osculating orbits evolution code.

Our approach is distinguished, however, in several respects. We devise and use here a fully constrained system of equations for even parity, as well as use the comparable system [37] for odd parity. We have found and use a set of analytic solutions for even-parity static modes, which complement published solutions [64] for odd parity. Particular attention is paid to accurately calculating near-static modes that occur for certain orbital parameters that produce a near resonance between the radial $\Omega_r$ and azimuthal $\Omega_\varphi$ orbital frequencies (see Fig. 1). To compute this subset of modes accurately, we resort to occasional (more expensive) use of 128-bit arithmetic (i.e., quad precision). This has two effects. First, we are able to trade some computational speed for more uniform accuracy across $e$ and $p$ space. Second, the technique significantly expands the region of $e$ and $p$ space within which the GSF can be computed accurately. For a given $l$ and $m$ mode, there will exist a harmonic $n$ that produces the lowest magnitude frequency, $\omega_{mn} = m\Omega_\varphi + n\Omega_r$. When a mode exists with frequency at or below $|\omega| < 10^{-4}M^{-1}$, we switch the critical parts of the computation over to quad precision. Furthermore, there is an added device that can be used for this single $(l, m, n)$ mode—we can eliminate part of the integration by using the jump conditions to normalize the mode. This procedure increases accuracy and restores some computational speed. With these techniques we are able to extend the reach of the code in computing the GSF to wider orbital separations, out to $p \lesssim 100$, and to higher eccentricities, reaching as high as $e \lesssim 0.8$ with acceptable errors when all available techniques are used.
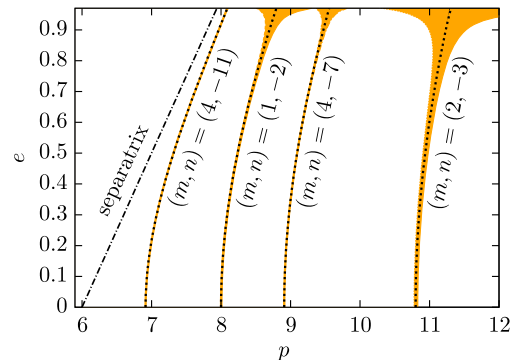


FIG. 1 (color online). Orbital parameter space, resonances, and regions with near-static modes. Relativistic definitions of semi-latus rectum $p$ and eccentricity $e$ are adopted [Eq. (2.5)]. Dotted curves indicate, as in Ref. [37], a closed orbit with the ratio $\Omega_\varphi/\Omega_r$ being a rational number. On any such curve, there exists a static mode $\omega_{mn} = m\Omega_\varphi + n\Omega_r = 0$ for indicated $m$ and $n$. Within the vicinity of these curves, these modes will be nearly static. For near-static modes with frequencies below $|\omega| < 10^{-4}M^{-1}$ (shaded region), we use 128-bit floating point arithmetic for part of the mode calculation. Our calculations are extended to frequencies as small as $|\omega| < 10^{-6}M^{-1}$, which exist in regions narrower than the dotted curves.

The accuracy criteria we adopt in this paper stem from envisioned use of computed inspirals and resulting waveforms in the matched filtering applications of gravitational wave detectors. A detector like eLISA [4,23] would employ template matching to separate individual sources and extract physical parameters from events buried in detector noise. To take full advantage of a signal when doing parameter matching [22,24,25], theoretical waveform phases must be sufficiently accurate that they do not contribute dephasing errors and thus degrade available signal-to-noise ratios [6,25,65]. The oscillations within the gravitational waveform will depend upon the orbital motion. For Schwarzschild EMRIs there are cumulative radial $\Phi_r = \chi_p(T)$ and azimuthal $\Phi_\varphi = \varphi_p(T)$ orbital phases (here $T \sim M^2/\mu$ is the cumulative time in the inspiral, and see Sec. II A for discussion of eccentric orbital motion). For schematic purposes, we simply take here the radial phase as a proxy for the waveform phase. Further, we assume that theoretical orbital phase uncertainties should be no larger than $\delta\Phi_r \simeq 0.01$ rad over a cumulative phase in the inspiral of as much as $\Phi_r \sim 10^6$ (for an EMRI) (see the discussion in Ref. [6]). Thus, the GSF and inspiral calculation should have fractional errors in the phase of order $10^{-8}$.

The GSF is often split into dissipative and conservative parts [65]. It is useful to also split the dissipative part into orbit-averaged and oscillatory parts. The orbit-averaged, dissipative GSF (i.e., energy and angular momentum fluxes to infinity and down the horizon) produces secular changes that drive the adiabatic inspiral. For a small mass ratio $\varepsilon$, the inspiral will schematically accumulate an orbital phase of

$$\Phi_r = \kappa_0(e,p,\eta)\frac{1}{\varepsilon} + \kappa_1(e,p,\eta) + \kappa_2(e,p,\eta)\varepsilon + \cdots, \quad (1.1)$$

where $e$ and $p$ are orbital parameters when the EMRI enters a detector pass band and $\eta$ is the ratio between ingress frequency $f_i$ and egress (or merger) frequency $f_e$. The $\kappa$'s are dimensionless functions of order unity that do not depend on $\varepsilon$. We are here assuming a Schwarzschild E/IMRI and absence of Kerr transient resonances [66]. Also beyond our present concern are the recently recognized effects of resonances in Schwarzschild EMRIs [67], which appear to come in at order $\varepsilon$ (i.e., produce contributions to $\kappa_2$). The orbit-averaged, dissipative part of the first-order GSF will determine $\kappa_0$. The rest of the first-order GSF, the oscillatory part of the dissipative piece and the (oscillatory) conservative part, contribute to $\kappa_1$. This term in $\Phi_r$ is of order unity and represents the post-1-adiabatic correction [65]. The implications for our work are this: if we require $\delta\Phi_r \simeq 10^{-2}$, we must compute the orbit-averaged first-order GSF with fractional errors at or below $\epsilon_0 \simeq 10^{-8} \lesssim \varepsilon\delta\Phi_r$ and compute the oscillatory parts with fractional errors of order $\epsilon_1 \simeq 10^{-3} \lesssim \delta\Phi_r$ or less. The retarded MPs themselves must be known even more

accurately, since mode-sum regularization is a numerically subtractive procedure.

Ultimately these contributions to $\kappa_1$ are necessary but not sufficient. It has long been understood that $\kappa_1$ also depends on the orbit-averaged part of the second-order GSF [12,17,65,68–70], which our code (and the one described in Ref. [37]) does not calculate. Moreover, there is expected to be an error in computing $\kappa_1$ by using FD methods and the "geodesic" GSF. In curved space, the real GSF will depend upon the entire past history of the particle's motion and the self-consistently evolved retarded field. In the geodesic approximation, there is no encoding of the prior history of an inspiral. For adiabatic inspiral the discrepancy is expected to appear at a relative order of $\varepsilon$ (thus in $\kappa_1$) [71]. It was stressed in Ref. [72] that this discrepancy could be assessed by comparing a self-consistent TD self-force calculation with an osculating orbits evolution using a FD-derived geodesic self-force. Such calculations are now in progress [73,74], pitting a scalar field self-consistent TD evolution against an osculating orbits inspiral driven by a geodesic scalar self-force calculation. Preliminary results [75] show small differences that are (so far) nearly indistinguishable from errors in the TD evolution.

Achievable GSF accuracy will depend on orbital parameters, particularly the eccentricity. Theoretical studies suggest that EMRIs may form via several mechanisms [23]. The standard channel involves weak two-body relaxation within the nuclear star cluster that scatters a compact object into a high eccentricity orbit about a SMBH. It is then captured by the SMBH through successive bursts of GW emission near pericenter, a process referred to as one-body inspiral [76]. These stars are captured initially in very high eccentricity orbits, which then proceed to circularize as the orbit shrinks. For $M \simeq 3 \times 10^6 M_\odot$, EMRIs formed in this way will have a distribution of eccentricities peaked about $e \simeq 0.7$ (and a maximum of $e \simeq 0.81$) as they enter the eLISA pass band (see Ref. [76] and its Fig. 4). Because of the likelihood that EMRIs will have high eccentricities, we have focused on extending the ability of our code to calculate up to $e \simeq 0.8$.

An alternative EMRI formation channel posits that compact *binaries* may scatter into high eccentricity orbits about the SMBH, with the binary being subsequently tidally disrupted. The dissolution of the binary may then inject a compact object into orbit, which will typically be less eccentric, about the SMBH. These EMRIs will subsequently have nearly circular orbits by the time they enter the eLISA pass band [23]. As Fig. 1 makes clear, there is less likelihood of encountering troublesome near-static modes at low eccentricity, and our code correspondingly has higher accuracy and speed in these cases.

This paper is organized as follows. In Sec. II we review the formalism for calculating the first-order MPs and the GSF for bound eccentric orbits on Schwarzschild. There we establish our notation for bound geodesic motion, our

convention for spherical harmonic decomposition, and the definition of MP amplitudes and give the coupled MP equations in Lorenz gauge. We also show in Sec. II how the size of these systems of coupled equations can be reduced, from seven down to four equations for even parity and from three down to two equations for odd parity, using the gauge conditions. These fully constrained equations are the ones we solve numerically, deriving the remaining MP amplitudes from the gauge conditions. In Sec. III we outline how we apply the method of EHS to coupled systems of equations. In Sec. IV, where the heart of our numerical method is presented, we provide a road map and details on how various classes of Fourier-harmonic modes are solved. These include low-order ($l = 0, 1$) modes, static modes, and near-static modes. Particularly worth noting is our new analytic solution for even-parity static modes (Sec. IV C) and various procedures for coping with near-static modes (Secs. IV A and IV B). Section V gives our numerical results. There we compare our computed GSF to values given in Ref. [37] for a particular orbit and provide tables of GSF values, including estimated digits of accuracy, for a broader set of orbital parameters (see also Appendix D). We show how the GSF errors vary smoothly as we range over orbital parameter space, while the speed of the algorithm changes more abruptly as it copes with difficult modes. We also discuss how flux calculations may be combined with the computed oscillatory part of the GSF to obtain sufficient accuracy for high eccentricity orbits in long-term orbit integrations, a subject we expect to return to in a later paper. Finally, we relegate to Appendix A some details on expansions that are used to set accurate boundary conditions on mode functions at large $r$ and near the horizon, to Appendix B some details on the expansions from which analytic solutions are derived for static modes, and to Appendix C the form of certain force terms used in the mode-sum regularization procedure.

Throughout this paper we set $c = G = 1$ and use metric signature $(- + + +)$ and sign conventions of Misner, Thorne, and Wheeler [77]. Our notation for metric perturbation amplitudes and source terms largely follows that of Martel and Poisson [78] (see also Ref. [31]). In particular, while general coordinate indices are denoted by greek letters $\alpha, \beta, \mu, \nu, \ldots$, it is useful to consider a split of the four-dimensional manifold into $\mathcal{M}^2 \times \mathcal{S}^2$ and adopt lowercase latin letters $a, b, c, \ldots$ for indices associated with coordinates $t$ and $r$ and capital latin letters $A, B, C, \ldots$ for the angular coordinates $\theta$ and $\varphi$ and associated indices.

## II. FORMALISM

### A. Bound orbits on a Schwarzschild background

We consider in this paper generic bound motion of a point particle of mass $\mu$ around a Schwarzschild black hole of mass $M$ under the assumption that $\mu/M \ll 1$. We use

Schwarzschild coordinates $x^\mu = (t, r, \theta, \varphi)$, in which the line element takes the standard form

$$ds^2 = -f dt^2 + f^{-1} dr^2 + r^2 (d\theta^2 + \sin^2\theta d\varphi^2), \quad (2.1)$$

where $f(r) = 1 - 2M/r$.

Let the worldline of the particle be $x_p^\alpha(\tau) = [t_p(\tau), r_p(\tau), \theta_p(\tau), \varphi_p(\tau)]$, with proper time $\tau$. In this paper a subscript $p$ indicates a field evaluated at the location of the particle. The 4-velocity is $u^\alpha = dx_p^\alpha/d\tau$. Without loss of generality, the motion is confined to the equatorial plane, $\theta_p(\tau) = \pi/2$. At zeroth order the motion is geodesic in the static background, and the geodesic equations yield immediate first integrals. This allows us to write the 4-velocity as

$$u^\alpha = \left( \frac{\mathcal{E}}{f_p}, u^r, 0, \frac{\mathcal{L}}{r_p^2} \right), \quad (2.2)$$

where $\mathcal{E}$ and $\mathcal{L}$ are the constant specific energy and specific angular momentum, respectively. Bound orbits have $\mathcal{E} < 1$ and require at least $\mathcal{L} > 2\sqrt{3}M$ for two turning points to exist. The constraint $u^\alpha u_\alpha = -1$ yields an expression for the radial coordinate velocity,

$$\dot{r}_p^2(t) = f_p^2 \left( 1 - \frac{U_p^2}{\mathcal{E}^2} \right), \quad (2.3)$$

where

$$U^2(r, \mathcal{L}^2) \equiv f(r) \left( 1 + \frac{\mathcal{L}^2}{r^2} \right), \quad (2.4)$$

and a dot indicates differentiation with respect to coordinate time.

While eccentric orbits on Schwarzschild can be parametrized by $\mathcal{E}$ and $\mathcal{L}$, alternative pairs of parameters can be chosen. For example, we can use instead the (dimensionless) semilatus rectum $p$ and the eccentricity $e$ (see Refs. [34,79]). A third choice is the pericentric and apocentric radii, $r_{\min}$ and $r_{\max}$. These various parameters are related by the following equations:

$$p = \frac{2 r_{\max} r_{\min}}{M(r_{\max} + r_{\min})}, \qquad e = \frac{r_{\max} - r_{\min}}{r_{\max} + r_{\min}}, \quad (2.5)$$

$$r_{\max} = \frac{pM}{1 - e}, \qquad r_{\min} = \frac{pM}{1 + e}, \quad (2.6)$$

and

$$\mathcal{E}^2 = \frac{(p - 2)^2 - 4e^2}{p(p - 3 - e^2)}, \qquad \mathcal{L}^2 = \frac{p^2 M^2}{p - 3 - e^2}. \quad (2.7)$$

To avoid a plunging orbit, the inner turning point must lie outside the maximum of the effective potential $U^2$, which implies another inequality, $p > 6 + 2e$. The boundary $p = 6 + 2e$ of these innermost stable orbits is the separatrix indicated in Fig. 1.

Numerical integration of the trajectory employs an alternate curve parameter, $\chi$, in which the radial position on the orbit is given a Keplerian-appearing form [80],

$$r_p(\chi) = \frac{pM}{1 + e\cos\chi}, \qquad (2.8)$$

where $\chi$ differs in general from the true anomaly $\varphi$. One radial libration makes a change $\Delta\chi = 2\pi$. The orbital equations then take the form

$$\frac{dt_p}{d\chi} = \frac{r_p(\chi)^2}{M(p - 2 - 2e\cos\chi)}\left[\frac{(p-2)^2 - 4e^2}{p - 6 - 2e\cos\chi}\right]^{1/2},$$

$$\frac{d\varphi_p}{d\chi} = \left[\frac{p}{p - 6 - 2e\cos\chi}\right]^{1/2},$$

$$\frac{d\tau_p}{d\chi} = \frac{Mp^{3/2}}{(1 + e\cos\chi)^2}\left[\frac{p - 3 - e^2}{p - 6 - 2e\cos\chi}\right]^{1/2}, \qquad (2.9)$$

with the use of $\chi$ removing singularities in the differential equations at the radial turning points (see Ref. [79]). Integrating the first of these equations provides the fundamental frequency and period of radial motion,

$$\Omega_r \equiv \frac{2\pi}{T_r}, \qquad T_r \equiv \int_0^{2\pi}\left(\frac{dt_p}{d\chi}\right)d\chi. \qquad (2.10)$$

Integrating the second equation determines the azimuthal advance. The average angular frequency $d\varphi_p/dt$ is found by integrating over a complete radial oscillation:

$$\Omega_\varphi \equiv \frac{1}{T_r}\int_0^{T_r}\left(\frac{d\varphi_p}{dt}\right)dt. \qquad (2.11)$$

In general $\Omega_r \neq \Omega_\varphi$, except in the Newtonian limit.

## B. First-order metric perturbation equations in Lorenz gauge

The finite mass of the small body induces a first-order perturbation $p_{\mu\nu}$ in the background metric $g_{\mu\nu}$: $g_{\mu\nu} = g_{\mu\nu} + p_{\mu\nu}$. Using the trace reverse $\bar{p}_{\mu\nu} = p_{\mu\nu} - \frac{1}{2}g_{\mu\nu}p$ (with $p = p_{\alpha\beta}g^{\alpha\beta}$), linearizing the Einstein equations, and imposing the Lorenz gauge condition

$$\bar{p}^{\mu\nu}{}_{|\nu} = 0 \qquad (2.12)$$

yields the first-order field equations for the MPs:

$$^4\Box\bar{p}_{\mu\nu} + 2R^\alpha{}_\mu{}^\beta{}_\nu\bar{p}_{\alpha\beta} = -16\pi T_{\mu\nu}. \qquad (2.13)$$

Here, a stroke $|\mu$ (or $\nabla_\mu$) indicates covariant differentiation with respect to $g_{\mu\nu}$ and $^4\Box = g^{\mu\nu}\nabla_\mu\nabla_\nu$. Additionally, $R^\alpha{}_{\mu\beta\nu}$ is the Riemann tensor associated with $g_{\mu\nu}$. Adopting a point particle description, the stress-energy tensor in Eq. (2.13) is

$$T^{\mu\nu}(x^\alpha) = \mu\int\frac{u^\mu u^\nu}{\sqrt{-g}}\delta^4[x^\alpha - x_p^\alpha(\tau)]d\tau. \qquad (2.14)$$

## C. Spherical harmonic decomposition

Our convention for tensor spherical harmonics and notation for MP amplitudes follows that of Martel and Poisson [78], a modification of the original notation of Regge and Wheeler [81]. (An alternative notation is found in Refs. [27,37,64].) The convention we use leaves all tensor harmonics orthogonal and clarifies the distinction between even-parity and odd-parity amplitudes. Odd-parity perturbations are expanded in terms of $X_A^{lm}$ and $X_{AB}^{lm}$, while even-parity perturbations use $Y^{lm}$, $Y_A^{lm}$, and $Y_{AB}^{lm}$:

$$p_{ab} = \sum_{lm}h_{ab}^{lm}Y^{lm},$$

$$p_{aB} = \sum_{lm}(j_a^{lm}Y_B^{lm} + h_a^{lm}X_B^{lm}),$$

$$p_{AB} = \sum_{lm}[r^2(K^{lm}\Omega_{AB}Y^{lm} + G^{lm}Y_{AB}^{lm}) + h_2^{lm}X_{AB}^{lm}]. \qquad (2.15)$$

The stress-energy tensor is also decomposed and following Ref. [78] has even-parity projections

$$Q_{lm}^{ab} = 8\pi\int T^{ab}\bar{Y}^{lm}d\Omega,$$

$$Q_{lm}^a = \frac{8\pi r^2}{\lambda + 1}\int T^{aB}\bar{Y}_B^{lm}d\Omega,$$

$$Q_{lm}^\flat = 8\pi r^2\int T^{AB}\Omega_{AB}\bar{Y}^{lm}d\Omega,$$

$$Q_{lm}^\sharp = \frac{8\pi r^4}{\lambda(\lambda + 1)}\int T^{AB}\bar{Y}_{AB}^{lm}d\Omega \qquad (2.16)$$

and odd-parity projections

$$P_{lm}^a = \frac{8\pi r^2}{\lambda + 1}\int T^{aB}\bar{X}_B^{lm}d\Omega,$$

$$P_{lm} = \frac{4\pi r^4}{\lambda(\lambda + 1)}\int T^{AB}\bar{X}_{AB}^{lm}d\Omega. \qquad (2.17)$$

The overbar here indicates the complex conjugate and $\lambda \equiv (l + 2)(l - 1)/2$. The sharp ($\sharp$) and flat ($\flat$) superscripts merely distinguish two distinct scalar projections. These source terms are given explicitly in Sec. V of Ref. [31].

## D. Lorenz gauge equations for MP amplitudes

Applying these projections to (2.13) yields coupled sets of field equations in $t$ and $r$ for the MP amplitudes.

Likewise (2.12) provides a set of Lorenz gauge conditions on the amplitudes. Lorenz gauge gives each of the ten field equations a hyperbolic form, and the principal part of the wave operator in each equation can be compactly expressed using the $1+1$ dimensional d'Alembertian

$$\Box \equiv -\partial_t^2 + f\partial_r(f\partial_r) = -\partial_t^2 + \partial_{r_*}^2, \qquad (2.18)$$

where $r_*$ is the tortoise coordinate

$$r_* = r + 2M \ln\left(\frac{r}{2M} - 1\right). \qquad (2.19)$$

The seven even-parity and three odd-parity Lorenz gauge field equations are well-posed hyperbolic systems, but the Lorenz gauge conditions (three even parity and one odd parity) force constraints on the initial conditions. These *unconstrained* field equations, along with the Bianchi identities, ensure that the gauge conditions, if fixed initially, are satisfied subsequently. We present the unconstrained equations first and then introduce modified *constrained* systems. Equations in this subsection are in TD form but can be converted to FD form as discussed in Sec. III A. In what follows all $l$ and $m$ indices on MP and source amplitudes are suppressed for brevity unless otherwise noted.

### 1. Unconstrained Lorenz gauge field equations

The seven even-parity unconstrained Lorenz gauge equations are

$$\Box h_{tt} + \frac{2(r-4M)f}{r^2}\partial_r h_{tt} + \frac{4Mf}{r^2}\partial_t h_{tr} + \frac{2M(3M-2r)f^2}{r^4}h_{rr} + \frac{4Mf^2}{r^3}K + \frac{2(M^2-r^2f)-2\lambda r^2 f}{r^4}h_{tt} = -fQ^{rr} - f^2 Q^\flat - f^3 Q^{tt},$$

$$\Box h_{tr} + \frac{2f^2}{r}\partial_r h_{tr} + \frac{2Mf}{r^2}\partial_t h_{rr} + \frac{2M}{r^2 f}\partial_t h_{tt} + \frac{4(\lambda+1)f}{r^3}j_t - \frac{4(M-r)^2 + 2\lambda r^2 f}{r^4}h_{tr} = 2fQ^{tr},$$

$$\Box h_{rr} + \frac{2f}{r}\partial_r h_{rr} + \frac{4M}{r^2 f}\partial_t h_{tr} + \frac{2M(3M-2r)}{r^4 f^2}h_{tt} + \frac{4(r-3M)}{r^3}K + \frac{8(\lambda+1)f}{r^3}j_r + \frac{2(r-M)(7M-3r)-2\lambda r^2 f}{r^4}h_{rr}$$
$$= Q^\flat - \frac{1}{f}Q^{rr} - fQ^{tt},$$

$$\Box j_t - \frac{2Mf}{r^2}\partial_r j_t + \frac{2Mf}{r^2}\partial_t j_r + \frac{2f^2}{r}h_{tr} - \frac{2f^2 + 2\lambda f}{r^2}j_t = f^2 Q^t,$$

$$\Box j_r + \frac{2Mf}{r^2}\partial_r j_r + \frac{2M}{r^2 f}\partial_t j_t + \frac{2f^2}{r}h_{rr} - \frac{2f}{r}K + \frac{2\lambda f}{r}G - \frac{4f^2 + 2(\lambda+1)f}{r^2}j_r = -Q^r,$$

$$\Box K + \frac{2f^2}{r}\partial_r K - \frac{2(3M-r)f^2}{r^3}h_{rr} + \frac{2M}{r^3}h_{tt} - \frac{4(\lambda+1)f^2}{r^3}j_r - \frac{4f^2 + 2\lambda f}{r^2}K = Q^{rr} - f^2 Q^{tt},$$

$$\Box G + \frac{2f^2}{r}\partial_r G + \frac{4f^2}{r^3}j_r - \frac{2\lambda f}{r^2}G = -\frac{f}{r^2}Q^\sharp. \qquad (2.20)$$

The three odd-parity parts of the field satisfy a separate unconstrained set of equations in Lorenz gauge:

$$\Box h_t - \frac{2Mf}{r^2}\partial_r h_t + \frac{2Mf}{r^2}\partial_t h_r - \frac{2f^2 + 2\lambda f}{r^2}h_t = f^2 P^t,$$

$$\Box h_r + \frac{2Mf}{r^2}\partial_r h_r + \frac{2M}{r^2 f}\partial_t h_t + \frac{2\lambda f}{r^3}h_2$$
$$+ \frac{2(4M-3r)f - 2\lambda r f}{r^3}h_r = -P^r,$$

$$\Box h_2 - \frac{2f^2}{r}\partial_r h_2 + \frac{4f^2}{r}h_r + \frac{2f(r-4M) - 2\lambda r f}{r^3}h_2 = -2fP. \qquad (2.21)$$

### 2. Lorenz gauge conditions

The Lorenz gauge conditions (2.12) separate into even- and odd-parity equations when expanded in spherical harmonics. For even parity there are three coupled gauge conditions,

$$f\partial_r h_{tr} - \frac{f}{2}\partial_t h_{rr} - \partial_t K - \frac{1}{2f}\partial_t h_{tt} + \frac{2(r-M)}{r^2}h_{tr}$$
$$- \frac{2(\lambda+1)}{r^2}j_t = 0,$$

$$-\frac{1}{f}\partial_t h_{tr} + \frac{f}{2}\partial_r h_{rr} - \partial_r K + \frac{1}{2f}\partial_r h_{tt} + \frac{2(r-M)}{r^2}h_{rr}$$
$$- \frac{2}{r}K - \frac{2(\lambda+1)}{r^2}j_r = 0,$$

$$f\partial_r j_r - \frac{1}{f}\partial_t j_t - \frac{f}{2}h_{rr} + \frac{1}{2f}h_{tt} + \frac{2(r-M)}{r^2}j_r - \lambda G = 0, \qquad (2.22)$$

while in odd parity there is just one condition,

$$f\partial_r h_r - \frac{1}{f}\partial_t h_t + \frac{2(r-M)}{r^2}h_r - \frac{\lambda}{r^2}h_2 = 0. \qquad (2.23)$$

### 3. Fully constrained field equations

While the unconstrained equations (2.20) and (2.21) might be solved numerically, in practice we have found it more efficient and accurate to use the gauge conditions (2.22) and (2.23) to produce reduced order systems of constrained equations. To do this we rewrite the gauge conditions (2.22) and (2.23) as expressions for the four

amplitudes $j_t$, $j_r$, $G$, and $h_2$. These are used, as necessary, to eliminate their appearance in six of the equations in the sets (2.20) and (2.21)—specifically those equations with wave operators acting on $h_{tt}$, $h_{tr}$, $h_{rr}$, $K$, $h_t$, and $h_r$. These six equations, four even parity and two odd parity, once modified only reference these remaining amplitudes. Once the constrained equations are solved, the eliminated fields, $j_t$, $j_r$, $G$, and $h_2$, are recovered via the gauge conditions.

We find the system of four constrained even-parity equations,

$$\Box h_{tt} + \frac{2(r-4M)f}{r^2}\partial_r h_{tt} + \frac{4Mf}{r^2}\partial_t h_{tr} + \frac{2M(3M-2r)f^2}{r^4}h_{rr} + \frac{4Mf^2}{r^3}K + \frac{2(M^2-r^2f)-2\lambda r^2 f}{r^4}h_{tt} = -fQ^{rr} - f^2 Q^\flat - f^3 Q^{tt},$$

$$\Box h_{tr} + \frac{4f^2}{r}\partial_r h_{tr} + \frac{4M-r}{r^2 f}\partial_t h_{tt} + \frac{(4M-r)f}{r^2}\partial_r h_{rr} - \frac{2f}{r}\partial_t K + \frac{4M(M-r)-2\lambda r^2 f}{r^4}h_{tr} = 2fQ^{tr},$$

$$\Box h_{rr} + \frac{4(r-M)f}{r^2}\partial_r h_{rr} + \frac{2}{r}\partial_r h_{tt} - \frac{4f}{r}\partial_r K + \frac{4(3M-r)}{r^2 f}\partial_t h_{tr} + \frac{2M(3M-2r)}{r^4 f^2}h_{tt} + \frac{4(M-r)}{r^3}K + \frac{2(M-r)^2-2\lambda r^2 f}{r^4}h_{rr}$$

$$= -\frac{1}{f}Q^{rr} + Q^\flat - fQ^{tt},$$

$$\Box K + \frac{4f^2}{r}\partial_r K - \frac{f}{r}\partial_r h_{tt} - \frac{f^3}{r}\partial_r h_{rr} + \frac{2f}{r}\partial_t h_{tr} + \frac{2M}{r^3}h_{tt} - \frac{2(r+M)f^2}{r^3}h_{rr} - \frac{2\lambda f}{r^2}K = -f^2 Q^{tt} + Q^{rr}, \qquad (2.24)$$

and the following system of two constrained odd-parity equations:

$$\Box h_t - \frac{2Mf}{r^2}\partial_r h_t + \frac{2Mf}{r^2}\partial_t h_r - \frac{2f^2 + 2\lambda f}{r^2}h_t = f^2 P^t,$$

$$\Box h_r + \frac{2(r-M)f}{r^2}\partial_r h_r - \frac{2(r-3M)}{r^2 f}\partial_t h_t$$

$$-\frac{2f^2 + 2\lambda f}{r^2}h_r = -P^r. \qquad (2.25)$$

These six equations, supplemented with the gauge conditions (2.22) and (2.23), are satisfied by the MPs in Lorenz gauge. However, as discussed in Sec. III, to find solutions numerically, we cast these equations into the FD, reducing them to large sets of ordinary differential equations. Furthermore, in certain special cases [i.e., low-order ($l = 0, 1$) modes and static ($\omega = 0$) modes], some MP amplitudes cease to be defined or the systems of equations reduce further in size, or both. Section IV discusses these special cases, each of which merits unique numerical treatment.

### E. Self-force and mode-sum regularization

Once the Lorenz gauge equations in the preceding section are solved using causal boundary conditions (i.e., outgoing waves at infinity and downgoing waves at the horizon), the MP amplitudes are used to reassemble the

retarded field $p_{\mu\nu}^{\rm ret}$. The full retarded field is divergent at the location of the point mass, precisely where its action back on the particle's motion must be determined. Regularization is required, and the mode-sum regularization (MSR) procedure of Barack and Ori [14] is commonly used (see, e.g., early use [38] with a scalar field and for the GSF in Lorenz gauge [4,27,34]). To discuss MSR it is useful to consider the decomposition discovered by Detweiler and Whiting [15] that splits the retarded MP within a normal neighborhood of the particle [5] into regular (R) and singular (S) parts:

$$p_{\mu\nu}^{\rm ret} = p_{\mu\nu}^R + p_{\mu\nu}^S. \qquad (2.26)$$

The singular part has a divergence that captures the singular behavior of the retarded field and satisfies the same inhomogeneous field equations (2.13), but through design (i.e., appropriate boundary conditions) does not contribute at all to the self-force. The regular part, in contrast, is a solution to the homogeneous first-order field equations and is entirely responsible for the self-force. Applying the self-force, the corrected motion can be regarded as forced, nongeodesic motion in the background spacetime. With the Detweiler and Whiting split, the motion can also be viewed as geodesic in the corrected metric $g_{\mu\nu} + p_{\mu\nu}^R$. In either viewpoint the self-force becomes a term in the equations of motion found from calculating

$$F_R^\alpha = \mu k^{\alpha\beta\gamma\delta} \bar{p}_{\beta\gamma|\delta}^R, \qquad (2.27)$$

which is evaluated at the particle, $x^\alpha = x_p^\alpha(\tau)$. Here, the trace-reversed MP is used, and the projection operator is

$$k^{\alpha\beta\gamma\delta}(x_p) = \frac{1}{2} g^{\alpha\delta} u^\beta u^\gamma - g^{\alpha\beta} u^\gamma u^\delta - \frac{1}{2} u^\alpha u^\beta u^\gamma u^\delta$$
$$+ \frac{1}{4} u^\alpha g^{\beta\gamma} u^\delta + \frac{1}{4} g^{\alpha\delta} g^{\beta\gamma}. \qquad (2.28)$$

At this point, $k^{\alpha\beta\gamma\delta}$ is defined only at the particle's location (though below we discuss broadening its definition so it can be evaluated off the worldline). Its form ensures orthogonality $F_R^\alpha u_\alpha = 0$. The same operator may be applied to $p_{\mu\nu}^{\text{ret}}$ and $p_{\mu\nu}^S$ to define the retarded and singular self-forces,

$$F_{\text{ret}}^\alpha = \mu k^{\alpha\beta\gamma\delta} \bar{p}_{\beta\gamma|\delta}^{\text{ret}}, \qquad F_S^\alpha = \mu k^{\alpha\beta\gamma\delta} \bar{p}_{\beta\gamma|\delta}^S, \qquad (2.29)$$

both of which diverge at $x^\alpha = x_p^\alpha(\tau)$. Formally, the regular part is formed through the subtraction $F_R^\alpha = F_{\text{ret}}^\alpha - F_S^\alpha$.

However, since both $F_{\text{ret}}^\alpha$ and $F_S^\alpha$ are infinite at the location of interest, a straightforward subtraction is not possible.

The central idea of MSR is to decompose the components of $F_{\text{ret}}^\alpha$ and $F_S^\alpha$ into sums over scalar multipole modes $F_{\text{ret}}^{\alpha l'}$ and $F_S^{\alpha l'}$, with every mode being finite at the location of the particle. (We use $l'$ and $m'$ to distinguish from the $l$ and $m$ of our tensor spherical harmonic decomposition.) Then the subtraction can be made mode by mode. There is a subtlety in the decomposition, however, since the operator $k^{\alpha\beta\gamma\delta}$ (and therefore the self-force) is only defined at this stage at the location of the particle. To generate a spherical harmonic decomposition, we must choose a way to extend $k^{\alpha\beta\gamma\delta}$ off of the worldline. Following Ref. [34] we define $k^{\alpha\beta\gamma\delta}(x; x_p)$ at field point $x$, when the particle is at $x_p$, to have the value given from Eq. (2.28) with $g^{\mu\nu}$ evaluated at $x$ and $u^\alpha$ evaluated at $x_p$. Later, in Eq. (2.33), when we reexpand our tensor harmonics as sums of scalar harmonics, this choice ensures a finite coupling of $l$ modes for each $l'$.

The mode-sum expansion for $F_S^\alpha$ can be written in the form

$$F_S^\alpha = \sum_{l'=0}^\infty \left[ \left( l' + \frac{1}{2} \right) F_{[-1]}^\alpha + F_{[0]}^\alpha + \frac{F_{[2]}^\alpha}{(l' - \frac{1}{2})(l' + \frac{3}{2})} + \frac{F_{[4]}^\alpha}{(l' - \frac{3}{2})(l' - \frac{1}{2})(l' + \frac{3}{2})(l' + \frac{5}{2})} + \cdots \right], \qquad (2.30)$$

where the coefficients $F_{[-1]}^\alpha$, $F_{[0]}^\alpha$, $F_{[2]}^\alpha$, ... are the $l'$-independent *regularization parameters* (RPs), which depend only upon position in the eccentric orbit. (We use the notation of Heffernan *et al.* [49] for the RPs.) Then, the mode-sum formula

$$F_R^\alpha = \sum_{l'=0}^\infty \left[ F_{\text{ret}}^{\alpha l'} - \left( l' + \frac{1}{2} \right) F_{[-1]}^\alpha - F_{[0]}^\alpha - \frac{F_{[2]}^\alpha}{(l' - \frac{1}{2})(l' + \frac{3}{2})} - \frac{F_{[4]}^\alpha}{(l' - \frac{3}{2})(l' - \frac{1}{2})(l' + \frac{3}{2})(l' + \frac{5}{2})} - \cdots \right] \qquad (2.31)$$

determines the regularized self-force. The first two RPs, $F_{[-1]}^\alpha$ and $F_{[0]}^\alpha$, for the GSF on a Schwarzschild background were originally given by Barack *et al.* [82]. Indeed, only these first two parameters are needed to obtain convergence. From the structure of the $l'$-dependent denominator terms, all of the succeeding terms each converge to zero as $l' \to \infty$. However, since the series with only $F_{[-1]}^\alpha$ and $F_{[0]}^\alpha$ converges slowly ($\sim 1/l'_{\text{max}}$), higher-order RPs are important for hastening convergence when the sum is truncated at some finite $l'_{\text{max}}$. Heffernan *et al.* [49] have calculated the higher-order coefficients $F_{[2]}^\alpha$ and $F_{[4]}^\alpha$ for the GSF, and their use (along with numerically fitting to even higher order) greatly improves convergence.

As described above, MSR requires an expansion of the full retarded self-force $F_{\text{ret}}^\alpha$ as a sum over scalar spherical harmonic modes $F_{\text{ret}}^{\alpha l'}$. In contrast, our Lorenz gauge calculation yields a set of MP amplitudes for each $l$ and $m$ in a tensor spherical harmonic expansion. The former can be derived from the latter by reexpanding each tensor

spherical harmonic in our expression for $F_{\text{ret}}^\alpha$ as a sum of scalar spherical harmonics. To that end, we take the definition of $k^{\alpha\beta\gamma\delta}(x, x_p)$ given above, along with the tensor spherical harmonic expansion of the retarded MP given in Eq. (2.15) and substitute in Eq. (2.29). Taking the limit $r \to r_p(t)$ while maintaining $\theta$ and $\varphi$ dependence leaves [34]

$$[F_{\text{ret}}^\alpha(t, r_p(t), \theta, \varphi)]_\pm$$
$$= \frac{\mu}{r_p^2} \sum_{l=0}^\infty \sum_{m=-l}^l [f_0^{\alpha lm} Y^{lm} + f_1^{\alpha lm} \sin^2\theta Y^{lm} + f_2^{\alpha lm} \sin\theta\cos\theta Y_{,\theta}^{lm}$$
$$+ f_3^{\alpha lm} \sin^2\theta Y_{,\theta\theta}^{lm} + f_4^{\alpha lm} (\cos\theta Y^{lm} - \sin\theta Y_{,\theta}^{lm})$$
$$+ f_5^{\alpha lm} \sin\theta Y_{,\theta}^{lm} + f_6^{\alpha lm} \sin^3\theta Y_{,\theta}^{lm} + f_7^{\alpha lm} \sin^2\theta\cos\theta Y_{,\theta\theta}^{lm}]_\pm, \qquad (2.32)$$

where a comma indicates a partial derivative. The vectors $f_0^{\alpha lm} \ldots f_7^{\alpha lm}$ are functions of the MP amplitudes and their

first $t$ and $r$ derivatives. Our tensor harmonic decomposition of the MP differs from Ref. [34], and so we provide the detailed form of these functions in Appendix C. The MP amplitudes are $\mathcal{O}(\mu)$, which makes the GSF of order $\mathcal{O}(\mu^2)$. Each of the functions $f_0^{\alpha lm} \dots f_7^{\alpha lm}$, as well as $F_{\text{ret}}^{\alpha}$, takes on a pair of values $(\pm)$ since the limit $r \to r_p(t)$ can be applied from the outside or inside of the particle radius $r_p(t)$. Differing limits on the two sides also appear in the RP $F_{[-1]}^{\alpha}$ and therefore in $F_S^{\alpha}$. The regularized GSF itself is single valued, though.

Finally, we obtain $F_{\text{ret}}^{\alpha l'}$ by expanding the $\theta$-dependent terms in (2.32) as sums of scalar spherical harmonics. This yields the following expression:

$$[F_{\text{ret}}^{\alpha l'}]_{\pm} = \frac{\mu}{r_p^2} \sum_{m=-l'}^{l'} Y^{l'm} [\mathcal{F}_{(-3)}^{\alpha l'-3,m} + \mathcal{F}_{(-2)}^{\alpha l'-2,m} + \mathcal{F}_{(-1)}^{\alpha l'-1,m}$$
$$+ \mathcal{F}_{(0)}^{\alpha l',m} + \mathcal{F}_{(+1)}^{\alpha l'+1,m} + \mathcal{F}_{(+2)}^{\alpha l'+2,m} + \mathcal{F}_{(+3)}^{\alpha l'+3,m}]_{\pm}. \tag{2.33}$$

The functions $\mathcal{F}_{(j)}^{\alpha l,m}$, given in Ref. [34], are found to each be a linear combination of the $f_n^{\alpha lm}$ of the same $l$ and $m$. Accordingly, a given $l'$ term used in the MSR formula couples only to tensor spherical harmonic amplitudes in the range $l' - 3 \leq l \leq l' + 3$.

## F. Conservative and dissipative parts of the self-force and first-order changes in orbital constants

The procedure described in the previous subsection takes the retarded field and produces the regular $(R)$ force (i.e., the self-force). To make the notation clear, we can write this retarded self-force as $F_{R,\text{ret}}^{\alpha}$. It is also conceivable to calculate the advanced self-force $F_{R,\text{adv}}^{\alpha}$, which is obtained by precisely the same procedure except in replacing $\bar{p}_{\mu\nu}^{\text{ret}}$ with $\bar{p}_{\mu\nu}^{\text{adv}}$. The singular field $F_S^{\alpha}$ is time symmetric, so the RPs are unaffected in swapping "ret" for "adv." Hinderer and Flanagan [65] show that it is convenient to split the retarded and advanced self-force into conservative and dissipative parts,

$$F_{R,\text{ret}}^{\alpha} = F_{\text{cons}}^{\alpha} + F_{\text{diss}}^{\alpha}, \qquad F_{R,\text{adv}}^{\alpha} = F_{\text{cons}}^{\alpha} - F_{\text{diss}}^{\alpha}, \tag{2.34}$$

where

$$F_{\text{cons}}^{\alpha} = \frac{1}{2}(F_{R,\text{ret}}^{\alpha} + F_{R,\text{adv}}^{\alpha}), \qquad F_{\text{diss}}^{\alpha} = \frac{1}{2}(F_{R,\text{ret}}^{\alpha} - F_{R,\text{adv}}^{\alpha}). \tag{2.35}$$

See also Ref. [83]. Furthermore, because of the symmetry, the conservative part actually requires regularization,

$$F_{\text{cons}}^{\alpha} = \sum_{l'=0}^{\infty} \left[ \frac{1}{2}(F_{\text{ret}}^{\alpha l'} + F_{\text{adv}}^{\alpha l'}) - F_S^{\alpha l'} \right], \tag{2.36}$$

while the dissipative part does not,

$$F_{\text{diss}}^{\alpha} = \frac{1}{2} \sum_{l'=0}^{\infty} (F_{\text{ret}}^{\alpha l'} - F_{\text{adv}}^{\alpha l'}). \tag{2.37}$$

Conveniently, for geodesic motion on Schwarzschild, the advanced self-force can be obtained from the retarded self-force using time reversal and symmetry,

$$F_{R,\text{adv}}^{\alpha}(\tau) = \epsilon_{(\alpha)} F_{R,\text{ret}}^{\alpha}(-\tau), \tag{2.38}$$

where $\tau = 0$ corresponds to periastron passage and the Schwarzschild components change sign or not according to $\epsilon_{(\alpha)} = (-1, 1, 1, -1)$, with no implied sum in the equation above.

The self-force produces changes in the orbital constants $\mathcal{E} = -u_t$ and $\mathcal{L} = u_{\varphi}$. Using the first-order equations of motion

$$\mu \frac{Du_{\alpha}}{D\tau} = g_{\alpha\beta} F_R^{\beta}, \tag{2.39}$$

the $t$ component $F_R^t$ provides a rate of work, and the $\varphi$ component $F_R^{\varphi}$ gives a torque such that

$$\dot{\mathcal{E}} = \frac{f_p}{\mu u^t} F_R^t, \qquad \dot{\mathcal{L}} = \frac{r_p^2}{\mu u^t} F_R^{\varphi}, \tag{2.40}$$

where the dot refers to derivative with respect to Schwarzschild time $t$. While the first-order GSF determines the leading-order, adiabatic motion and contributes terms to the post-1-adiabatic corrections [65], the leading-order adiabatic changes require only the orbit-averaged part of the dissipative GSF:

$$\langle \dot{\mathcal{E}} \rangle = \frac{1}{T_r} \int_0^{T_r} \frac{f_p}{\mu u^t} F_{\text{diss}}^t dt, \qquad \langle \dot{\mathcal{L}} \rangle = \frac{1}{T_r} \int_0^{T_r} \frac{r_p^2}{\mu u^t} F_{\text{diss}}^{\varphi} dt. \tag{2.41}$$

For the geodesic GSF, the first-order rate of work and torque are balanced by the energy and angular momentum fluxes (each averaged over the orbital period and summed over 2-surfaces near infinity and the horizon) calculated from the first-order MP (see Sec. V B).

## III. FREQUENCY DOMAIN TECHNIQUES FOR SOLVING COUPLED SYSTEMS

Rather than solve directly the TD Lorenz gauge equations of Sec. II D, we use FD techniques for their speed and accuracy. Accuracy requirements were discussed in the Introduction, and these are attained in the FD through

solution of ordinary differential equations (ODEs). The TD alternative [34], solving $1 + 1$-dimensional partial differential equations for each $l, m$, has the compensating advantage of allowing the GSF to be applied self-consistently [72]. The specific equations we solve are the FD version of the fully constrained field equations (2.24) and (2.25) and the gauge conditions (2.22) and (2.23), obtained by taking $\partial_t \to -i\omega$ and replacing amplitudes, e.g., $h_{tt}(t, r) \to \tilde{h}_{tt}(r)$. Subsequently the solution is returned to the TD, whence the GSF can be calculated. The Fourier synthesis uses the method of EHS [40], which circumvents the Gibbs phenomenon encountered with a distributional source.

Below we set the notation for the Fourier transform, give a matrix notation for the coupled sets of FD ODEs, and discuss independent bases of homogeneous solutions that appear at leading order asymptotically. We then discuss the use of variation of parameters and how EHS is broadened to encompass systems of ODEs.

### A. Fourier decomposition

As explained in Sec. II A, two fundamental frequencies, $\Omega_r$ and $\Omega_\varphi$, exist in the eccentric-orbit Schwarzschild E/IMRI problem. In the frame that rotates at the mean azimuthal rate ($\varphi' = \varphi - \Omega_\varphi t$), the MP appears nonsinusoidal but periodic in $t$. It can be represented in a Fourier series in harmonics $n\Omega_r$. In the inertial frame, the phase of each multipole with $m \neq 0$ advances linearly, giving the Fourier-harmonic modes a spectrum

$$\omega \equiv \omega_{mn} = m\Omega_\varphi + n\Omega_r. \tag{3.1}$$

Each MP and source amplitude is replaced by a Fourier series (with a tilde denoting a FD amplitude). For a generic

amplitude $X_{lm}$ (not to be confused with the tensor harmonics $X_A^{lm}$ and $X_{AB}^{lm}$), we have

$$\tilde{X}_{lmn}(r) = \frac{1}{T_r} \int_0^{T_r} X_{lm}(t, r) e^{i\omega_{mn}t} dt,$$

$$X_{lm}(t, r) = \sum_{n=-\infty}^{\infty} \tilde{X}_{lmn}(r) e^{-i\omega_{mn}t}. \tag{3.2}$$

Henceforth, not only will indices $l$ and $m$ be suppressed, but so will $n$ on FD objects (unless otherwise noted).

### B. Matrix notation for coupled ODE systems

It is convenient to place the coupled FD equations in matrix form. For even and odd parities, respectively, the fields appearing in the constrained systems are assembled into the vectors

$$\tilde{\mathcal{E}}(r) = r \begin{bmatrix} \tilde{h}_{tt} \\ f\tilde{h}_{tr} \\ f^2\tilde{h}_{rr} \\ \tilde{K} \end{bmatrix}, \qquad \tilde{\mathcal{B}}(r) = \begin{bmatrix} \tilde{h}_t \\ f\tilde{h}_r \end{bmatrix}. \tag{3.3}$$

With this notation the even- and odd-parity FD equations are compactly expressed in matrix form

$$\tilde{\mathcal{E}}'' + \mathbf{A}\tilde{\mathcal{E}}' + \mathbf{B}\tilde{\mathcal{E}} = \tilde{\mathcal{U}}, \qquad \tilde{\mathcal{B}}'' + \mathbf{C}\tilde{\mathcal{B}}' + \mathbf{D}\tilde{\mathcal{B}} = \tilde{\mathcal{V}}, \tag{3.4}$$

with the prime indicating differentiation with respect to tortoise coordinate $r_*$ and where the solution vectors and source vectors have dimension $k = 4$ or $k = 2$ for even or odd parity, respectively. In the general case, the matrices that couple the amplitudes and their first derivatives are

$$\mathbf{A} = \frac{1}{r^2} \begin{bmatrix} -4M & 0 & 0 & 0 \\ 0 & 2(r - 4M) & 0 & 0 \\ 2rf & 0 & 2(r - 4M) & -4rf^2 \\ -r & 0 & -r & 2rf \end{bmatrix},$$

$$\mathbf{B} = \left( \omega^2 - \frac{2(\lambda + 1)f}{r^2} \right) \mathbf{I} + \frac{1}{r^4} \begin{bmatrix} 2M(r - M) & -4i\omega Mr^2 & -2M(2r - 3M) & 4Mrf^2 \\ i\omega r^2(r - 4M) & -2fMr & i\omega r^2(r - 4M) & 2i\omega r^3 f^2 \\ -2(r - M)^2 & 4i\omega r^2(r - 3M) & 2(r^2 - 3Mr + 3M^2) & -4Mrf^2 \\ r^2 & -2i\omega r^3 & -r^2 & 2fMr \end{bmatrix}, \tag{3.5}$$

$$\mathbf{C} = \frac{2}{r^2} \begin{bmatrix} -M & 0 \\ 0 & r - 3M \end{bmatrix}, \qquad \mathbf{D} = \left( \omega^2 - \frac{2f^2 + 2\lambda f}{r^2} \right) \mathbf{I} + \frac{2i\omega}{r^2} \begin{bmatrix} 0 & -M \\ r - 3M & 0 \end{bmatrix}, \tag{3.6}$$

where the **I**'s are relevant-sized identity matrices ($k \times k = 4 \times 4$ or $2 \times 2$). The source vectors are

$$\tilde{\mathcal{U}} = r \begin{bmatrix} -f\tilde{Q}^{rr} - f^2\tilde{Q}^{\flat} - f^3\tilde{Q}^{tt} \\ 2f^2\tilde{Q}^{tr} \\ -f\tilde{Q}^{rr} + f^2\tilde{Q}^{\flat} - f^3\tilde{Q}^{tt} \\ \tilde{Q}^{rr} - f^2\tilde{Q}^{tt} \end{bmatrix}, \qquad \tilde{\mathcal{V}} = \begin{bmatrix} f^2\tilde{P}^t \\ -f\tilde{P}^r \end{bmatrix}.$$

(3.7)

In certain special cases (low-order modes or static modes), some components of the vectors $\tilde{\mathcal{E}}$ and $\tilde{\mathcal{B}}$ identically vanish, effectively reducing the order of the system, with concomitant reduction in the source components and elements of **A**, ..., **D**. These special cases are detailed in Sec. IV.

## C. Linearly independent sets of homogeneous solutions

The constrained even-parity equations are a set of four, coupled, second-order ODEs. As such they have eight linearly independent homogeneous solutions. We divide these into four solutions $\tilde{\mathcal{E}}_i^+$ (with $i = 0, 1, 2, 3$) that have causal, running-wave dependence $e^{i\omega r_*}$ at $r_* = +\infty$ and four solutions $\tilde{\mathcal{E}}_i^-$ that are downgoing, $e^{-i\omega r_*}$, at the horizon ($r_* = -\infty$). For odd parity, where the system is a set of two, coupled, second-order ODEs, there are four linearly independent homogeneous solutions. In parallel we denote these by $\tilde{\mathcal{B}}_i^{\pm}$ with $i = 0, 1$. A complete basis of linearly independent homogeneous solutions is of dimension $2k$.

Upon examining the asymptotic limits of Eq. (3.4) as $r_* \to \pm\infty$, we find the following is one possible representation of the leading-order behavior of the even-parity homogeneous solutions:

$$(\tilde{\mathcal{E}}_0^-)^{\top} \sim (1, 1, 1, 0)e^{-i\omega r_*},$$

$$(\tilde{\mathcal{E}}_0^+)^{\top} \sim (1, 0, -1, 0)e^{i\omega r_*},$$

$$(\tilde{\mathcal{E}}_1^-)^{\top} \sim (1, 0, -1, -2(1 - 4i\omega M)^{-1})fe^{-i\omega r_*},$$

$$(\tilde{\mathcal{E}}_1^+)^{\top} \sim (0, 1, -2, 0)e^{i\omega r_*},$$

$$(\tilde{\mathcal{E}}_2^-)^{\top} \sim (1, -1, 1, 1)f^2 e^{-i\omega r_*},$$

$$(\tilde{\mathcal{E}}_2^+)^{\top} \sim (0, 1, -2, 1)r^{-1}e^{i\omega r_*},$$

$$(\tilde{\mathcal{E}}_3^-)^{\top} \sim (0, 0, 0, 1)e^{-i\omega r_*},$$

$$(\tilde{\mathcal{E}}_3^+)^{\top} \sim (0, 0, -2, 1)r^{-2}e^{i\omega r_*},$$

(3.8)

where $\top$ indicates transpose. We note that, while these vectors are linearly independent, the MP amplitudes

(components) do not decouple asymptotically. Likewise the asymptotic limits of the odd-parity equations allow the following representation of the leading-order behavior of odd-parity homogeneous solutions:

$$(\tilde{\mathcal{B}}_0^-)^{\top} \sim (1, 1)e^{-i\omega r_*}, \qquad (\tilde{\mathcal{B}}_0^+)^{\top} \sim (1, -1)e^{i\omega r_*},$$

$$(\tilde{\mathcal{B}}_1^-)^{\top} \sim (1, -1)fe^{-i\omega r_*}, \qquad (\tilde{\mathcal{B}}_1^+)^{\top} \sim (0, 1)r^{-1}e^{i\omega r_*}. \quad (3.9)$$

Here again, while the odd-parity vectors are linearly independent, the MP amplitudes are still mixed between them asymptotically.

The limiting behavior for $\tilde{\mathcal{E}}_i^{\pm}$ and $\tilde{\mathcal{B}}_i^{\pm}$ displayed in (3.8) and (3.9) is merely one possible choice, and we refer to these as the *simple bases*. It is, however, clearly possible to introduce linear transformations on these sets of eight and four homogeneous solutions, and we describe in Sec. IV A clear advantages in doing so at least for the even- and odd-parity bases on the near-infinity side.

## D. Variation of parameters and extended homogeneous solutions for coupled systems

With the assumption that sets of homogeneous solutions $\tilde{\mathcal{E}}_i^{\pm}$ and $\tilde{\mathcal{B}}_i^{\pm}$ have been obtained by integrating Eqs. (3.4) (subject to the boundary conditions of the previous section or other equivalently independent ones), it is straightforward to construct solutions to the inhomogeneous equations using a variation of parameters. Introducing a set of $2k$ variable coefficients $c_i^{\pm}(r)$ that multiply the homogeneous basis elements, the particular solutions are assumed to have the forms

$$\tilde{\mathcal{E}}(r) = \sum_{i=0}^{3} (\tilde{\mathcal{E}}_i^- c_i^{e,-}(r) + \tilde{\mathcal{E}}_i^+ c_i^{e,+}(r)),$$

$$\tilde{\mathcal{B}}(r) = \sum_{i=0}^{1} (\tilde{\mathcal{B}}_i^- c_i^{o,-}(r) + \tilde{\mathcal{B}}_i^+ c_i^{o,+}(r)). \quad (3.10)$$

Variation of parameters then assumes that the first derivative of (3.10) also depends only on the coefficients $c_i^{\pm}(r)$, and not their derivatives, by placing a set of $k$ conditions on $\partial_{r_*} c_i^{\pm}(r)$. Differentiating again and substituting into Eqs. (3.4) yields a second set of $k$ conditions on $\partial_{r_*} c_i^{\pm}(r)$. Taken together these conditions form a linear system with a $2k \times 2k$ matrix **M**, formed from the homogeneous basis elements and their first derivative, that acts on the vector made up of the first derivative of the coefficients $c_i^{\pm}(r)$. The matrix **M** is the Wronksian matrix. In odd parity ($k = 2$) these equations have the form

$$\mathbf{M} \begin{bmatrix} \partial_{r_*} c_0^{o,-} \\ \partial_{r_*} c_1^{o,-} \\ \partial_{r_*} c_0^{o,+} \\ \partial_{r_*} c_1^{o,+} \end{bmatrix}$$

$$= \begin{bmatrix} \tilde{\mathcal{B}}_0^- & \tilde{\mathcal{B}}_1^- & \tilde{\mathcal{B}}_0^+ & \tilde{\mathcal{B}}_1^+ \\ \partial_{r_*} \tilde{\mathcal{B}}_0^- & \partial_{r_*} \tilde{\mathcal{B}}_1^- & \partial_{r_*} \tilde{\mathcal{B}}_0^+ & \partial_{r_*} \tilde{\mathcal{B}}_1^+ \end{bmatrix} \begin{bmatrix} \partial_{r_*} c_0^{o,-} \\ \partial_{r_*} c_1^{o,-} \\ \partial_{r_*} c_0^{o,+} \\ \partial_{r_*} c_1^{o,+} \end{bmatrix}$$

$$= \begin{bmatrix} \mathbf{0} \\ \tilde{\mathcal{V}} \end{bmatrix}, \tag{3.11}$$

where bold entries are $2 \times 1$ column vectors.

The normalization functions are then found by matrix inversion followed by integration over the source region

$$c_i^{e/o,+}(r) = \int_{r_{\min}}^r \frac{1}{f} \frac{W_i^{e/o,+}}{W^{e/o}} dr',$$

$$c_i^{e/o,-}(r) = -\int_r^{r_{\max}} \frac{1}{f} \frac{W_i^{e/o,-}}{W^{e/o}} dr'. \tag{3.12}$$

In these integrals $W^{e/o}$ is the determinant of the Wronskian matrix (even or odd parity). The determinants $W_i^{e/o,\pm}$ are formed by replacing the column in the Wronskian corresponding to the $i$th homogeneous solution with the column vector $(\mathbf{0}, \tilde{\mathcal{U}})^\top$ or $(\mathbf{0}, \tilde{\mathcal{V}})^\top$ (even or odd parity) in accordance with Cramer's rule. Again, for odd parity, the Wronskian and one of the modified Wronskians are

$$W^o = \begin{vmatrix} \tilde{\mathcal{B}}_0^- & \tilde{\mathcal{B}}_1^- & \tilde{\mathcal{B}}_0^+ & \tilde{\mathcal{B}}_1^+ \\ \partial_{r_*} \tilde{\mathcal{B}}_0^- & \partial_{r_*} \tilde{\mathcal{B}}_1^- & \partial_{r_*} \tilde{\mathcal{B}}_0^+ & \partial_{r_*} \tilde{\mathcal{B}}_1^+ \end{vmatrix},$$

$$W_0^{o,-} = \begin{vmatrix} \mathbf{0} & \tilde{\mathcal{B}}_1^- & \tilde{\mathcal{B}}_0^+ & \tilde{\mathcal{B}}_1^+ \\ \tilde{\mathcal{V}} & \partial_{r_*} \tilde{\mathcal{B}}_1^- & \partial_{r_*} \tilde{\mathcal{B}}_0^+ & \partial_{r_*} \tilde{\mathcal{B}}_1^+ \end{vmatrix}. \tag{3.13}$$

Thus, both $W^o$ and $W_0^{o,-}$ are determinants of $4 \times 4$ matrices. In even parity the matrices are $8 \times 8$, and in special cases other matrix ranks occur. In this section we have sketched using Cramer's rule for the matrix inversion merely to provide a compact discussion. In reality we use LU decomposition in the code to provide the numerical inversion.

Once the normalization functions $c_i^{e/o,\pm}(r)$ are known, the particular solutions (3.10) can be computed. However, since the source in the TD problem is distributional, this standard procedure is fraught with the appearance of Gibbs behavior in the MP (and GSF) upon returning to the TD. Its use is now supplanted by the method of EHS, though the EHS method uses key parts of the standard-approach machinery.

Barack, Ori, and Sago [40] developed the EHS method and applied it in computing the scalar field of a charge in eccentric orbit about a Schwarzschild black hole. Subsequently, Hopper and Evans [31] employed EHS to compute the MPs of a small mass in eccentric orbit on Schwarzschild in the Regge–Wheeler–Zerilli formalism. EHS was also used [34,62] to compute the low-order ($l = 0, 1$) modes in Lorenz gauge, which marked its first use for a coupled system. EHS then found use in modeling the scalar self-force on a particle in eccentric equatorial orbit on a Kerr black hole [84]. In addition, a variant called the method of extended particular solutions was developed [85] that is useful for certain problems with noncompact source terms. It was employed to compute the gauge vector that generates the odd-parity transformation of the MP from Regge–Wheeler to Lorenz gauge.

Our application of EHS to general MPs in Lorenz gauge for eccentric orbital motion on Schwarzschild was developed contemporaneously with Akcay, Warburton, and Barack (see talks at the 2012 Capra meeting [63,86,87]). Their code was applied [36] to long-term inspiral, and their full method has been published [37].

EHS uses the matrix inversion and integration involved in computing the normalization functions but extends the integration over the entire source region to obtain a set of complex constants. In practice, the integration is done with respect to $\chi$,

$$C_i^{e/o,\pm} = \pm \int_0^\pi \frac{1}{f(r_p(\chi))} \frac{W_i^{e/o,\pm}(r_p(\chi))}{W^{e/o}(r_p(\chi))} \frac{dr_p}{d\chi} d\chi, \tag{3.14}$$

providing better numerical behavior at the turning points. These constants are used to normalize the basis vectors and to assemble specific linear combinations, referred to as FD extended homogeneous solutions. They are smooth functions everywhere outside the horizon ($r > 2M$),

$$\tilde{\mathcal{E}}^\pm(r) = \sum_{i=0}^3 C_i^{e,\pm} \tilde{\mathcal{E}}_i^\pm, \qquad \tilde{\mathcal{B}}^\pm(r) = \sum_{i=0}^1 C_i^{o,\pm} \tilde{\mathcal{B}}_i^\pm. \tag{3.15}$$

Using these functions, exponentially convergent Fourier sums then provide the TD extended homogeneous solutions

$$\mathcal{E}^\pm(t, r) = \sum_{n=-\infty}^\infty \tilde{\mathcal{E}}^\pm(r) e^{-i\omega t},$$

$$\mathcal{B}^\pm(t, r) = \sum_{n=-\infty}^\infty \tilde{\mathcal{B}}^\pm(r) e^{-i\omega t}, \tag{3.16}$$

which likewise hold for all $r > 2M$ and are smooth in $r$ and $t$. The solutions to Eqs. (2.24) and (2.25) then follow by abutting the $+$ and $-$ TD EHS at the location of the particle,

$$\mathcal{E}(t, r) = \mathcal{E}^+ \theta[r - r_p(t)] + \mathcal{E}^- \theta[r_p(t) - r],$$

$$\mathcal{B}(t, r) = \mathcal{B}^+ \theta[r - r_p(t)] + \mathcal{B}^- \theta[r_p(t) - r]. \qquad (3.17)$$

In Lorenz gauge all of the MP amplitudes are $C^0$ at $r = r_p(t)$. The discontinuity in the derivative is encoded by the presence of the $\theta$ functions. While the Lorenz gauge MP amplitudes must analytically satisfy $\mathcal{E}^+(t, r_p(t)) = \mathcal{E}^-(t, r_p(t))$ and $\mathcal{B}^+(t, r_p(t)) = \mathcal{B}^-(t, r_p(t))$, the degree to which this equality is satisfied numerically is a measure of convergence.

## IV. NUMERICAL ALGORITHM

In this section we provide details on our numerical algorithm. For a geodesic given by $p$ and $e$, we seek to compute to sufficient accuracy the MP and the GSF, $F_R^\alpha$, as functions of time around the orbit. We first itemize the principal steps and then follow with detailed discussion on some aspects of the procedure:

(1) Orbital parameters: For a given $p$ and $e$, integrate the orbit equations to find the period of radial motion $T_r$ and fundamental frequencies $\Omega_r$ and $\Omega_\varphi$. Determine also $\mathcal{E}$, $\mathcal{L}$, $r_{\min}$, and $r_{\max}$ (Sec. II A).

(2) Mode characterization: Fourier-harmonic modes divide into classes according to $l, m, n$. Low-multipole modes $l = 0, 1$ are handled separately from $l \geq 2$ radiative modes. We further divide modes into static ($m = n = 0$), near-static ($0 < |\omega M| < 10^{-4}$), or general cases. See Table I for an overlapping breakdown of modes.

(3) Linearly independent, causal homogeneous bases: For every $l, m, n$ mode, find or compute a complete

set of $2k$ independent homogeneous solutions. In general, the solution process begins with providing causal initial conditions at the boundaries using Taylor series or asymptotic expansions (Appendix A) and performing numerical ODE integrations (Sec. III C) into the source region. On the horizon side, boundary conditions are set at $r_* = -6M$, and sufficient Taylor expansion terms are included to reach a fractional error of $\sim 10^{-15}$. At large radius, the starting location depends on mode and frequency. Large enough starting radius is taken, and short integrations are used to confirm the asymptotic expansions have errors of order $10^{-14}$. All of the homogeneous solutions are then integrated to $r_* = r_*^{\min}$ (i.e., the value of $r_*$ when $r = r_{\min}$). Orthogonality of the initial vectors is carefully considered to minimize ill conditioning of matrix inversion (Sec. IV A). For near-static ($0 < |\omega M| < 10^{-4}$) modes, we employ special techniques to overcome strong ill conditioning (Secs. IV A and IV B). Static (zero frequency) modes have exact analytic homogeneous solutions (Sec. IV C). The systems of equations change character or reduce in size for low-multipole modes (Sec. IV D).

(4) FD extended homogeneous solutions: For each $l, m, n$ the homogeneous solutions are integrated over the source from $r_{\min}$ to $r_{\max}$ to find normalization constants and the linear combinations that represent the FD EHS (Sec. III D). Again, for near-static ($0 < |\omega M| < 10^{-4}$) modes, we employ special techniques to overcome strong ill conditioning (Sec. IV B). Special consideration occurs again for low-multipole modes.

TABLE I. Classification of FD modes as functions of $lm\omega$. Most modes (i.e., general case) are found by solving the complete fully constrained systems (2.24) and (2.25) and deriving the remaining fields using the gauge conditions (2.22) and (2.23). Special cases include static, near-static, and low-multipole ($l = 0, 1$) modes. For static and low-multipole modes, the system size reduces, and some MP amplitudes identically vanish. Special cases are discussed in separate sections as noted.

| $l$ | Parity | Frequency | No. field eqs. | No. constraints | Variables in reduced eqs. | Variables from constraints | Section |
|---|---|---|---|---|---|---|---|
| $l \geq 2$ | Even | General | 7 | 3 | $\tilde{h}_{tt}, \tilde{h}_{tr}, \tilde{h}_{rr}, \tilde{K}$ | $\tilde{j}_t, \tilde{j}_r, \tilde{G}$ | IV A |
| | | Near-static | 7 | 3 | $\tilde{h}_{tt}, \tilde{h}_{tr}, \tilde{h}_{rr}, \tilde{K}$ | $\tilde{j}_t, \tilde{j}_r, \tilde{G}$ | IV B |
| | | Static | 5 | 2 | $\tilde{h}_{tt}, \tilde{h}_{rr}, \tilde{K}$ | $\tilde{j}_r, \tilde{G}$ | IV C |
| | Odd | General | 3 | 1 | $\tilde{h}_t, \tilde{h}_r$ | $\tilde{h}_2$ | IV A |
| | | Near-static | 3 | 1 | $\tilde{h}_t, \tilde{h}_r$ | $\tilde{h}_2$ | IV B |
| | | Static | 1 | 0 | $\tilde{h}_t$ | - | IV C |
| $l = 1$ | Even | General | 6 | 3 | $\tilde{h}_{tt}, \tilde{h}_{tr}, \tilde{h}_{rr}, \tilde{K}$ | $\tilde{j}_t, \tilde{j}_r$ | IV A |
| | | Near-static | 6 | 3 | $\tilde{h}_{tt}, \tilde{h}_{tr}, \tilde{h}_{rr}, \tilde{K}$ | $\tilde{j}_t, \tilde{j}_r$ | IV B |
| | Odd | General | 2 | 1 | $\tilde{h}_t, \tilde{h}_r$ | - | IV A |
| | | Static | 1 | 0 | $\tilde{h}_t$ | - | IV D |
| $l = 0$ | Even | General | 4 | 2 | $\tilde{h}_{tt}, \tilde{h}_{tr}, \tilde{h}_{rr}, \tilde{K}$ | - | IV A |
| | | Static | 3 | 1 | $\tilde{h}_{tt}, \tilde{h}_{rr}, \tilde{K}$ | - | IV D |

(5) TD extended homogeneous solutions: For every $l, m$ construct the TD EHS (Sec. III D) by summing over sufficient positive and negative $n$ until the Fourier series on each side converge to a relative error of $\sim 10^{-10}$. Not only can convergence of the EHS on each side of $r_p(t)$ be monitored, but each $l, m$ mode should approach becoming $C^0$, and the derivative in $r$ at the particle should satisfy a jump condition.

(6) Assemble $l'$ contributions to $F_{\text{ret}}^{\alpha l'}$: Compute force terms $f_n^{\alpha l m}$ (Appendix C) and linear combinations $\mathcal{F}_{(j)}^{\alpha l, m}$ (Sec. II E), and sum over $m$ for each $l$ mode. Only $m \geq 0$ modes need be computed, since $m < 0$ are determined by crossing relations on the spherical harmonics. Assemble the $l'$ part of the retarded force by combining $l$ for $l' - 3 \leq l \leq l' + 3$.

(7) Apply MSR to obtain GSF: Sum over $l'$ in the MSR formula until the GSF converges to a prescribed tolerance or minimum error (Sec. II E). In the process we use available analytically calculated regularization parameters $F_{[-1]}^{\alpha}$, $F_{[0]}^{\alpha}$, $F_{[2]}^{\alpha}$, and $F_{[4]}^{\alpha}$ and a least-squares fit for $F_{[6]}^{\alpha}$ and $F_{[8]}^{\alpha}$ using the last seven $l'$ modes. We find that the error (by comparing the regularized self-force on the two sides of the particle) minimizes for $l'_{\max} \simeq 13$ for low eccentricities and several modes lower for high eccentricity. A required $l'_{\max}$ implies that we must compute tensor spherical harmonic modes up to $l_{\max} = l'_{\max} + 3$.

## A. General modes

We first consider the general case, encompassing all modes with $l \geq 2$ that are neither static nor near static. The expressions (3.8) and (3.9) provide leading-order behavior for the MP amplitudes as $r_* \to \pm\infty$. In practice, boundary conditions are set at finite radii and require expansions with numerous terms beyond just this leading order. Appendix A provides details on the asymptotic ($r_* \to +\infty$) and Taylor ($r_* \to -\infty$) expansions that are used to set accurate boundary conditions as close to the source region as possible. Unique numerical issues are encountered on both the near-horizon and near-infinity sides.

### 1. Boundary conditions near the horizon and subdominance instability

On the near-horizon side, using the simple bases of (3.8) and (3.9) at large negative $r_*$ is found to generate a subdominance instability. There is an undesired, acausal (upgoing) homogeneous solution that can be excited by roundoff errors in the numerical boundary condition that grows exponentially relative to a desired (subdominant) causal solution. Figure 2 shows the effect of starting the integration at various initial $r_*^H$ and integrating to $r_* = 10M$. Setting the boundary at $r_*^H < -10M$ generates substantial growth of this acausal mode. We now explain briefly why this occurs. We use odd parity as the example, with even parity following a similar analysis.

A complete set of odd-parity independent homogeneous solutions at the event horizon has leading behavior

$$(\tilde{\mathcal{B}}_0^-)^\top \sim (1,1)e^{-i\omega r_*}, \quad (\tilde{\mathcal{B}}_2^-)^\top \sim (1,1)fe^{+i\omega r_*},$$
$$(\tilde{\mathcal{B}}_1^-)^\top \sim (1,-1)fe^{-i\omega r_*}, \quad (\tilde{\mathcal{B}}_3^-)^\top \sim (1,-1)e^{+i\omega r_*}. \quad (4.1)$$

$\tilde{\mathcal{B}}_0^-$ and $\tilde{\mathcal{B}}_1^-$ are the desired causal solutions of Eq. (3.9), representing downgoing modes, while $\tilde{\mathcal{B}}_2^-$ and $\tilde{\mathcal{B}}_3^-$ are acausal, representing radiation coming up from the black hole. When we attempt to set boundary conditions for $\tilde{\mathcal{B}}_0^-$
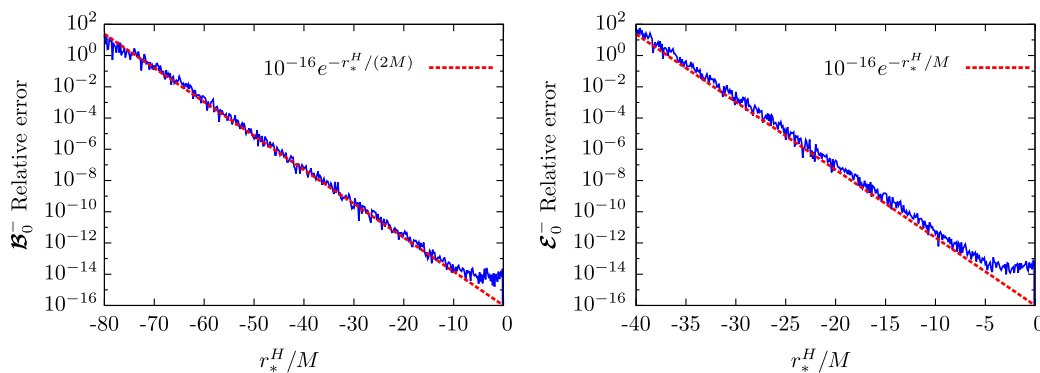


FIG. 2 (color online).    Subdominance instability and growth of roundoff errors with starting location. We demonstrate the effects of a subdominance instability by comparing results of numerical integrations begun at different initial radii $r_*^H$ near the horizon and ending at $r_* = 10M$. The chosen modes have $l = 2$ and $M\omega = 1$ (odd parity on the left; even parity on the right). The fiducial, accurate solution is obtained from a high-order Taylor expansion, with sufficient terms that residuals are at or below roundoff even at a radius of $r_*^H = 0$. Using the Taylor expansion at any $-6M < r_*^H < 0$ to begin an integration that then ends at $r_* = 10M$ gives results that are consistent with each other. However, as smaller initial radii are chosen ($r_*^H < -10M$), exponentially greater errors are found in comparing at $r_* = 10M$ the integrated mode and the fiducial Taylor expansion. We avoid the instability by beginning all integrations at $r_*^H = -6M$ with initial conditions from the high-order Taylor expansion.

and $\tilde{\mathcal{B}}_1^-$, the inherent limitations of our double precision routines produce instead numerical superpositions

$$\tilde{\mathcal{B}}_0^{-,N} = \tilde{\mathcal{B}}_0^- + \alpha_1 \tilde{\mathcal{B}}_1^- + \alpha_2 \tilde{\mathcal{B}}_2^- + \alpha_3 \tilde{\mathcal{B}}_3^-,$$
$$\tilde{\mathcal{B}}_1^{-,N} = \tilde{\mathcal{B}}_1^- + \beta_0 \tilde{\mathcal{B}}_0^- + \beta_2 \tilde{\mathcal{B}}_2^- + \beta_3 \tilde{\mathcal{B}}_3^-, \qquad (4.2)$$

where all the terms $\alpha_n \tilde{\mathcal{B}}_n^-$ and $\beta_n \tilde{\mathcal{B}}_n^-$ are of order $\sim 10^{-16}$ (roundoff) times the desired dependence. We must be concerned with any of these roundoff terms that are acausal and grow relative to the causal terms as we integrate from our starting location, $r_*^H$. Near the horizon $f \sim e^{r_*/2M}$, meaning $\alpha_2 \tilde{\mathcal{B}}_2^-$, an acausal contribution to $\tilde{\mathcal{B}}_0^{-,N}$, has precisely this exponential growth relative to $\tilde{\mathcal{B}}_0^-$. This prediction is confirmed numerically, as shown in the left panel of Fig. 2. On the other hand, $\tilde{\mathcal{B}}_1^-$ itself grows like $e^{r_*/2M}$, and we see none of the other roundoff terms grow relative to it. As such, this solution does not display a subdominance instability.

In the case of even parity, the worst acausal mode has an $f^2$ radial dependence. Accordingly, its relative growth is even worse, i.e., $\sim e^{r_*/M}$. This is shown in the right panel of Fig. 2. The figure merely demonstrates the instability. In practice, we simply set the boundary condition at $r_*^H = -6M$ using Taylor series with sufficient terms to reach roundoff. The details of those Taylor series are found in Appendix A. We note finally that it is not inconceivable that the instability we discuss here is a result of the particular set of MP variables, and therefore the form of the Lorenz gauge equations, that we chose to use.

### 2. Boundary conditions at large radius and thin-QR preconditioning

On the near-infinity side, the expansions are asymptotic and require a large starting radius $r_*^\infty$, with the radius being roughly inversely related to mode frequency $\omega$. In what follows, we use the odd-parity equations as an example. Even parity follows a similar analysis. After long inward integration to $r_*^{\min}$, the outer solutions $\tilde{\mathcal{B}}_i^+$ can be combined with the inner solutions $\tilde{\mathcal{B}}_i^-$ to form the Wronskian matrix $\mathbf{M}$ [see Eq. (3.11)]. Unfortunately, especially at low frequency, we find the Wronskian matrix to be typically ill conditioned. Generally one can define a condition number of the matrix as $\kappa(\mathbf{M}) = |\lambda_{\max}/\lambda_{\min}|$, where $\lambda_{\max}$ and $\lambda_{\min}$ are the maximal and minimal eigenvalues of $\mathbf{M}$. Alternatively and conveniently, we may define it as $\kappa(\mathbf{M}) = \sigma_{\max}/\sigma_{\min}$, in terms of the singular values $\sigma_i$ of $\mathbf{M}$ in a singular value decomposition (SVD). The condition number is important since one loses roughly $\log_{10}(\kappa)$ digits of accuracy in operations like matrix inversion [88]. Starting with the leading-order, near-infinity behavior of the simple basis in Eq. (3.9) leads to condition numbers as large as $\kappa \sim 10^{12}$ in some cases.

Fortunately, it is possible to use a linear transformation on the simple basis $\tilde{\mathcal{B}}_i^+$ to find a new one $\tilde{\mathcal{B}}_{i'}^+$. Unfortunately, long integration of the altered set of homogeneous solutions to $r_*^{\min}$ is required in order to combine them with the inner solutions and calculate $\kappa$, making this a hit-or-miss procedure.

We have instead developed a novel means for determining a good linear transformation (at $r_*^\infty$) that reduces $\kappa$ by many orders of magnitude. While the method is most effective in handling near-static modes (discussed below in Sec. IV B), we nevertheless use it for all modes and therefore discuss it here. The technique involves using just half the information (outer solutions only) that goes into the Wronskian and calculating a "semicondition number" $\rho$. It begins by picking a basis (e.g., the simple one), taking the right half of the matrix $\mathbf{M}$, and forming the $4 \times 2$ matrix

$$\mathbf{V} \equiv \begin{bmatrix} \tilde{\mathcal{B}}_0^+ & \tilde{\mathcal{B}}_1^+ \\ \partial_{r_*} \tilde{\mathcal{B}}_0^+ & \partial_{r_*} \tilde{\mathcal{B}}_1^+ \end{bmatrix}. \qquad (4.3)$$

While $\mathbf{V}$ is a nonsquare matrix, it has a SVD and yields a set of non-negative, real singular values $\sigma_i$. In our example there are two singular values; for even parity there are four. We call the ratio of the largest to smallest, $\rho(\mathbf{V}) = \sigma_{\max}/\sigma_{\min}$, the semicondition number. An advantage of $\rho(\mathbf{V})$ is that it can be computed immediately once an outer basis is chosen. However, $\rho$ is not the same as the full condition number $\kappa$, which can only be computed once the complete set of (inner as well as outer) homogeneous solutions is compared. Empirically, though, we find that $\rho$ is typically large to begin with ($\sim 10^7$) and grows by multiple orders of magnitude as the outer solutions are integrated inward (see Fig. 3) and that its value at $r_*^{\min}$ tends to be within an order of magnitude of $\kappa$. This strongly suggests that, if $\rho$ could be minimized at the starting radius, then $\kappa$ might be greatly reduced in the source region. This guess turns out to be correct.

A linear transformation on the outer boundary conditions can be used to mitigate the ill conditioning [i.e., we are free to choose the starting $b$'s in (A16) to begin solving the recurrence relations]. To see how a choice might be made, we start with the simple basis of (3.9) to form $\mathbf{V}$ [see also Eq. (A20)] and perform a thin-QR decomposition [89]. The matrix is numerically split into a product $\mathbf{V} = \mathbf{QR}$, where $\mathbf{Q}$ is a $4 \times 2$ unitary matrix and $\mathbf{R}$ is a $2 \times 2$ square, upper-triangular matrix. Computed at an initial location $r_*^\infty$, the columns of $\mathbf{Q}$ are an alternative, and in this case orthogonal, basis for beginning an integration for the homogeneous solutions. In other words $\rho(\mathbf{Q}) = 1$. We see that the square matrix $\mathbf{R}$ multiplies $\mathbf{Q}$ from the right to give $\mathbf{V}$ and $\mathbf{R}^{-1}$ multiplies $\mathbf{V}$ from the right to give $\mathbf{Q}$.

In principle, while the columns of $\mathbf{Q}$ (evaluated from $\mathbf{V}$ at finite radius $r_*^\infty$) do indeed give a new orthogonal basis

with unit semicondition number, in practice the use of this basis for boundary conditions on the homogeneous solutions (i.e., replacing $\mathbf{V} \to \mathbf{V}' = \mathbf{Q}$) leads to a separate, serious numerical problem. Because $\mathbf{V}$ is ill conditioned, the numerical construction of $\mathbf{Q}$ at finite radius $r_*^\infty$ will be accompanied by phase and amplitude errors that are well above roundoff, some of which will be consistent with undesired acausal modes (see the similar discussion in the previous subsection). In effect, the numerically derived new basis could not be obtained (to machine accuracy) from an integration of purely outgoing wave solutions at infinity.

Nevertheless, the thin-QR decomposition provides the route forward. The idea is to use the initial choice for $\mathbf{V}$ at $r_*^\infty$ afforded by the simple basis and its related asymptotic expansion. Then the thin-QR decomposition is computed numerically. With this done, we compute from $\mathbf{R}$ its inverse numerically. After that, we use these values of $\mathbf{R}^{-1}$ at $r_*^\infty$ to transform the initial conditions for solving the recurrence relations, and we solve those again. The resulting set of new asymptotic expansions has built into them proper causal behavior and also has $\rho(\mathbf{V}') = 1$. In effect, $\mathbf{R}^{-1}$ serves as a *preconditioner* on the linear system. (Akcay *et al.* [37] use a different means of preconditioning their boundary conditions for the outer solutions.) So we are able to start inward integrations with ideal linear independence (by this measure) and obtain greatly reduced ill conditioning (also by this measure) once the source region is reached (see Fig. 3 and six orders of magnitude improvement). Empirically, we then find the full condition number, $\kappa$, is also improved by orders of magnitude.

Since developing this thin-QR preconditioning technique, we have thus far not been able to find any comparable discussion in the literature.

### 3. Numerical integration

Having set the boundary conditions, our C code uses the Runge–Kutta–Prince–Dormand 7(8) [90] routine rk8pd of the GNU Scientific Library (GSL) [91] to obtain the homogeneous solutions [note that GSL documentation incorrectly labels rk8pd a 8(9) method]. We first integrate the outer homogeneous solutions from $r_*^\infty$ inward and then through the source region to $r_*^{\min}$. We then integrate the inner homogeneous solutions from $r_*^H$ to $r_*^{\min}$. Next, we switch to an integration over $\chi$ to compute Eqs. (3.14) and acquire $C_i^{e/o,\pm}$. In practice, we also find it more efficient to determine the integrands of Eq. (3.14) using an LU decomposition of the Wronskian matrix. Finally, we form the TD EHS as described in Sec. III D.

A final comment is warranted on the integration over the source region and the relative accuracies of various quantities. In the sweep back over the source region, the Wronskian matrix elements are recomputed step by step alongside the normalization functions $c_i^{e/o}(r)$ within a broadened system of ODEs. When the Wronskian matrix is mildly ill conditioned, it becomes impractical to enforce the same accuracy criterion on the normalization coefficients as the homogeneous solutions that make up the elements of the Wronskian. We instead modify the adaptive step size routine to demand high accuracy $\sim 10^{-15}$ for the Wronskian elements while ignoring the fractional errors in the normalization coefficients unless they exceed $\sim 10^{-12}$.
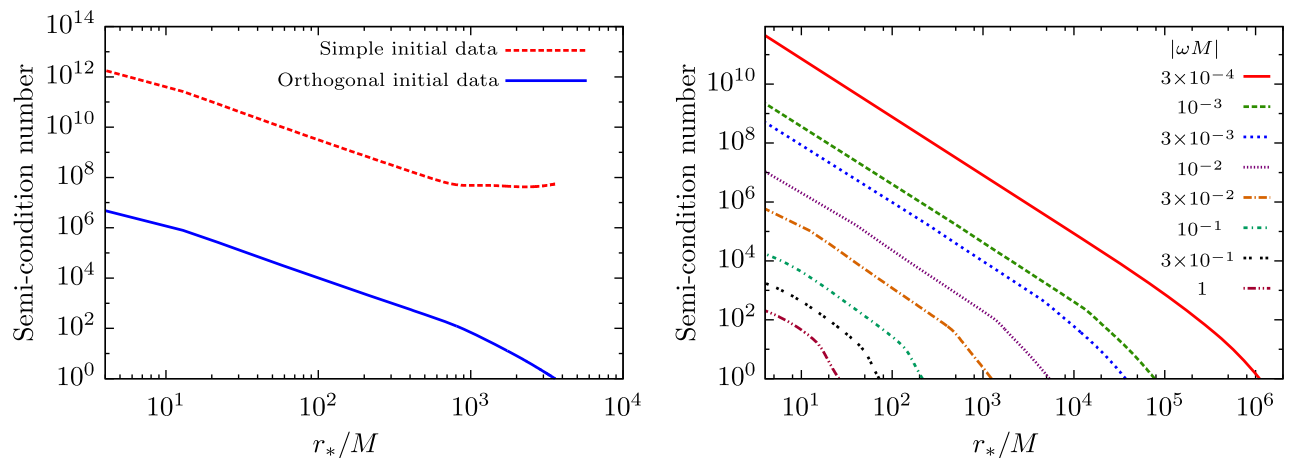


FIG. 3 (color online). Semicondition number growth of outgoing homogeneous solutions and effect of thin-QR preconditioning. The left panel uses the even-parity mode $(l, \omega) = (5, 5 \times 10^{-3} M^{-1})$ and plots as a function of $r_*$ the semicondition number $\rho$ of the matrix $\mathbf{V}$, which is comprised of (the outer solution) half of the Wronskian matrix. Two initial conditions are compared: the simple basis in red (dotted) and the thin-QR preconditioned basis in blue (solid). Orthogonalization with the thin-QR preconditioner makes a more than 5 orders of magnitude improvement. The right panel uses an $l = 16$ even-parity mode and shows the growth of $\rho$ in solutions that start with thin-QR orthogonalized initial conditions, as functions of frequency. Once the frequency reaches $|\omega M| \leq 10^{-4}$, thin-QR preconditioning is no longer sufficient to control the condition number in the source region and still allow double precision computations, and we turn to added techniques.

This criterion does not really diminish the achievable accuracy in the coefficients, since the condition number of the Wronskian may reach or exceed $10^3$ near the low frequency limit of our double precision code (see Sec. IV B for use of quad precision). It does, however, prevent the step size from being driven unreasonably small and halting the integration.

## B. Near-static modes

As mentioned in our step-by-step procedure, near-static modes ($0 < |\omega M| < 10^{-4}$) are a special case subject to separate numerical handling. This problem has also been discussed in Ref. [37]. The ill conditioning associated with the outer homogeneous solutions continues to grow as $\omega \to 0$, despite the application of the orthogonalization technique described in the previous section. To compute modes with $10^{-6} \lesssim |\omega M| \lesssim 10^{-4}$, we make use of three procedures. First, the thin-QR preconditioning discussed in Sec. IV A, which is used for all modes, helps to minimize the semicondition number as much as possible. Second, when a mode with frequency as low as this is encountered, we switch to the use of quad-precision routines to handle integration of the homogeneous solutions and source integrations (i.e., steps 3 and 4). Third, for a given $l, m$, we identify the lowest frequency mode $n = n'$, and for it we bypass the source integration and instead use the jump conditions to provide its normalization.

The semicondition number scales roughly as $\rho \sim 10^2 (M\omega)^{-2}$, as can be seen in Fig. 3. Once the condition number of the Wronskian matrix reaches $\sim 10^{10}$, too many digits ($\sim 10$) are being lost to make double precision calculations viable. Resorting to 128-bit floating point arithmetic is a computationally costly but effective way of proceeding. At quad precision, much higher condition numbers ($\lesssim 10^{22}$) can be tolerated. Our quad-precision implementation is based on modified Numerical Recipes in C [92] routines. We switch to the

Runge–Kutta–Cash–Karp 4(5) method for these calculations. While C compiler support for quad precision is available, its use is computationally costly on 64-bit hardware. Fortunately, for broad regions of orbital parameter space, these modes are few enough that growth in CPU time is manageable (see Fig. 4).

The third element of the procedure focuses on the fact that for a given $l, m$ there is always one $n = n'$ that gives the lowest magnitude frequency, $\omega'$. If $\omega'$ is small enough (and there are others like it for enough other $l$ and $m$), the quad precision integrations over the source might overly dominate the run time of the code. This is particularly a concern for wide separations and large eccentricities. Fortunately, for each $l$ and $m$, there is a way of bypassing the source integration for this one $n'$ mode and obtaining its normalization coefficients more efficiently.

We use odd parity to illustrate the method. For a given $l, m$, the jump conditions in the TD for the MP amplitudes and their derivatives can be written in vector form:

$$[\![\mathcal{B}]\!]_p(t) \equiv \mathcal{B}^+(t, r_p) - \mathcal{B}^-(t, r_p) = \begin{bmatrix} [\![h_t]\!]_p \\ [\![f h_r]\!]_p \end{bmatrix},$$

$$[\![\partial_r \mathcal{B}]\!]_p(t) \equiv \partial_r \mathcal{B}^+(t, r_p) - \partial_r \mathcal{B}^-(t, r_p) = \begin{bmatrix} [\![\partial_r h_t]\!]_p \\ [\![\partial_r (f h_r)]\!]_p \end{bmatrix}.$$

$$(4.4)$$

These jump conditions can be obtained analytically from the field equations and the projections of the stress-energy tensor. They are known to imply that the MP is $C^0$ and the radial derivative jump is some function of time, $\mathcal{J}(t)$. The jump conditions can be written as the difference between the TD EHS or using Eq. (3.16) as the difference of the Fourier sums over FD EHS,
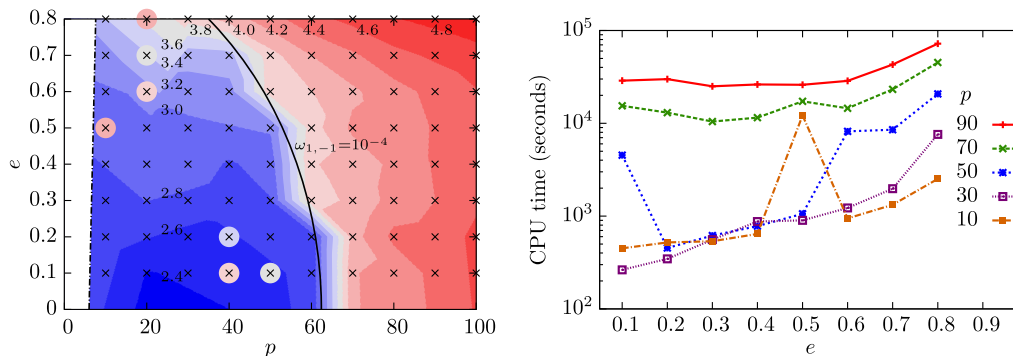


FIG. 4 (color online). Plots of CPU time for GSF calculations as a function of orbital parameter space location. In the left panel, labels give the $\log_{10}$ of CPU time in seconds for each contour. The crosses indicate where models were computed. Every orbit on the right of the solid curve utilizes quad precision. Some orbits on the left lie near resonances, as indicated by local peaks in the contour plot caused by quad precision computing. Slices of CPU time vs $e$ are shown in the right panel. GSF models require single-processor CPU times that range from 4 min to 1 day.

$$\begin{bmatrix} \mathbf{0} \\ \mathcal{J}(t) \end{bmatrix} = \begin{bmatrix} [\![\mathcal{B}]\!]_p(t) \\ [\![\partial_r \mathcal{B}]\!]_p(t) \end{bmatrix}$$

$$= \sum_\omega \left\{ \begin{bmatrix} \tilde{\mathcal{B}}^+(r_p) \\ \partial_r \tilde{\mathcal{B}}^+(r_p) \end{bmatrix} - \begin{bmatrix} \tilde{\mathcal{B}}^-(r_p) \\ \partial_r \tilde{\mathcal{B}}^-(r_p) \end{bmatrix} \right\} e^{-i\omega t}.$$

(4.5)

Normally these conditions are used to check the convergence of the Fourier sums. In the case of a near-static mode, we first normalize all of the other $n \neq n'$ modes in the usual way. Then the near-static mode is split out of the sum in (4.5) and written explicitly in terms of its individual homogeneous solutions and their normalization coefficients,

$$e^{-i\omega' t} \begin{bmatrix} \tilde{\mathcal{B}}_0^+ & \tilde{\mathcal{B}}_1^+ & -\tilde{\mathcal{B}}_0^- & -\tilde{\mathcal{B}}_1^- \\ \partial_r\tilde{\mathcal{B}}_0^+ & \partial_r\tilde{\mathcal{B}}_1^+ & -\partial_r\tilde{\mathcal{B}}_0^- & -\partial_r\tilde{\mathcal{B}}_1^- \end{bmatrix} \begin{bmatrix} C_0^{o,+} \\ C_1^{o,+} \\ C_0^{o,-} \\ C_1^{o,-} \end{bmatrix}$$

$$= \begin{bmatrix} \mathbf{0} \\ \mathcal{J}(t) \end{bmatrix} - \sum_{\omega \neq \omega'} \left\{ \begin{bmatrix} \tilde{\mathcal{B}}^+ \\ \partial_r\tilde{\mathcal{B}}^+ \end{bmatrix} - \begin{bmatrix} \tilde{\mathcal{B}}^- \\ \partial_r\tilde{\mathcal{B}}^- \end{bmatrix} \right\} e^{-i\omega t}. \quad (4.6)$$

In this expression, the function $\mathcal{J}(t)$ is known analytically, and all of the terms in the sum on the right have been computed by the standard procedure. On the left, the homogeneous solutions for $\omega'$ that make up the matrix are computed with quad precision, and what remains are the four unknowns $C_{0/1}^{o,\pm}$. This matrix equation is solved at an arbitrary time $t$, and in doing so we have obtained the normalization coefficients for the troublesome mode without integrating over the source region. It can be applied for frequencies as small as $|\omega| \sim 10^{-6}M^{-1}$.

An objection might be raised that this "spends" the ability to use the jump conditions as a convergence check. But in fact it remains possible to check the jumps at any other time within the radial period $T_r$. Ultimately, the techniques presented in this section can be overwhelmed, since as $T_r$ becomes large the frequency $\Omega_r$ can become smaller than $10^{-4}M^{-1}$, which results in numerous near-static modes per multipole (see Fig. 4).

### C. Static modes with $l \geq 2$

Static modes are another special case and occur when $m = n = 0$. At zero frequency, some of the field amplitudes vanish identically and spur a reduction of order in the constrained field equations and gauge equations. We discuss odd and even parity in turn.

#### 1. Odd-parity static modes

Analytic homogeneous solutions to the static odd-parity Lorenz gauge field equations were first derived by Barack

and Lousto [64]. They showed that $\tilde{h}_r = \tilde{h}_2 = 0$ and wrote down the inner and outer solutions for $\tilde{h}_t$ in terms of finite power series. Here, we express the solution in slightly different form:

$$\tilde{h}_t^- = \frac{r^2}{M} \sum_{k=0}^{l-1} a_k^{\text{odd}} \left(\frac{r}{M}\right)^k,$$

$$\tilde{h}_t^+ = \tilde{h}_t^- \ln f + \frac{M^2}{r} \sum_{k=0}^{l+2} b_k^{\text{odd}} \left(\frac{r}{M}\right)^k. \quad (4.7)$$

The determination of the power series coefficients is described in detail in Appendix B 1.

#### 2. Even-parity static modes

In this paper, we present for the first time analytic solutions for static even-parity modes in Lorenz gauge. (We understand that equivalent analytic solutions have been derived recently by others [93] also.) For static modes in even parity, the reduction $\tilde{h}_{tr} = \tilde{j}_t = 0$ occurs. The reduced constrained equations are sixth order and involve $\tilde{h}_{tt}$, $\tilde{h}_{rr}$, and $\tilde{K}$. We had a novel, if circuitous, route to discovering these analytic solutions, which we now present step by step.

(1) Even-$l$ solution to odd-parity equations: For static modes $m = n = 0$, Eqs. (4.7) are used with odd $l$ to provide a necessary part of the MP. There is, however, nothing to bar us from using an even $l$ in Eqs. (4.7); these, too, are solutions to the odd-parity Lorenz gauge equations even if they serve no purpose in decomposing the MP.

(2) Solution to the Regge–Wheeler equation: Armed with this "even-$l$ solution to the odd-parity Lorenz gauge equations," we next form the gauge-invariant Cunningham–Price–Moncrief (CPM) [94] function

$$\tilde{\Psi}^{\text{odd}}(r) = \frac{r}{\lambda}\left(\frac{d\tilde{h}_t}{dr} - \frac{2}{r}\tilde{h}_t\right). \quad (4.8)$$

Recall that $\lambda = (l+2)(l-1)/2$. This master function satisfies the homogeneous Regge–Wheeler (RW) equation. See also Refs. [31,78].

(3) CPM master function to Zerilli master function: Next use the Detweiler–Chandrasekhar transformation [95–97] to obtain from the CPM function a solution to the homogeneous Zerilli equation,

$$\tilde{\Psi}^{\text{even}}(r) = \frac{1}{\lambda(\lambda+1)}\left[\left(\lambda(\lambda+1) + \frac{9M^2 f}{3Mr + \lambda r^2}\right)\tilde{\Psi}^{\text{odd}} + 3Mf\frac{d\tilde{\Psi}^{\text{odd}}}{dr}\right]. \quad (4.9)$$

(4) MP amplitudes in RW gauge: Use $\tilde{\Psi}^{\text{even}}$ to reconstruct the nonzero even-parity MP amplitudes in RW

gauge. For purposes of presentation, the expressions (see, e.g., Ref. [31]) simplify greatly by using Eqs. (4.8) and (4.9) to write the MP amplitudes in terms of $\tilde{h}_t$,

$$\tilde{K}^{\text{RW}} = \frac{2M}{r^2\lambda}\tilde{h}_t + \left(1 + \frac{2M}{r\lambda}\right)\frac{d\tilde{h}_t}{dr},$$

$$\tilde{h}_{rr}^{\text{RW}} = -\frac{2M}{r^2f^2}\tilde{h}_t + \frac{1}{f}\frac{d\tilde{h}_t}{dr},$$

$$\tilde{h}_{tt}^{\text{RW}} = -\frac{2M}{r^2}\tilde{h}_t + f\frac{d\tilde{h}_t}{dr}, \qquad (4.10)$$

where we have used the homogeneous field equations to remove higher derivatives of $\tilde{h}_t$. Given analytic expressions for the even-$l$ solutions for $\tilde{h}_t$ in step 1, we have obtained even-$l$ static solutions for the MP in RW gauge.

(5) Gauge vector for RW to Lorenz transformation: We next seek a gauge vector to map the even-parity static MPs from RW to Lorenz gauge. The gauge vector will satisfy the wave equation

$$\nabla_\nu \nabla^\nu \Xi_\mu = \nabla^\nu \bar{p}_{\mu\nu}^{\text{RW}}. \qquad (4.11)$$

The generator $\Xi_\mu$ can be decomposed [85] akin to that shown in Sec. II C, and its even-parity part is

$$\Xi_a = \sum_{l,m}[\delta_a{}^t\xi_t^{lm}(t,r) + \delta_a{}^r\xi_r^{lm}(t,r)]Y_{lm},$$

$$\Xi_A = \sum_{l,m}\xi_e^{lm}(t,r)Y_A^{lm}. \qquad (4.12)$$

We insert these into Eq. (4.11) and transform to the FD. Then we specialize to the static case (where $\tilde{\xi}_t = 0$) and are left with two coupled equations (after again dropping $lmn$ indices),

$$\frac{d^2\tilde{\xi}_e}{dr^2} + \frac{2M}{r^2f}\frac{d\tilde{\xi}_e}{dr} - \frac{2(\lambda+1)}{r^2f}\tilde{\xi}_e + \frac{2}{r}\tilde{\xi}_r = 0, \qquad (4.13)$$

$$\frac{d^2\tilde{\xi}_r}{dr^2} + \frac{2}{rf}\frac{d\tilde{\xi}_r}{dr} - \frac{2(\lambda+1)+2f}{r^2f}\tilde{\xi}_r + \frac{4(\lambda+1)}{r^3f}\tilde{\xi}_e$$
$$= \frac{2}{rf}\tilde{h}_{rr}^{\text{RW}} - \frac{2}{rf}\tilde{K}^{\text{RW}} + \frac{d\tilde{h}_{rr}^{\text{RW}}}{dr} - \frac{1}{f}\frac{d\tilde{K}^{\text{RW}}}{dr}, \qquad (4.14)$$

where we have used the homogeneous relation $\tilde{h}_{tt}^{\text{RW}} = f^2\tilde{h}_{rr}^{\text{RW}}$. Solving Eq. (4.13) for $\tilde{\xi}_r$ and inserting into Eq. (4.14) yields a single fourth-order equation. Further, we use Eq. (4.10) and the $\tilde{h}_t$ field

equation to write the source term as a function of $\tilde{h}_t$ and its first derivative:

$$\frac{d^4\tilde{\xi}_e}{dr^4} + \frac{4r - 2M}{r^2f}\frac{d^3\tilde{\xi}_e}{dr^3} - \frac{4r(\lambda+1) - 4M}{r^3f}\frac{d^2\tilde{\xi}_e}{dr^2}$$

$$+ \frac{8M^2 - 4rM(\lambda+2)}{r^5f^2}\frac{d\tilde{\xi}_e}{dr}$$

$$+ \frac{4(\lambda+1)(2M+r\lambda)}{r^5f^2}\tilde{\xi}_e = S_\xi,$$

$$S_\xi \equiv \frac{8M(\lambda+f)}{\lambda f^2 r^4}\tilde{h}_t + \frac{8M}{\lambda f r^3}\frac{d\tilde{h}_t}{dr}. \qquad (4.15)$$

Equation (4.15) has four independent homogeneous solutions denoted by $\tilde{\xi}_{e,H0}^\pm$ and $\tilde{\xi}_{e,H1}^\pm$ and two independent inhomogeneous solutions (since the source has inner and outer instances) denoted by $\tilde{\xi}_{e,I}^\pm$. Here, the superscript $\pm$ indicates the solution that is regular at $r = \infty$ (+) or the horizon (−).

(6) Transformation to six independent Lorenz gauge homogeneous solutions: Once the six solutions for the gauge generator have been obtained, we can use them to transform the even-parity static MP to Lorenz gauge and derive a complete set of homogeneous solutions. The transformation is [78]

$$\tilde{h}_{tt} = \tilde{h}_{tt}^{\text{RW}} + \frac{2Mf}{r^2}\tilde{\xi}_r, \qquad \tilde{h}_{rr} = \tilde{h}_{rr}^{\text{RW}} - \frac{2M}{r^2f}\tilde{\xi}_r - 2\frac{d\tilde{\xi}_r}{dr},$$

$$\tilde{K} = \tilde{K}^{\text{RW}} - \frac{2f}{r}\tilde{\xi}_r + \frac{2(\lambda+1)}{r^2}\tilde{\xi}_e. \qquad (4.16)$$

Note that $\tilde{\xi}_r$ is recovered using Eq. (4.13). We can now switch to the vector notation of Sec. III B and write

$$\tilde{\mathcal{E}} = \tilde{\mathcal{E}}^{\text{RW}} + \boldsymbol{\Delta}\tilde{\boldsymbol{\xi}}, \qquad (4.17)$$

with components

$$\tilde{\mathcal{E}} = r\begin{bmatrix} \tilde{h}_{tt} \\ 0 \\ f^2\tilde{h}_{rr} \\ \tilde{K} \end{bmatrix}, \qquad \boldsymbol{\Delta}\tilde{\boldsymbol{\xi}} \equiv \begin{bmatrix} \frac{2Mf}{r}\tilde{\xi}_r \\ 0 \\ -\frac{2Mf}{r}\tilde{\xi}_r - 2rf^2\frac{d\tilde{\xi}_r}{dr} \\ -2f\tilde{\xi}_r + \frac{2(\lambda+1)}{r}\tilde{\xi}_e \end{bmatrix}, \qquad (4.18)$$

and with $\tilde{\mathcal{E}}^{\text{RW}}$ being obvious. The zeros in the second row follow from $\tilde{h}_{tr}$ vanishing in both Lorenz and RW gauges when $\omega = 0$. We denote the six Lorenz gauge homogeneous solutions by $\tilde{\mathcal{E}}_0^\pm$, $\tilde{\mathcal{E}}_1^\pm$, and $\tilde{\mathcal{E}}_2^\pm$ (recall Sec. III C). The first four Lorenz gauge homogeneous solutions derive from the homogeneous solutions to Eq. (4.15),

$$\tilde{\mathcal{E}}_0^\pm = \Delta\tilde{\xi}_{H0}^\pm, \qquad \tilde{\mathcal{E}}_1^\pm = \Delta\tilde{\xi}_{H1}^\pm. \qquad (4.19)$$

The final two are found by transforming from the RW gauge MP amplitudes of step 4 with the inhomogeneous solutions to Eq. (4.15),

$$\tilde{\mathcal{E}}_2^\pm = \tilde{\mathcal{E}}^{\mathrm{RW},\pm} + \Delta\tilde{\xi}_I^\pm. \qquad (4.20)$$

The extensive expressions for $\tilde{\xi}_{e,H0}^\pm$, $\tilde{\xi}_{e,H1}^\pm$, and $\tilde{\xi}_{e,I}^\pm$ can be found in Appendix B 2.

### D. Low-multipole modes

The low-multipole ($l = 0, 1$) components of the MP are as essential to the GSF as the radiative modes. Solutions were first given by Zerilli [98]. These solutions, specialized to circular orbits, were then transformed to Lorenz gauge by Detweiler and Poisson [99]. Low-multipole mode calculations for circular orbits were considered in Refs. [27,64]. Their solution was extended to eccentric orbits in Refs. [34,37] using the method of EHS.

#### 1. Even-parity dipole mode

In the case of the even-parity dipole mode $l = 1$, $m = 1$, the amplitude $\tilde{G}$ is not defined [see Eq. (2.15) and note that $Y_{AB}$ is not defined for $l < 2$]. The fully constrained field equations (3.4) are unaffected, however. The vanishing of $\tilde{G}$ does add the subtlety that the individual homogeneous solutions to Eq. (3.4) will not, in general, satisfy the Lorenz gauge conditions, Eq. (2.22).

Numerically, the even-parity dipole mode requires no special treatment. As usual, we use Eq. (3.14) to integrate through the source region and find $C_i^{e,\pm}$. We then find that

the solution that results from linear superposition of the normalized modes in Eq. (3.15) *does* satisfy the gauge conditions, a byproduct of the source terms being consistent with the Bianchi identities.

#### 2. Odd-parity dipole mode

In the case of the odd-parity dipole mode $l = 1$, $m = 0$, the amplitude $\tilde{h}_2$ is not defined [see Eq. (2.15) and note that $X_{AB}$ is not defined for $l < 2$]. As with the even-parity case, this does not affect the fully constrained field equations. When $\omega \neq 0$, this mode requires no special treatment. We find that after normalization and superposition the solution does satisfy the gauge condition.

The static mode, $l = 1$, $m = 0$, $n = 0$, must be handled separately. In this case we use the analytic homogeneous solutions [99]

$$\tilde{h}_t^- = \frac{r^2}{M}, \qquad \tilde{h}_t^+ = \frac{M^2}{r} \qquad (4.21)$$

and proceed as usual to obtain the FD EHS.

#### 3. Monopole mode

In the case of the monopole mode, $l = m = 0$, the amplitudes $\tilde{j}_t$, $\tilde{j}_r$, and $\tilde{G}$ are not defined [see Eq. (2.15) and note that $Y_A$ and $Y_{AB}$ are not defined for $l = 0$]. Again, the fully constrained field equations are unaffected, and no special treatment is required to obtain the particular solution as long as $n \neq 0$.

However, the monopole static mode $l = m = n = 0$ is exceptional. The system is fourth order and has four independent homogeneous solutions [100], which also satisfy the Lorenz gauge conditions,

$$\tilde{\mathcal{E}}_0^- = \frac{1}{fr^3}\begin{bmatrix} -Mf^2(r^2 + 2Mr + 4M^2) \\ 0 \\ r^3 - Mr^2 - 2M^2r + 12M^3 \\ f^2r(r^2 + 2Mr + 4M^2) \end{bmatrix}, \qquad \tilde{\mathcal{E}}_0^+ = \frac{1}{f^2r}\begin{bmatrix} f^2(3M - r) \\ 0 \\ M \\ 0 \end{bmatrix}, \qquad \tilde{\mathcal{E}}_1^+ = \frac{1}{f^2r^4}\begin{bmatrix} f^2M^4 \\ 0 \\ M^3(2r - 3M) \\ -rf^2M^3 \end{bmatrix},$$

$$\tilde{\mathcal{E}}_2^+ = \frac{1}{f^2r^4}\begin{bmatrix} Mf^2[r(4M - 3r)(M + r) + (8M^3 - r^3)\ln f + 8M^3\ln(\frac{r}{M})] \\ 0 \\ fr(r^3 - Mr^2 - 2M^2r + 12M^3)\ln f + 8M^3(2r - 3M)\ln(\frac{r}{M}) - Mr(r^2 - 5Mr + 12M^2) \\ f^2r[(r^3 - 8M^3)\ln f - 8M^3\ln(\frac{r}{M}) - Mr(r + 4M)] \end{bmatrix}. \qquad (4.22)$$

Recall from Sec. IV C that $\tilde{h}_{tr}$ vanishes for static modes, as indicated by the zeros in the second rows of these expressions.

We have made a particular choice with this basis. The solutions $\tilde{\mathcal{E}}_1^+$ and $\tilde{\mathcal{E}}_2^+$ are the only independent ones that are regular at $r = \infty$. Then, $\tilde{\mathcal{E}}_0^-$ is the only solution that is

regular at the horizon and does not perturb the mass energy of the black hole [46] (at the horizon). This leaves $\tilde{\mathcal{E}}_0^+$. Ordinarily, we would expect two homogeneous solutions on the horizon side and two on the infinity side. But all that is really required are four independent solutions and regularity. This last solution is independent, and its only

irregularity at $r = \infty$ is the well-known property of Lorenz gauge that $\tilde{h}_{tt}$ approaches a constant as $r \to \infty$ [64]. This behavior leads to a rescaling of the time coordinate [34,37,46,101]], which is necessary for the solution to have the correct mass perturbation $M \to M + \mu\mathcal{E}$ in the region exterior to the particle orbit [99]. With this complete set of homogeneous solutions, we form the FD EHS. Rather than using the expression in Eq. (3.15), for this special case the normalization is

$$\tilde{\mathcal{E}}^-(r) = C_0^{e,-}\tilde{\mathcal{E}}_0^-, \qquad \tilde{\mathcal{E}}^+(r) = \sum_{i=0}^{2} C_i^{e,+}\tilde{\mathcal{E}}_i^+. \quad (4.23)$$

Our route to the solution for this mode differs from that of Akcay *et al.* [37], but of course the two approaches are ultimately equivalent.

## V. ADDITIONAL NUMERICAL RESULTS

We give in this section a sampling of added numerical results from computing the GSF and discuss the range of applicability of the code. As mentioned in the Introduction, astrophysical EMRI sources are expected to have eccentricities as high as $e \simeq 0.8$. This expectation has motivated our effort to develop an efficient and accurate code capable of widely spanning $p$ and $e$ space.

### A. GSF results and their accuracies

We first compare our code to results from Ref. [37] for a mildly eccentric orbit ($e = 0.2$, $p = 7.0$). Table II shows values of the $t$ and $r$ components of both the conservative and dissipative parts of the GSF for a set of locations on the orbit. Our values match closely those of Akcay *et al.* Our results are presented with the number of digits we believe are significant. Their values were presented with uncertainties in the least significant digit, so we have rounded their values and present in the table only fully significant digits for comparison. The two codes agree for this orbit to

within four to seven digits but do differ in many cases in the least significant figure. We estimate errors in our calculation by examining sensitivity in Fourier convergence and in truncating the MSR. The discrepancy between our two codes likely reflects the difficulty in determining *absolute error* when truncating a Fourier sum or power series. In terms of speed, our code generates GSF data rapidly ($\sim 15$ minutes) for an orbit with an eccentricity as low as this. CPU run times can be nearly 2 orders of magnitude greater for high-eccentricity wide-separation orbits (see Fig. 4) where the code begins to switch on intermittent use of quad precision.

We next give in Table III a set of numerical values for the $t$ and $r$ components of the GSF for eccentricity $e = 0.1$ and a range of orbital separations. The full regularized GSF is given at points all around one radial libration. The dissipative and conservative parts can be reconstructed through averaging and differencing values across conjugate points on the orbit using expressions in Sec. II E. The $\varphi$ component of the GSF can be obtained from orthogonality. We list only significant digits. It is clear that for low eccentricity our code generally achieves accuracies of seven to ten decimal places. As we discussed in the Introduction, accuracy of eight or more decimal places is required to keep dephasing errors below $\delta\Phi_r \simeq 10^{-2}$ when $\varepsilon = 10^{-6}$. The requirement is obviously eased if $\varepsilon = 10^{-5}$. The results in Table III indicate that our error criterion is attained for $e = 0.1$. Additional results are provided in Appendix D.

Remarkably, the accuracy of our code improves as the orbital separation increases, as can be seen in Fig. 5. This trend emerges from conflicting aspects of the algorithm. One aspect, as Fig. 3 shows, is that integration from large $r_*$ to the libration region is accompanied by growth in the semi-condition number of the outgoing homogeneous solutions. In integrating from $r_* \sim 10^2 M$ to $r_* \sim 10M$, the semicondition number grows by 2 orders of magnitude. For larger $p$, many modes will thus have smaller $\rho$ in the libration region,

TABLE II. Comparison of GSF data from two different codes. We give self-force values for an orbit with $p = 7.0$ and $e = 0.2$ and present only significant figures for the data from our code (rows without parentheses). Our results are compared to those of Akcay *et al.* [37] (parentheses), where we have rounded the last digit from values in their table to retain only fully significant digits. Our code took approximately 15 min on a single core to generate all of the GSF data in this table.

| $\chi$ | $(M/\mu)^2 F_{\text{cons}}^t$ | $(M/\mu)^2 F_{\text{diss}}^t$ | $(M/\mu)^2 F_{\text{cons}}^r$ | $(M/\mu)^2 F_{\text{diss}}^r$ |
|---|---|---|---|---|
| 0 | 0 | $-4.06328 \times 10^{-3}$ | $3.35760 \times 10^{-2}$ | 0 |
| | (0) | $(-4.063302 \times 10^{-3})$ | $(3.357606 \times 10^{-2})$ | (0) |
| $\pi/4$ | $8.6473 \times 10^{-4}$ | $-2.15691 \times 10^{-3}$ | $2.909881 \times 10^{-2}$ | $4.734956 \times 10^{-3}$ |
| | $(8.6472 \times 10^{-4})$ | $(-2.156923 \times 10^{-3})$ | $(2.909881 \times 10^{-2})$ | $(4.734956 \times 10^{-3})$ |
| $\pi/2$ | $8.28613 \times 10^{-4}$ | $-2.5168 \times 10^{-4}$ | $2.125032 \times 10^{-2}$ | $3.204189 \times 10^{-3}$ |
| | $(8.28611 \times 10^{-4})$ | $(-2.516803 \times 10^{-4})$ | $(2.125034 \times 10^{-2})$ | $(3.204190 \times 10^{-3})$ |
| $3\pi/4$ | $4.60749 \times 10^{-4}$ | $-1.1241 \times 10^{-5}$ | $1.590147 \times 10^{-2}$ | $9.63378 \times 10^{-4}$ |
| | $(4.60750 \times 10^{-4})$ | $(-1.124092 \times 10^{-5})$ | $(1.590149 \times 10^{-2})$ | $(9.633734 \times 10^{-4})$ |
| $\pi$ | 0 | $-3.4613 \times 10^{-5}$ | $1.40888 \times 10^{-2}$ | 0 |
| | (0) | $(-3.461416 \times 10^{-5})$ | $(1.408877 \times 10^{-2})$ | (0) |

TABLE III. GSF results for $e = 0.1$ and a range of $p$. We present the $t$ and $r$ components of the full regularized self-force at a set of points around a complete radial libration. Dissipative and conservative parts can be obtained by addition or subtraction across conjugate points on the orbit according to Eqs. (2.35). The $\varphi$ component can be recovered from the orthogonality relation $F^\alpha u_\alpha = 0$. Results for additional eccentricities are found in Table IV and in Appendix D.

| | $\chi$ | $p = 10$ | $p = 20$ | $p = 30$ | $p = 60$ | $p = 90$ |
|---|---|---|---|---|---|---|
| $F^t$ | 0 | $-2.262915 \times 10^{-4}$ | $-5.259858 \times 10^{-6}$ | $-6.4546731 \times 10^{-7}$ | $-1.919788169 \times 10^{-8}$ | $-2.504370129 \times 10^{-9}$ |
| | $\pi/4$ | $1.198168 \times 10^{-4}$ | $6.729545 \times 10^{-5}$ | $2.7706691 \times 10^{-5}$ | $5.382433506 \times 10^{-6}$ | $2.00678099 \times 10^{-6}$ |
| | $\pi/2$ | $2.767753 \times 10^{-4}$ | $8.716476 \times 10^{-5}$ | $3.4907828 \times 10^{-5}$ | $6.689040469 \times 10^{-6}$ | $2.486733999 \times 10^{-6}$ |
| | $3\pi/4$ | $1.810961 \times 10^{-4}$ | $5.416762 \times 10^{-5}$ | $2.1556094 \times 10^{-5}$ | $4.107340582 \times 10^{-6}$ | $1.524147563 \times 10^{-6}$ |
| | $\pi$ | $-3.133613 \times 10^{-5}$ | $-8.374829 \times 10^{-7}$ | $-1.0622118 \times 10^{-7}$ | $-3.201044762 \times 10^{-9}$ | $-4.156911071 \times 10^{-10}$ |
| | $5\pi/4$ | $-2.601123 \times 10^{-4}$ | $-5.626206 \times 10^{-5}$ | $-2.1821319 \times 10^{-5}$ | $-4.115331358 \times 10^{-6}$ | $-1.525185847 \times 10^{-6}$ |
| | $3\pi/2$ | $-4.334752 \times 10^{-4}$ | $-9.111977 \times 10^{-5}$ | $-3.5403737 \times 10^{-5}$ | $-6.703942473 \times 10^{-6}$ | $-2.488674896 \times 10^{-6}$ |
| | $7\pi/4$ | $-4.52304 \times 10^{-4}$ | $-7.519925 \times 10^{-5}$ | $-2.8683093 \times 10^{-5}$ | $-5.411581273 \times 10^{-6}$ | $-2.010582879 \times 10^{-6}$ |
| $F^r$ | 0 | $1.606774 \times 10^{-2}$ | $4.972162 \times 10^{-3}$ | $2.3630073 \times 10^{-3}$ | $6.306313760 \times 10^{-4}$ | $2.863538695 \times 10^{-4}$ |
| | $\pi/4$ | $1.544991 \times 10^{-2}$ | $4.734491 \times 10^{-3}$ | $2.2459999 \times 10^{-3}$ | $5.984342621 \times 10^{-4}$ | $2.71591791 \times 10^{-4}$ |
| | $\pi/2$ | $1.360189 \times 10^{-2}$ | $4.167538 \times 10^{-3}$ | $1.9721189 \times 10^{-3}$ | $5.238329929 \times 10^{-4}$ | $2.374664601 \times 10^{-4}$ |
| | $3\pi/4$ | $1.180704 \times 10^{-2}$ | $3.628645 \times 10^{-3}$ | $1.7134645 \times 10^{-3}$ | $4.538465637 \times 10^{-4}$ | $2.055245423 \times 10^{-4}$ |
| | $\pi$ | $1.105404 \times 10^{-2}$ | $3.413109 \times 10^{-3}$ | $1.6107881 \times 10^{-3}$ | $4.262250069 \times 10^{-4}$ | $1.929393281 \times 10^{-4}$ |
| | $5\pi/4$ | $1.163054 \times 10^{-2}$ | $3.622782 \times 10^{-3}$ | $1.712561 \times 10^{-3}$ | $4.538069014 \times 10^{-4}$ | $2.055180646 \times 10^{-4}$ |
| | $3\pi/2$ | $1.322747 \times 10^{-2}$ | $4.155439 \times 10^{-3}$ | $1.9702746 \times 10^{-3}$ | $5.237528164 \times 10^{-4}$ | $2.374533990 \times 10^{-4}$ |
| | $7\pi/4$ | $1.506292 \times 10^{-2}$ | $4.722305 \times 10^{-3}$ | $2.244163 \times 10^{-3}$ | $5.983551871 \times 10^{-4}$ | $2.71578943 \times 10^{-4}$ |

leading generally to more accurate GSF values. In contrast, larger radius orbits are more likely to yield near-static modes (see the $M\omega = 10^{-4}$ curve in Fig. 4). Yet, as explained in Sec. IV B, when this occurs the algorithm switches on quad-precision routines for these modes. We posit that the clear benefit of lower semicondition numbers at large $p$ out-weighs difficulties induced by added near-static modes, especially as the algorithm adapts to the presence of these modes. The price to be paid is a significant increase in CPU time as larger $p$ orbits are computed.

The situation changes as we consider higher eccentricities. Table IV shows equivalent information for orbits with $e = 0.5$. At this eccentricity the GSF values have between five and seven decimal places of accuracy. As

before, accuracies improve with wider separations. In Appendix D we provide two more tables, with $e = 0.3$ and $e = 0.7$. At $e = 0.3$ accuracies are intermediate, with six to nine decimal places, but at $e = 0.7$ accuracies drop to three to five significant figures. The trend in accuracy is best displayed semiquantitatively in Fig. 5, where labeled contours trace the isosurfaces of relative error in the GSF. The general trend of improvement in accuracy (in our code) with increasing $p$ is evident, as is the more severe falloff with increasing $e$. It is worth noting how uniform the trends in accuracy are. This uniformity is in contrast to CPU run times seen in Fig. 4, evidence that the code trades speed for accuracy when necessary. With an error goal of $10^{-7}$ (useful if we consider $\varepsilon \gtrsim 10^{-5}$ or are willing to relax to
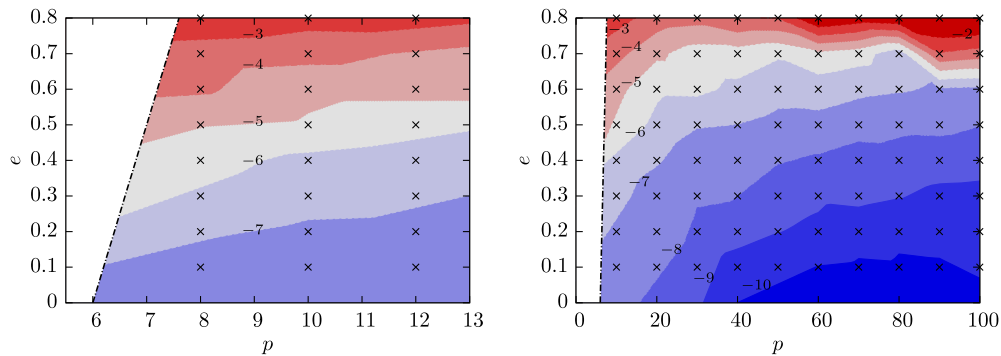


FIG. 5 (color online). Contours of relative errors in the GSF. A grid of orbital parameters is chosen (crosses), and the GSF is calculated. Resulting relative errors are used to generate contour levels of relative accuracy. Numerical labels indicate the $\log_{10}$ of the relative error of each contour.

TABLE IV.  Same as Table III but with $e = 0.5$.

|  | $\chi$ | $p = 10$ | $p = 20$ | $p = 30$ | $p = 60$ | $p = 90$ |
|---|---|---|---|---|---|---|
| $F^t$ | 0 | $-3.6577 \times 10^{-3}$ | $-7.31834 \times 10^{-5}$ | $-8.45794 \times 10^{-6}$ | $-2.403093 \times 10^{-7}$ | $-3.110084 \times 10^{-8}$ |
|  | $\pi/4$ | $2.3230 \times 10^{-3}$ | $5.49789 \times 10^{-4}$ | $2.18176 \times 10^{-4}$ | $4.230920 \times 10^{-5}$ | $1.583867 \times 10^{-5}$ |
|  | $\pi/2$ | $2.1668 \times 10^{-3}$ | $4.64492 \times 10^{-4}$ | $1.79705 \times 10^{-4}$ | $3.379164 \times 10^{-5}$ | $1.251105 \times 10^{-5}$ |
|  | $3\pi/4$ | $6.5637 \times 10^{-4}$ | $1.45139 \times 10^{-4}$ | $5.53475 \times 10^{-5}$ | $1.020907 \times 10^{-5}$ | $3.752960 \times 10^{-6}$ |
|  | $\pi$ | $1.0093 \times 10^{-6}$ | $1.68029 \times 10^{-8}$ | $1.87076 \times 10^{-9}$ | $5.493613 \times 10^{-11}$ | $7.802583 \times 10^{-12}$ |
|  | $5\pi/4$ | $-6.2100 \times 10^{-4}$ | $-1.44416 \times 10^{-4}$ | $-5.52583 \times 10^{-5}$ | $-1.020630 \times 10^{-5}$ | $-3.752584 \times 10^{-6}$ |
|  | $3\pi/2$ | $-1.6155 \times 10^{-3}$ | $-4.54743 \times 10^{-4}$ | $-1.78586 \times 10^{-4}$ | $-3.375934 \times 10^{-5}$ | $-1.250680 \times 10^{-5}$ |
|  | $7\pi/4$ | $-3.3431 \times 10^{-3}$ | $-5.74637 \times 10^{-4}$ | $-2.21391 \times 10^{-4}$ | $-4.240869 \times 10^{-5}$ | $-1.585176 \times 10^{-5}$ |
| $F^r$ | 0 | $3.3855 \times 10^{-2}$ | $9.08159 \times 10^{-3}$ | $4.29527 \times 10^{-3}$ | $1.154902 \times 10^{-3}$ | $5.267282 \times 10^{-4}$ |
|  | $\pi/4$ | $3.0193 \times 10^{-2}$ | $7.61709 \times 10^{-3}$ | $3.56654 \times 10^{-3}$ | $9.498506 \times 10^{-4}$ | $4.317999 \times 10^{-4}$ |
|  | $\pi/2$ | $1.5020 \times 10^{-2}$ | $4.30288 \times 10^{-3}$ | $2.00992 \times 10^{-3}$ | $5.283582 \times 10^{-4}$ | $2.387940 \times 10^{-4}$ |
|  | $3\pi/4$ | $6.3892 \times 10^{-3}$ | $1.86095 \times 10^{-3}$ | $8.61808 \times 10^{-4}$ | $2.238814 \times 10^{-4}$ | $1.007354 \times 10^{-4}$ |
|  | $\pi$ | $3.9352 \times 10^{-3}$ | $1.12769 \times 10^{-3}$ | $5.19946 \times 10^{-4}$ | $1.345001 \times 10^{-4}$ | $6.043324 \times 10^{-5}$ |
|  | $5\pi/4$ | $6.2762 \times 10^{-3}$ | $1.85640 \times 10^{-3}$ | $8.61052 \times 10^{-4}$ | $2.238461 \times 10^{-4}$ | $1.007295 \times 10^{-4}$ |
|  | $3\pi/2$ | $1.3115 \times 10^{-2}$ | $4.24160 \times 10^{-3}$ | $2.00050 \times 10^{-3}$ | $5.279454 \times 10^{-4}$ | $2.387264 \times 10^{-4}$ |
|  | $7\pi/4$ | $2.2613 \times 10^{-2}$ | $7.40405 \times 10^{-3}$ | $3.53587 \times 10^{-3}$ | $9.485827 \times 10^{-4}$ | $4.315958 \times 10^{-4}$ |

$\delta\Phi_r \simeq 10^{-1}$), our code can directly supply the GSF for long-term orbit integrations for $e \lesssim 0.4$–0.5 over most of the range of $p$.

For eccentricities above $e = 0.5$ (or in fact above $e = 0.25$ for $p \lesssim 10$), computing the full GSF accurately is more problematic, and the code, by itself, is not able to meet the goal of $\delta\Phi_r = 0.01$ if $\varepsilon = 10^{-6}$. (For an IMRI, though, with $\varepsilon = 10^{-3}$ we might compute inspirals with eccentricities as high as $e \lesssim 0.5$–0.6.) One recourse would be to switch over much of the computation to 128-bit arithmetic, but doing so on 64-bit architecture would be expensive. So, can eccentricities of $\simeq 0.8$ be reached and still maintain the required error tolerance? We believe the answer is yes and propose a hybrid approach.

The present difficulty stems from asking too much of a single numerical method. Recall that the first-order GSF determines both the adiabatic inspiral and its part of the post-1-adiabatic corrections (with additional correction coming eventually from the orbit-averaged part of the second-order GSF). Hence, we need the code to provide the orbit-averaged part of the first-order GSF to a fractional accuracy $\epsilon_0$ that is $\mathcal{O}(\varepsilon)$ better than the accuracy $\epsilon_1$ it provides in the oscillatory part of the GSF [see the argument centered around Eq. (1.1)]. This viewpoint suggests splitting the task, with a separate code providing the gravitational wave fluxes that drive the inspiral (i.e., post-0-adiabatic) and the Lorenz gauge code providing the conservative and oscillatory part of the dissipative GSF (post-1-adiabatic). In such a hybrid scheme, the present code needs only provide the oscillatory GSF with relative errors of, say, $\epsilon_1 \simeq 10^{-4}$–$10^{-3}$. The flux code would need to give the orbit-averaged force to an accuracy of $\epsilon_0 \lesssim 10^{-8}$. A Regge–Wheeler–Zerilli (RWZ) code can achieve this latter accuracy and would not add significant computational burden.

### B. Improving the GSF with energy and angular momentum fluxes and a hybrid approach

To assess how this hybrid scheme might work, we first discuss how fluxes are extracted from the Lorenz gauge code and compare them to computed local rate of change of work and torque. Energy and angular momentum fluxes can be read off if the asymptotic values of the Zerilli–Moncrief (ZM), $\Psi_{lm}^{\text{even}}$, and CPM, $\Psi_{lm}^{\text{odd}}$, master functions [31,78] are available. When $l + m$ is even, we use $\Psi_{lm} = \Psi_{lm}^{\text{even}}$, and when $l + m$ is odd, we use $\Psi_{lm} = \Psi_{lm}^{\text{odd}}$. Functions are evaluated at both asymptotic limits, with $\Psi_{lm}^{+}$ being the amplitude at $r = \infty$ and $\Psi_{lm}^{-}$ being the one at $r = 2M$. See Ref. [31] and its Sec. IV B for flux expressions in terms of $\Psi_{lm}^{+}$ and $\Psi_{lm}^{-}$.

Expressed in terms of FD amplitudes, the ZM and CPM master functions are related to Lorenz gauge amplitudes by

$$\tilde{\Psi}_{lmn}^{\text{even}}(r) = \frac{r}{\lambda+1}\left[\tilde{K} + \frac{f}{\Lambda}(f\tilde{h}_{rr} - r\partial_r\tilde{K})\right] - \frac{2f}{\Lambda}\tilde{j}_r + r\tilde{G},$$

$$\tilde{\Psi}_{lmn}^{\text{odd}}(r) = \frac{r}{\lambda}\left(\partial_r\tilde{h}_t + i\omega\tilde{h}_r - \frac{2}{r}\tilde{h}_t\right), \qquad (5.1)$$

where we define $\Lambda \equiv \lambda + 3M/r$. The master functions have asymptotic running wave behavior $\tilde{\Psi}_{lmn}^{\pm}(r_* \to \pm\infty) = C_{lmn}^{\pm}e^{\pm i\omega r_*}$ and the coefficients can be obtained from the asymptotic behavior of the Lorenz gauge amplitudes. [Note, the $C_{lmn}^{\pm}$ here are not the same as those in Eq. (3.14).] Having made these connections to Lorenz gauge, we use standard expressions for the fluxes:

$$\langle \dot{E} \rangle = \sum_{lmn} \frac{\omega_{mn}^2}{64\pi} \frac{(l+2)!}{(l-2)!} (|C_{lmn}^+|^2 + |C_{lmn}^-|^2),$$

$$\langle \dot{L} \rangle = \sum_{lmn} \frac{m\omega_{mn}}{64\pi} \frac{(l+2)!}{(l-2)!} (|C_{lmn}^+|^2 + |C_{lmn}^-|^2). \qquad (5.2)$$

In a geodesic GSF code, the fluxes should match the orbit-averaged rate of work and torque that are computed locally at the particle via Eq. (2.41). The dissipative GSF can be split into sums over *tensor* spherical harmonic and FD contributions, each of which can be taken to be a function of $\chi$,

$$F_{\text{diss}}^{\alpha}(\chi) = \sum_{lmn} F_{lmn}^{\alpha,\text{diss}}(\chi). \qquad (5.3)$$

This decomposition of $F_{\text{diss}}^{\alpha}$ can be substituted into the integrals in Eq. (2.41) to yield the orbit-averaged rates of change of energy and angular momentum. It is possible though to reverse the order of sum and integration and derive individual $l, m$ contributions to the rate of work and torque:

$$\langle \dot{\mathcal{E}} \rangle = \sum_{lm} \langle \dot{\mathcal{E}} \rangle_{lm} = \frac{2}{T_r} \sum_{lmn} \left( \int_0^\pi \frac{f_p}{\mu u^t} \frac{dt}{d\chi} F_{lmn}^{t,\text{diss}} d\chi \right),$$

$$\langle \dot{\mathcal{L}} \rangle = \sum_{lm} \langle \dot{\mathcal{L}} \rangle_{lm} = \frac{2}{T_r} \sum_{lmn} \left( \int_0^\pi \frac{r_p^2}{\mu u^t} \frac{dt}{d\chi} F_{lmn}^{\varphi,\text{diss}} d\chi \right). \qquad (5.4)$$

Moreover, the force can be evaluated on either side of the particle and should yield the same rates of change (up to numerical errors). Balance between fluxes and local dissipation occurs mode by mode, i.e., $\langle \dot{E} \rangle_{lm} = -\mu \langle \dot{\mathcal{E}} \rangle_{lm}$ and $\langle \dot{L} \rangle_{lm} = -\mu \langle \dot{\mathcal{L}} \rangle_{lm}$. Alternatively, we can compare them after summing over all modes.

Table V compares the balance between fluxes and local dissipation for several $p = 10$ orbits with different eccentricities. For low eccentricity ($e = 0.1$) we see a high degree of fidelity between the local dissipation, computed on both sides of the particle, and the fluxes derived from the Lorenz gauge fields. The comparison continues to hold, but the accuracy drops markedly as orbits with $e = 0.5$ and $e = 0.7$ are considered. We also then show the results of computing the fluxes with a RWZ code [31] and a Teukolsky code [102]. Much smaller fractional errors, $\simeq 10^{-10}$–$10^{-9}$, are typically obtained, a result due at least in part to computing more $l, m$ modes.

A hybrid method would make use of the substantially smaller relative error $\epsilon_0 \simeq 10^{-10}$–$10^{-9}$ of a RWZ code to provide the orbit-averaged first-order GSF. A question arises, however, as to what exactly orbit-averaged means. Pound and Poisson [103] discuss various secular and radiative approximations. As they point out, an average $\langle F_R^\alpha \rangle_\chi$ over $\chi$ is not the same as, for example, the average $\langle F_R^\alpha \rangle_t$ over $t$. A hybrid method would use a very specific average. A glance at (2.41) shows that the net fluxes will be balanced by integrals over *proper time* $\tau$ of the relevant *covariant* components of the dissipative part, $F_\alpha^{\text{diss}}$, of the GSF. These averages are then related to fluxes by

$$\langle \dot{E} \rangle_{\text{flux}} = -\mu \langle \dot{\mathcal{E}} \rangle_{\text{diss}} = \frac{1}{T_r} \int_0^{\mathcal{T}_r} F_t^{\text{diss}} d\tau = \frac{\mathcal{T}_r}{T_r} \langle F_t^{\text{diss}} \rangle_\tau,$$

$$\langle \dot{L} \rangle_{\text{flux}} = -\mu \langle \dot{\mathcal{L}} \rangle_{\text{diss}} = -\frac{1}{T_r} \int_0^{\mathcal{T}_r} F_\varphi^{\text{diss}} d\tau = -\frac{\mathcal{T}_r}{T_r} \langle F_\varphi^{\text{diss}} \rangle_\tau,$$

$$(5.5)$$

where $\mathcal{T}_r$ is the lapse of proper time in one radial orbit. If we assume that the fluxes are computed with a RWZ code, we can infer from them an orbit-averaged dissipative force

TABLE V. Comparisons between energy and angular momentum fluxes and locally computed dissipation. Several orbits with $p = 10$ and differing eccentricities are considered. Local changes in energy and angular momentum (computed with the GSF on both sides of the particle) are compared to total fluxes radiated to infinity and down the horizon. One set of fluxes is calculated using the present GSF code by extracting asymptotic values of the Lorenz gauge amplitudes. These results are then compared to published values that were computed using RWZ and Teukolsky codes. The changes in energy are measured in units of $M^2/\mu^2$, while the changes in angular momentum are measured in units of $M/\mu^2$.

| | | $e = 0.1$ | $e = 0.5$ | $e = 0.7$ |
|---|---|---|---|---|
| $-\mu\langle\dot{\mathcal{E}}^+\rangle$ | This paper | $6.3190584052 \times 10^{-5}$ | $9.2871 \times 10^{-5}$ | $9.49 \times 10^{-5}$ |
| $-\mu\langle\dot{\mathcal{E}}^-\rangle$ | This paper | $6.3190584053 \times 10^{-5}$ | $9.2871 \times 10^{-5}$ | $9.49 \times 10^{-5}$ |
| $\langle\dot{E}\rangle$ | This paper | $6.319058405374 \times 10^{-5}$ | $9.287477 \times 10^{-5}$ | $9.5052 \times 10^{-5}$ |
| $\langle\dot{E}\rangle$ | Hopper and Evans | $6.319058405375 \times 10^{-5}$ | $9.287480002 \times 10^{-5}$ | $9.505332849 \times 10^{-5}$ |
| $\langle\dot{E}\rangle$ | Fujita *et al.* | $6.3190584054 \times 10^{-5}$ | $9.287480001 \times 10^{-5}$ | $9.505332847 \times 10^{-5}$ |
| $-\mu\langle\dot{\mathcal{L}}^+\rangle$ | This paper | $1.9531904845 \times 10^{-3}$ | $1.9765 \times 10^{-3}$ | $1.63 \times 10^{-3}$ |
| $-\mu\langle\dot{\mathcal{L}}^-\rangle$ | This paper | $1.9531904845 \times 10^{-3}$ | $1.9765 \times 10^{-3}$ | $1.63 \times 10^{-3}$ |
| $\langle\dot{L}\rangle$ | This paper | $1.95319048455 \times 10^{-3}$ | $1.976807 \times 10^{-3}$ | $1.6348 \times 10^{-3}$ |
| $\langle\dot{L}\rangle$ | Hopper and Evans | $1.95319048455 2 \times 10^{-3}$ | $1.976807667 \times 10^{-3}$ | $1.634854630 \times 10^{-3}$ |

$$\langle F_t^{\text{diss}}\rangle_{\text{RWZ}} = \frac{T_r}{\mathcal{T}_r}\langle \dot{E}\rangle_{\text{RWZ}}, \qquad \langle F_\varphi^{\text{diss}}\rangle_{\text{RWZ}} = -\frac{T_r}{\mathcal{T}_r}\langle \dot{L}\rangle_{\text{RWZ}},$$

$$(5.6)$$

with vanishing $r$ component. The process of constructing the hybrid force involves first taking the GSF from the Lorenz gauge code and constructing the oscillatory part

$$F_\alpha^{\text{osc}} = F_\alpha^{\text{cons}} + F_\alpha^{\text{diss}} - \langle F_\alpha^{\text{diss}}\rangle_\tau, \qquad (5.7)$$

by computing the $\tau$ average of the full force (the conservative part has zero mean) and subtracting it off. The hybrid GSF is then the sum of the dissipative term from a RWZ code and the oscillatory part from the Lorenz gauge code

$$F_\alpha^{\text{hybrid}} = \langle F_\alpha^{\text{diss}}\rangle_{\text{RWZ}} + F_\alpha^{\text{osc}}. \qquad (5.8)$$

If the Lorenz gauge code and the RWZ code were to have comparable accuracies, this construction would have little value. But circumstances are different if the RWZ code can provide the average force, which drives secular changes, with relative errors as small as $\epsilon_0 \simeq 10^{-10}$–$10^{-9}$, while the Lorenz code supplies the oscillatory part of the GSF with relative errors of $\epsilon_1 \sim 10^{-10}$–$10^{-3}$ (depending on eccentricity). Substantially tighter tolerance, and hence smaller $\epsilon_0$, is required on the former because the secular changes drive a large accumulation in the orbital phase $\Phi_r \simeq 1/\varepsilon$ in a long-term evolution. The oscillatory part contributes to $\kappa_1$, and its fractional errors $\epsilon_1$ need only be $\lesssim 10^{-3} \lesssim \delta\Phi_r$, consistent with the criterion outlined in the Introduction.

## VI. CONCLUSIONS AND FUTURE WORK

We have described in this paper the key elements in our development of a FD method to compute the gravitational self-force in Lorenz gauge. With this method we have extended the region in $p$ and $e$ of orbital parameter space within which accurate GSF results can be obtained. The GSF can be calculated out to $p \simeq 100$ and up to $e \simeq 0.5$ (with this code alone). New features in our approach include (1) use of fully constrained Lorenz gauge equations for both odd and even parity, (2) discovery of analytic solutions for arbitrary-$l$ even-parity static modes, (3) development of a thin-QR preconditioning technique for orthogonalizing outer homogeneous solutions and reducing condition number, (4) adaptive use of quad-precision arithmetic to maintain accuracy of near-static modes, (5) an application of the jump conditions to avoid source integration for the lowest frequency mode, and (6) outlining a proposal for a novel hybrid approach to combine the Lorenz gauge code with a RWZ code to allow GSF calculation up to $e \simeq 0.8$.

This last proposal is an important idea to explore next and should be done in the context of using our code with a separate osculating orbits code to revisit long-term orbit evolutions [36]. Our existing Lorenz gauge code, with minor tightening of tolerances, should be able to push to inspirals of orbits that start with $e \simeq 0.5$. By including parallel computation of radiative modes with an existing, separate RWZ code, we should be able to reach initial orbits with $e \simeq 0.8$, near the peak in the expected EMRI distribution.

An ambitious downstream effort would involve finding some way to include the orbit-averaged second-order GSF (i.e., second-order fluxes). Preliminary work is underway [104] with applications to circular orbits on a Schwarzschild background [74,105]. If it proves possible to find and implement such a scheme, we would be able to compute inspirals accurately enough for matched filtering and detector applications (within the restrictions of a Schwarzschild background and no spin in the secondary body).

A more immediate next application might involve the inclusion of spin in the small body and calculating not just the regularized perturbation of the spin precession for circular orbits [106] but for eccentric orbits also. More generally, the code might be used as a laboratory to explore other self-interaction effects, like tidal moments [107], with attention to their behavior in eccentric orbits. We anticipate also using the code to explore overlap with a newly developed MST code that uses analytic function expansions to find the GSF for eccentric orbits [54].

## APPENDIX A: ASYMPTOTIC BOUNDARY CONDITIONS

We give here the recurrence relations for asymptotic and Taylor expansions that provide boundary conditions for mode integrations. Expansions about $r_* = \pm\infty$ for homogeneous Lorenz gauge solutions were first given by Akcay [32] but with a different initial basis and for a larger,

partially constrained even-parity system. The fully constrained even-parity system we use makes the generic recurrence relations valid for $l = 0, 1$ modes when $\omega \neq 0$. Throughout this section we use $\sigma = M\omega$ for brevity.

### 1. Near-horizon even-parity Taylor expansions

The even-parity homogeneous solutions can be expanded around $r = 2M$ in a Taylor series in powers of $f(r)$:

$$\tilde{\mathcal{E}}^- = r \begin{bmatrix} \tilde{h}_{tt} \\ f\tilde{h}_{tr} \\ f^2\tilde{h}_{rr} \\ \tilde{K} \end{bmatrix} = Me^{-i\omega r_*} \sum_{k=0}^{\infty} \begin{bmatrix} a_k^{(tt)} \\ a_k^{(tr)} \\ a_k^{(rr)} \\ a_k^{(K)} \end{bmatrix} f^k. \tag{A1}$$

Recurrence relations for the coefficients can be found via the method of Frobenius:

$$\begin{bmatrix} 1+8i\sigma+2k(k-2-4i\sigma) & -8i\sigma & -1 & 0 \\ -2i\sigma & k(k-2)-4i\sigma(k-1) & -2i\sigma & 0 \\ -1 & -8i\sigma & 1+8i\sigma+2k(k-2-4i\sigma) & 0 \\ -k+1+2i\sigma & -4i\sigma & -k-1+2i\sigma & k(k-4i\sigma) \end{bmatrix} \begin{bmatrix} a_k^{(tt)} \\ a_k^{(tr)} \\ a_k^{(rr)} \\ a_k^{(K)} \end{bmatrix} = \begin{bmatrix} A_k^{(tt)} \\ A_k^{(tr)} \\ A_k^{(rr)} \\ A_k^{(K)} \end{bmatrix}. \tag{A2}$$

The rhs contains only lower-order coefficients in the expansion

$$\begin{aligned}
A_k^{(tt)} &\equiv [-4i(k-4)\sigma + 2k(5k-34) + 3l(l+1) + 113]2a_{k-3}^{(tt)} - 2[2k(5k-6i\sigma-26) + 3l(l+1) + 36i\sigma + 65]a_{k-2}^{(tt)} \\
&\quad + [2k(5k-12i\sigma-18) + 2l(l+1) + 48i\sigma + 29]a_{k-1}^{(tt)} + [2(42-5k)k - 2l(l+1) - 173]a_{k-4}^{(tt)} - 8i\sigma a_{k-3}^{(tr)} \\
&\quad + 24i\sigma a_{k-2}^{(tr)} - 24i\sigma a_{k-1}^{(tr)} + (2(k-5)^2 - 1)a_{k-5}^{(tt)} + 3a_{k-5}^{(rr)} - 11a_{k-4}^{(rr)} + 14a_{k-3}^{(rr)} - 6a_{k-2}^{(rr)} - a_{k-1}^{(rr)} - 4a_{k-6}^{(K)} \\
&\quad + 16a_{k-5}^{(K)} - 24a_{k-4}^{(K)} + 16a_{k-3}^{(K)} - 4a_{k-2}^{(K)}, \\
A_k^{(tr)} &\equiv [5k^2 - 4i(3k-7)\sigma - 20k + l^2 + l + 16]a_{k-1}^{(tr)} + [2k(5k-2i\sigma-40) + 3(l^2+l+52) + 20i\sigma]a_{k-3}^{(tr)} \\
&\quad + [2k(-5k+6i\sigma+30) - 3l(l+1) - 44i\sigma - 84]a_{k-2}^{(tr)} + [-5(k-10)k - l(l+1) - 124]a_{k-4}^{(tr)} - 4i\sigma a_{k-3}^{(tt)} \\
&\quad + 10i\sigma a_{k-2}^{(tt)} - 8i\sigma a_{k-1}^{(tt)} - 4i\sigma a_{k-3}^{(rr)} + 10i\sigma a_{k-2}^{(rr)} - 8i\sigma a_{k-1}^{(rr)} - 4i\sigma a_{k-4}^{(K)} + 8i\sigma a_{k-3}^{(K)} - 4i\sigma a_{k-2}^{(K)} + (k-6)^2 a_{k-5}^{(tr)}, \\
A_k^{(rr)} &\equiv 2[-4i(k-5)\sigma + 10(k-8)k + 3l(l+1) + 155]a_{k-3}^{(rr)} - 2[2k(5k-6i\sigma-30) + 3l(l+1) + 44i\sigma + 83]a_{k-2}^{(rr)} \\
&\quad + [2k(5k-12i\sigma-20) + 2l(l+1) + 56i\sigma + 33]a_{k-1}^{(rr)} + [-10(k-10)k - 2l(l+1) - 249]a_{k-4}^{(rr)} \\
&\quad + (-24k + 8i\sigma + 74)a_{k-3}^{(tt)} + 2(8k-8i\sigma-17)a_{k-2}^{(tt)} + (-4k+8i\sigma+3)a_{k-1}^{(tt)} - 24i\sigma a_{k-3}^{(tr)} + 56i\sigma a_{k-2}^{(tr)} \\
&\quad - 40i\sigma a_{k-1}^{(tr)} + 8(6k-2i\sigma-21)a_{k-4}^{(K)} + (-32k+32i\sigma+80)a_{k-3}^{(K)} + 4(2k-4i\sigma-3)a_{k-2}^{(K)} + (19-4k)a_{k-5}^{(tt)} \\
&\quad + (16k-63)a_{k-4}^{(tt)} + (2(k-12)k+73)a_{k-5}^{(rr)} + (8k-44)a_{k-6}^{(K)} + (144-32k)a_{k-5}^{(K)}, \\
A_k^{(K)} &\equiv [5k^2 - 2k(5+6i\sigma) + l^2 + l + 16i\sigma + 4]a_{k-1}^{(K)} + [2k(-5k+6i\sigma+20) - 3(l^2+l+12) - 32i\sigma]a_{k-2}^{(K)} \\
&\quad + [2k(5k-2i\sigma-30) + 3l(l+1) + 16i\sigma + 84]a_{k-3}^{(K)} + [-5(k-8)k - l(l+1) - 76]a_{k-4}^{(K)} \\
&\quad + (6k-2i\sigma-15)a_{k-2}^{(tt)} + (-4k+4i\sigma+7)a_{k-1}^{(tt)} + 4i\sigma a_{k-2}^{(tr)} - 8i\sigma a_{k-1}^{(tr)} + (6k-2i\sigma-9)a_{k-2}^{(rr)} \\
&\quad + (4i\sigma-4k+1)a_{k-1}^{(rr)} + (k-4)a_{k-4}^{(tt)} + (13-4k)a_{k-3}^{(tt)} + (k-4)a_{k-4}^{(rr)} + (11-4k)a_{k-3}^{(rr)} + (k-6)(k-4)a_{k-5}^{(K)}. \tag{A3}
\end{aligned}$$

In these recurrence relations, a coefficient vanishes any time a negative index appears. Because the matrix is singular when $k \leq 2$, the first few terms are evaluated separately:

$$a_0^{(tr)} = a_0^{(tt)}, \qquad a_0^{(rr)} = a_0^{(tt)}, \qquad a_1^{(tr)} = -\frac{l(l+1)+1}{1+4i\sigma}a_0^{(tt)}, \qquad a_1^{(rr)} = -\frac{2(l(l+1)+1)}{1+4i\sigma}a_0^{(tt)} - a_1^{(tt)},$$

$$a_1^{(K)} = -\frac{4(l(l+1)+1)}{1+16\sigma^2}a_0^{(tt)} + \left(\frac{l(l+1)}{1-4i\sigma}-1\right)a_0^{(K)} - \frac{2}{1-4i\sigma}a_1^{(tt)},$$

$$a_2^{(tr)} = \frac{l^2(l+1)^2 - 8i\sigma(l(l+1)+1) + 16\sigma^2}{4i\sigma(1+16\sigma^2)}a_0^{(tt)} - \frac{1}{1-4i\sigma}a_0^{(K)} + \frac{l(l+1)-1}{1-4i\sigma}a_1^{(tt)} - a_2^{(tt)},$$

$$a_2^{(rr)} = -\frac{2(l(l+1)+1)(l(l+1)-3)}{1+16\sigma^2}a_0^{(tt)} + 2\left(1+\frac{1}{1-4i\sigma}\right)a_0^{(K)} - \frac{2(l(l+1)-1)}{1-4i\sigma}a_1^{(tt)} + a_2^{(tt)},$$

$$a_2^{(K)} = \frac{-4(l(l+1)-11)(l(l+1)+1)\sigma - i(3l(l(3l(l+2)+1)-2)-16)+16i\sigma^2}{8\sigma(1+8\sigma(2\sigma+i))+4i}a_0^{(tt)}$$

$$- \frac{(l(l+1)+4i\sigma)^2 - 36i\sigma + 12}{4(8\sigma^2+6i\sigma-1)}a_0^{(K)} + \frac{2l(l+1)(1-i\sigma)+4i\sigma-1}{8\sigma^2+6i\sigma-1}a_1^{(tt)} + a_2^{(tt)}. \tag{A4}$$

The freely chosen coefficients $a_0^{(tt)}$, $a_1^{(tt)}$, $a_2^{(tt)}$, and $a_0^{(K)}$ control the boundary conditions. For example, at leading order we can choose the simple basis

$$(a_0^{(tt)}, a_1^{(tt)}, a_2^{(tt)}, a_0^{(K)}) = (1,0,0,0) \rightarrow (\tilde{\mathcal{E}}_0^-)^\top \sim (1,1,1,0)e^{-i\omega r_*}$$

$$(a_0^{(tt)}, a_1^{(tt)}, a_2^{(tt)}, a_0^{(K)}) = (0,1,0,0) \rightarrow (\tilde{\mathcal{E}}_1^-)^\top \sim (1,0,-1,-2(1-4i\sigma)^{-1})fe^{-i\omega r_*},$$

$$(a_0^{(tt)}, a_1^{(tt)}, a_2^{(tt)}, a_0^{(K)}) = (0,0,1,0) \rightarrow (\tilde{\mathcal{E}}_2^-)^\top \sim (1,-1,1,1)f^2 e^{-i\omega r_*},$$

$$(a_0^{(tt)}, a_1^{(tt)}, a_2^{(tt)}, a_0^{(K)}) = (0,0,0,1) \rightarrow (\tilde{\mathcal{E}}_3^-)^\top \sim (0,0,0,1)e^{-i\omega r_*}. \tag{A5}$$

## 2. Near-horizon odd-parity Taylor expansions

The odd-parity homogeneous solutions can also be expanded around $r = 2M$ in powers of $f(r)$:

$$\tilde{\mathcal{B}}^- = \begin{bmatrix} \tilde{h}_t \\ f\tilde{h}_r \end{bmatrix} = Me^{-i\omega r_*}\sum_{k=0}^{\infty}\begin{bmatrix} a_k^{(t)} \\ a_k^{(r)} \end{bmatrix}f^k. \tag{A6}$$

Recurrence relations for the coefficients are again found via the method of Frobenius:

$$\begin{bmatrix} k(k-1-4i\sigma)+2i\sigma & -2i\sigma \\ -2i\sigma & k(k-1-4i\sigma)+2i\sigma \end{bmatrix}\begin{bmatrix} a_k^{(t)} \\ a_k^{(r)} \end{bmatrix}$$

$$= \begin{bmatrix} A_k^{(t)} \\ A_k^{(r)} \end{bmatrix}. \tag{A7}$$

Once again these result in a linear system to be solved, and the rhs has only lower-order coefficients:

$$A_k^{(t)} \equiv (4k^2 - 22k + l^2 + l + 24)a_{k-3}^{(t)}$$

$$- 2[k(3k-2i\sigma-12) + l^2 + l + 5i\sigma + 9]a_{k-2}^{(t)}$$

$$+ [2k(2k-4i\sigma-5) + l^2 + l + 12i\sigma + 4]a_{k-1}^{(t)}$$

$$+ 2i\sigma a_{k-2}^{(r)} - 4i\sigma a_{k-1}^{(r)} - (k-5)(k-2)a_{k-4}^{(t)},$$

$$A_k^{(r)} \equiv -2[k(3k-2i\sigma-15) + l^2 + l + 7i\sigma + 15]a_{k-2}^{(r)}$$

$$+ [4k(k-2i\sigma-3) + l^2 + l + 16i\sigma + 6]a_{k-1}^{(r)}$$

$$+ [4(k-7)k + l^2 + l + 42]a_{k-3}^{(r)} + 6i\sigma a_{k-2}^{(t)}$$

$$- 8i\sigma a_{k-1}^{(t)} - (k-6)(k-3)a_{k-4}^{(r)}. \tag{A8}$$

Any negative-index coefficients vanish. This linear system is singular for $k \leq 1$, and starting conditions for the recursion are calculated separately:

$$a_0^{(r)} = a_0^{(t)}, \qquad a_1^{(r)} = -\frac{(l+2)(l-1)}{2i\sigma}a_0^{(t)} - a_1^{(t)}. \tag{A9}$$

The freely chosen coefficients $a_0^{(t)}$ and $a_1^{(t)}$ control the boundary conditions. We can choose a simple basis, which at leading order has the form

$$(a_0^{(t)}, a_1^{(t)}) = (1,0) \rightarrow (\tilde{\boldsymbol{B}}_0^-)^\top \sim (1,1)e^{-i\omega r_*},$$

$$(a_0^{(t)}, a_1^{(t)}) = (0,1) \rightarrow (\tilde{\boldsymbol{B}}_1^-)^\top \sim (1,-1)fe^{-i\omega r_*}. \quad \text{(A10)}$$

In practical applications, we evaluate these expansions at $r_* = -6M$ and add terms in the series until the relative size of the last term drops below machine precision.

### 3. Near-infinity even-parity asymptotic expansions

The even-parity homogeneous solutions can be expanded about $r = \infty$ as

$$\tilde{\mathcal{E}}^+ = r \begin{bmatrix} \tilde{h}_{tt} \\ f\tilde{h}_{tr} \\ f^2\tilde{h}_{rr} \\ \tilde{K} \end{bmatrix} = Me^{i\omega r_*} \sum_{k=0}^{k_{\max}} \begin{bmatrix} b_k^{(tt)} \\ b_k^{(tr)} \\ b_k^{(rr)} \\ b_k^{(K)} \end{bmatrix} \left(\frac{M}{r}\right)^k. \quad \text{(A11)}$$

Recurrence relations for the coefficients are a linear system of equations:

$$\begin{bmatrix} -2i\sigma k & 0 & 0 & 0 \\ -i\sigma & 2i\sigma(k-1) & -i\sigma & -2i\sigma \\ 2i\sigma & 4i\sigma & -2i\sigma(k-1) & -4i\sigma \\ -i\sigma & -2i\sigma & -i\sigma & -2i\sigma(k-1) \end{bmatrix} \begin{bmatrix} b_k^{(tt)} \\ b_k^{(tr)} \\ b_k^{(rr)} \\ b_k^{(K)} \end{bmatrix}$$

$$= \begin{bmatrix} B_k^{(tt)} \\ B_k^{(tr)} \\ B_k^{(rr)} \\ B_k^{(K)} \end{bmatrix}. \quad \text{(A12)}$$

As with the horizon-side expansions, the rhs groups all of the lower-order coefficients

$$B_k^{(tt)} \equiv [-k^2 - 4i(k-2)\sigma + k + l^2 + l]b_{k-1}^{(tt)} - 2[(7-2k)k + l^2 + l - 5]b_{k-2}^{(tt)} + 4i\sigma b_{k-1}^{(tr)}$$
$$\quad - 2[2(k-6)k + 17]b_{k-3}^{(tt)} - 6b_{k-3}^{(rr)} + 4b_{k-2}^{(rr)} - 16b_{k-4}^{(K)} + 16b_{k-3}^{(K)} - 4b_{k-2}^{(K)},$$

$$B_k^{(tr)} \equiv 2[(11-2k)k + l^2 + l - 15]b_{k-2}^{(tr)} + [k(k+4i\sigma - 3) - l(l+1) - 12i\sigma + 2]b_{k-1}^{(tr)}$$
$$\quad - 4i\sigma b_{k-1}^{(tt)} - 4i\sigma b_{k-1}^{(rr)} + 8i\sigma b_{k-2}^{(K)} - 8i\sigma b_{k-1}^{(K)} + 4(k-4)^2 b_{k-3}^{(tr)},$$

$$B_k^{(rr)} \equiv [-k^2 - 4i(k-3)\sigma + 3k + l^2 + l - 4]b_{k-1}^{(rr)} - 2[(11-2k)k + l^2 + l - 17]b_{k-2}^{(rr)}$$
$$\quad + 2(k+2i\sigma)b_{k-1}^{(tt)} + 12i\sigma b_{k-1}^{(tr)} + 4(6k+4i\sigma - 11)b_{k-2}^{(K)} - 4(k+4i\sigma - 1)b_{k-1}^{(K)} + (8k-22)b_{k-3}^{(tt)}$$
$$\quad + (12-8k)b_{k-2}^{(tt)} + (-4(k-8)k - 66)b_{k-3}^{(rr)} + 16(2k-7)b_{k-4}^{(K)} + (128-48k)b_{k-3}^{(K)},$$

$$B_k^{(K)} \equiv [-k(k+4i\sigma - 3) + l^2 + l + 8i\sigma - 2]b_{k-1}^{(K)} - 2[(9-2k)k + l^2 + l - 9]b_{k-2}^{(K)}$$
$$\quad + 2(k-2)b_{k-2}^{(tt)} - kb_{k-1}^{(tt)} + 2(k-2)b_{k-2}^{(rr)} + (2-k)b_{k-1}^{(rr)} - 4(k-4)(k-2)b_{k-3}^{(K)}. \quad \text{(A13)}$$

All appearances of a negative index imply a vanishing coefficient. The linear system is singular here when $k \le 2$ and starting coefficients are obtained from the reduced equations

$$b_0^{(rr)} = -b_0^{(tt)} - 2b_0^{(tr)}, \qquad b_0^{(K)} = 0, \qquad b_1^{(tt)} = -\frac{l(l+1) + 4i\sigma}{2i\sigma}b_0^{(tt)} - 2b_0^{(tr)},$$

$$b_1^{(rr)} = \frac{l(l+1) + 4(1+i\sigma)}{2i\sigma}b_0^{(tt)} + 2\left(1 + \frac{1}{i\sigma}\right)b_0^{(tr)} - 2b_1^{(tr)}, \qquad b_1^{(K)} = -\frac{1}{i\sigma}b_0^{(tt)} + \frac{(l+2)(l-1)}{2i\sigma}b_0^{(tr)} + b_1^{(tr)},$$

$$b_2^{(tt)} = -\frac{l(l+1)((l+2)(l-1) + 8i\sigma) + 4i\sigma}{8\sigma^2}b_0^{(tt)} + \frac{l(l+1) + 2}{2i\sigma}b_0^{(tr)} - b_1^{(tr)},$$

$$b_2^{(tr)} = -\frac{1}{i\sigma}b_0^{(tt)} + \frac{l(l+1)(l+2)(l-1) + 4i\sigma(l(l+1) + 3)}{8\sigma^2}b_0^{(tr)} - \left(1 + \frac{l(l+1)}{2i\sigma}\right)b_1^{(tr)},$$

$$b_2^{(rr)} = \frac{l(l+1)((l+2)(l-1) + 8i\sigma) + 20i\sigma}{8\sigma^2}b_0^{(tt)} + \frac{l(l+1)((l+2)(l-1) - 2i\sigma) + 8i\sigma}{4\sigma^2}b_0^{(tr)} + 3b_1^{(tr)} - 2b_2^{(K)}. \quad \text{(A14)}$$

The freely chosen coefficients $b_0^{(tt)}$, $b_0^{(tr)}$, $b_1^{(tr)}$, and $b_2^{(K)}$ control the boundary conditions, and a simple choice for the basis gives the following lowest-order form:

$$(b_0^{(tt)}, b_0^{(tr)}, b_1^{(tr)}, b_2^{(K)}) = (1,0,0,0) \rightarrow (\tilde{\mathcal{E}}_0^+)^\top \sim (1,0,-1,0)e^{i\omega r_*},$$

$$(b_0^{(tt)}, b_0^{(tr)}, b_1^{(tr)}, b_2^{(K)}) = (0,1,0,0) \rightarrow (\tilde{\mathcal{E}}_1^+)^\top \sim (0,1,-2,0)e^{i\omega r_*},$$

$$(b_0^{(tt)}, b_0^{(tr)}, b_1^{(tr)}, b_2^{(K)}) = (0,0,1,0) \rightarrow (\tilde{\mathcal{E}}_2^+)^\top \sim (0,1,-2,1)r^{-1}e^{i\omega r_*},$$

$$(b_0^{(tt)}, b_0^{(tr)}, b_1^{(tr)}, b_2^{(K)}) = (0,0,0,1) \rightarrow (\tilde{\mathcal{E}}_3^+)^\top \sim (0,0,-2,1)r^{-2}e^{i\omega r_*}. \tag{A15}$$

Note though that, as described in Sec. IV A, we take this simple basis and apply a linear transformation called thin-QR preconditioning.

### 4. Near-infinity odd-parity asymptotic expansions

The odd-parity homogeneous solutions can be expanded about $r = \infty$ as

$$\tilde{\mathcal{B}}^+ = \begin{bmatrix} \tilde{h}_t \\ f\tilde{h}_r \end{bmatrix} = Me^{i\omega r_*} \sum_{k=0}^{k_{\max}} \begin{bmatrix} b_k^{(t)} \\ b_k^{(r)} \end{bmatrix} \left(\frac{M}{r}\right)^k. \tag{A16}$$

Again, the recurrence relations are found to satisfy a linear system,

$$\begin{bmatrix} -2ik\sigma & 0 \\ -2i\sigma & 2i\sigma(k-1) \end{bmatrix} \begin{bmatrix} b_k^{(t)} \\ b_k^{(r)} \end{bmatrix} = \begin{bmatrix} B_k^{(t)} \\ B_k^{(r)} \end{bmatrix}, \tag{A17}$$

where again the rhs contains all lower-order coefficients,

$$B_k^{(t)} \equiv [l(l+1) - k(k + 4i\sigma - 1) + 6i\sigma]b_{k-1}^{(t)}$$
$$- 2[l(l+1) - 2(k-3)k - 2]b_{k-2}^{(t)} + 2i\sigma b_{k-1}^{(r)}$$
$$- 4(k-4)(k-1)b_{k-3}^{(t)},$$

$$B_k^{(r)} \equiv [k(k + 4i\sigma - 3) - l(l+1) - 10i\sigma + 2]b_{k-1}^{(r)}$$
$$- 2[2(k-5)k - l(l+1) + 10]b_{k-2}^{(r)}$$
$$- 6i\sigma b_{k-1}^{(t)} + 4(k-5)(k-2)b_{k-3}^{(r)}, \tag{A18}$$

and any negative index that appears implies a vanishing coefficient. This linear system is singular for $k \leq 1$, and starting conditions are evaluated individually:

$$b_0^{(r)} = -b_0^{(t)}, \qquad b_1^{(t)} = -\frac{l(l+1)}{2i\sigma}b_0^{(t)}. \tag{A19}$$

The freely chosen coefficients $b_0^{(t)}$ and $b_1^{(r)}$ determine the boundary conditions, and a simple choice for the basis yields the following lowest-order form:

$$(b_0^{(t)}, b_1^{(r)}) = (1,0) \rightarrow (\tilde{\mathcal{B}}_0^+)^\top \sim (1,-1)e^{i\omega r_*}$$

$$(b_0^{(t)}, b_1^{(r)}) = (0,1) \rightarrow (\tilde{\mathcal{B}}_1^+)^\top \sim (0,1)r^{-1}e^{i\omega r_*}. \tag{A20}$$

As with even parity, the method described in Sec. IV A transforms this simple basis to a more orthogonal one using thin-QR preconditioning.

With these asymptotic series, care must be exercised with the number of terms and the starting radius $r_*^\infty$. The test for convergence is whether a numerical integration through a distance $\sim\omega^{-1}$ starting with an initial evaluation of the asymptotic expansion agrees with a second evaluation of the expansion at the end point of the trial. If the test fails, we increase $r_*^\infty$ by some factor (say $\sim 1.5$) and repeat.

## APPENDIX B: HOMOGENEOUS STATIC MODES

Here, we provide the details of the power series used to construct exact analytic homogeneous solutions for static modes when $l \geq 2$, as were discussed in Sec. IV C. Throughout this section we set $\rho = r/M$. Regularity at $\rho = 2$ and $\rho = \infty$ governs our choice for inner and outer solutions.

### 1. Odd parity

In Sec. IV C we gave expressions for $\tilde{h}_t^-$ and $\tilde{h}_t^+$ as finite sums. The coefficients in those sums are

$$a_k^{\text{odd}} = \frac{3(-1)^k 2^{1-k}(l+k+1)!}{l(l+1)k!(k+3)!(l-k-1)!}, \tag{B1}$$

$$b_0^{\text{odd}} = \frac{96}{l^2(l+1)^2(l+2)(l-1)},$$

$$b_1^{\text{odd}} = \frac{24}{l^2(l+1)^2}, \qquad b_2^{\text{odd}} = \frac{6}{l(l+1)},$$

$$b_3^{\text{odd}} = \frac{1}{l(l+1)} + \frac{11}{6} - 2H_l,$$

$$b_k^{\text{odd}} = \frac{1}{-4k(k-3)}[4(k-3)a_{k-4}^{\text{odd}} + (12-8k)a_{k-3}^{\text{odd}}$$
$$+ (12 - 7k + k^2 - l(l+1))b_{k-2}^{\text{odd}}$$
$$+ 2(10k - 2k^2 - 10 + l(l+1))b_{k-1}^{\text{odd}}], \tag{B2}$$

where $H_k$ is the $k^{\text{th}}$ harmonic number defined as

$$H_k \equiv \begin{cases} 0, & k = 0 \\ \sum_{j=1}^k j^{-1}, & k \geq 1 \end{cases}. \tag{B3}$$

We have found the expression for $\tilde{h}_t^+$ in Eq. (4.7) to be impractical to use numerically for large $r$ because of a large

number of cancellations between the two sums. We instead reexpand the solution as an infinite series,

$$\tilde{h}_t^+ = \frac{M}{\rho^l} \sum_{k=0}^{\infty} \frac{d_k^{\text{odd}}}{\rho^k},$$

$$d_k^{\text{odd}} = \frac{2^{2l+k+1}(l+k+1)!(l+k-2)!\Gamma(l+3/2)}{k!(l+1)(l-2)!(2l+k+1)!\sqrt{\pi}}, \quad (B4)$$

which agrees with the expression in Eq. (4.7) up to a constant factor. This is a convergent Taylor series if $\rho > 2$.

### 2. Even parity

As summarized in Sec. IV C, we find the even-parity static modes through a series of steps. We give here the complete expressions for the gauge variables $\tilde{\xi}_{e,H0}^{\pm}$, $\tilde{\xi}_{e,H1}^{\pm}$, and $\tilde{\xi}_{e,I}^{\pm}$ that are defined in that section. We construct power series expansions, and we seek series that are exact solutions with finite numbers of terms. This condition imposes constraints on otherwise freely chosen coefficients. The variables $\tilde{\xi}_{e,H0}^{\pm}$ are found from the finite sums

$$\tilde{\xi}_{H0}^- = M^2 \sum_{k=0}^{l} a_k^{H0} \rho^k, \qquad \tilde{\xi}_{H0}^+ = \tilde{\xi}_{H0}^- \ln f + M^2 \sum_{k=0}^{l-1} b_k^{H0} \rho^k, \quad (B5)$$

where the coefficients $a_k^{H0}$ and $b_k^{H0}$ are given by the closed-form expressions

$$a_k^{H0} = \frac{(-1)^k (l+k)!}{2^k (k!)^2 (l-k)!}, \qquad b_k^{H0} = 2a_k^{H0}(H_k - H_l). \quad (B6)$$

In practice, we find the above expression for $\tilde{\xi}_{H0}^+$ to be impractical to use numerically due to a large number of cancellations between the two sums. Instead we use the following equivalent Taylor series, which converges for all $\rho > 2$:

$$\tilde{\xi}_{H0}^+ = \frac{M^2}{\rho^{l+1}} \sum_{k=0}^{\infty} \frac{d_k^{H0}}{\rho^k}, \qquad d_k^{H0} = \frac{(-1)^{l+1} 2^{l+k+1} [(l+k)!]^2}{k!(2l+k+1)!}. \quad (B7)$$

The variables $\tilde{\xi}_{e,H1}^{\pm}$ are given by

$$\tilde{\xi}_{H1}^- = \tilde{\xi}_{H0}^- \ln \rho + M^2 \sum_{k=0}^{l+2} a_k^{H1} \rho^k,$$

$$\tilde{\xi}_{H1}^+ = \tilde{\xi}_{H0}^- \left[ \text{Li}_2(f) - \frac{1}{2}\ln\left(\frac{\rho}{4}\right)\ln f - \frac{\pi^2}{6} - \frac{a_{l+2}^{H1} + a_{l+1}^{H1} + b_l^{H1}}{a_l^{H0}} \right] + \frac{1}{2}\tilde{\xi}_{H0}^+ \ln \rho - \frac{1}{2}\tilde{\xi}_{H1}^- \ln f + M^2 \sum_{k=0}^{l+1} b_k^{H1} \rho^k, \quad (B8)$$

where we have introduced the dilogarithm function $\text{Li}_2(f) \equiv - \int_0^f x^{-1} \ln(1-x) dx$, and the coefficients follow from the recurrences

$$a_0^{H1} = 0, \quad a_1^{H1} = l(l+1) + \frac{1}{2}, \quad a_2^{H1} = \frac{1}{16}(2 - l(-2 + l(1 + 3l(2 + l)))),$$

$$a_3^{H1} = -\frac{1}{8} - \frac{1}{12}l + \frac{539}{864}l^2 + \frac{91}{288}l^3 - \frac{7}{216}l^4 + \frac{11}{288}l^5 + \frac{11}{864}l^6,$$

$$8(-3+k)(-2+k)k^2 a_k^{H1} = 2(-7+2k)(11 + (-7+k)k - l(1+l))a_{k-3}^{H0}$$
$$- 2(-99k^2 + 12k^3 - 4k(-65 + 2l(1+l)) + 3(-72 + 7l(1+l)))a_{k-2}^{H0}$$
$$+ 4(-68 + 2k(65 + 6(-6+k)k) + 7l - 4kl + (7-4k)l^2)a_{k-1}^{H0}$$
$$- 8k(12 + k(-15+4k))a_k^{H0} + (-5+k-l)(-3+k-l)(-4+k+l)(-2+k+l)a_{k-3}^{H1}$$
$$- 2(128 - 33k^3 + 3k^4 + (-5+l)l(1+l)(6+l) - 2k^2(-65 + 2l(1+l)) + 3k(-72 + 7l(1+l)))a_{k-2}^{H1}$$
$$+ 4(24 + (-4+k)k(17 + 3(-4+k)k) - 7l + (7-2k)kl + (-7 + (7-2k)k)l^2)a_{k-1}^{H1},$$

$$b_0^{H1} = 0, \quad b_1^{H1} = -\frac{1}{2}(1 + H_l(2l(l+1)+1)),$$

$$b_2^{H1} = \frac{1}{16}\left(\frac{6 + l - 27l^2 - 16l^3}{l(l+1)} + H_l(-2 + l(-2 + l(1 + 3l(2+l))))\right),$$

$$b_3^{H1} = \frac{216 + l(216 + l(-656 + l(-1229 + l(-1279 + l(-463 + 27l)))))}{1728 l(l+1)}$$
$$+ \frac{H_l}{864}(-180 + l(-120 + l(613 + l(495 + l(28 - 11l(3+l)))))), \quad (B9)$$

$$8(-3+k)(-2+k)k^2 b_k^{H1} = -4(-3+k)a_{k-2}^{H0} + 2(-7+4k)a_{k-1}^{H0} - 4(-3+k)(8+(-6+k)k-l(1+l))a_{k-2}^{H1}$$
$$+ 2(-51k^2 + 8k^3 + 7(-8+l+l^2) + k(99-4l(1+l)))a_{k-1}^{H1} - 4k(12+k(-15+4k))a_k^{H1}$$
$$+ (-7+2k)(11+(-7+k)k-l(1+l))b_{k-3}^{H0}$$
$$+ (99k^2 - 12k^3 + 4k(-65+2l(1+l)) - 3(-72+7l(1+l)))b_{k-2}^{H0}$$
$$+ 2(-68+2k(65+6(-6+k)k)+7l-4kl+(7-4k)l^2)b_{k-1}^{H0} - 4k(12+k(-15+4k))b_k^{H0}$$
$$+ (-5+k-l)(-3+k-l)(-4+k+l)(-2+k+l)b_{k-3}^{H1}$$
$$- 2(128-33k^3 + 3k^4 + (-5+l)l(1+l)(6+l) - 2k^2(-65+2l(1+l)) + 3k(-72+7l(1+l)))b_{k-2}^{H1}$$
$$+ 4(24+(-4+k)k(17+3(-4+k)k) - 7l+(7-2k)kl+(-7+(7-2k)k)l^2)b_{k-1}^{H1}. \tag{B10}$$

As with $\tilde{\xi}_{H0}^+$, we find the expression for $\tilde{\xi}_{H1}^+$ to be impractical for numerical use at large radius and replace it with a convergent Taylor series [this expression for $\tilde{\xi}_{H1}^+$ is equivalent to that in Eq. (B8) up to a linear combination with $\tilde{\xi}_{H0}^+$]:

$$\tilde{\xi}_{H1}^+ = \frac{1}{2}\tilde{\xi}_{H0}^+ \ln\rho + \frac{M^2}{\rho^{l-1}}\sum_{k=0}^{\infty} \frac{d_k^{H1}}{\rho^k},$$

$$d_0^{H1} = \frac{3+8l+4l^2}{4l}d_0^{H0}, \qquad d_1^{H1} = \frac{l^2+l-1}{l}d_0^{H1}, \qquad d_2^{H1} = 0,$$

$$(-2+k)k(-1+k+2l)(1+k+2l)d_k^{H1} = 2(-3+k+l)(3+4k^2+l(-9+4l)+k(-9+8l))d_{k-4}^{H0}$$
$$- (-2+8k^3+3k^2(-9+8l)+l(27-26l+4l^2)+k(22-58l+20l^2))d_{k-3}^{H0}$$
$$+ (-1+2k+2l)(-1-2l+k(-1+k+2l))d_{k-2}^{H0} - 4(-3+k+l)^2(-1+k+l)(k+l)d_{k-2}^{H1}$$
$$+ 2((-2+k)k(1+k(-5+2k))-6l+k(27+k(-29+8k))l+2(-2+k)(-3+5k)l^2+2(-3+2k)l^3)d_{k-1}^{H1}. \tag{B11}$$

The remaining unknown gauge variables are $\tilde{\xi}_{e,I}^\pm$, which satisfy the inhomogeneous ODE, Eq. (4.15). To find expressions for them, we must first write the source term of that equation as a power series. The source term that is regular at the horizon is

$$S_\xi^- = \frac{1}{M^2\rho^3 f^2}\sum_{k=0}^{l} y_k^- \rho^k, \qquad y_k^- = \begin{cases} -\frac{96}{(l+2)(l-1)} & k=0 \\ \frac{8a_{k-1}^{\text{odd}}(2(k+1)+l(l+1))-32(k+3)a_k^{\text{odd}}}{(l+2)(l-1)} & 0<k<l \\ \frac{8(l+1)}{l-1}a_{l-1}^{\text{odd}} & k=l \end{cases} \tag{B12}$$

The corresponding term that is regular at infinity is

$$S_\xi^+ = S_\xi^- \ln f + \frac{1}{M^2\rho^5 f^2}\sum_{k=0}^{l+2} y_k^+ \rho^k, \qquad y_k^+ = \begin{cases} \frac{8(l(l+1)+2(k-1))b_k^{\text{odd}}-32(k+1)b_{k+1}^{\text{odd}}}{(l+2)(l-1)} & k=0,1 \\ \frac{8(l(l+1)+2(k-1))b_k^{\text{odd}}-32(k+1)b_{k+1}^{\text{odd}}+32a_{k-2}^{\text{odd}}}{(l+2)(l-1)} & 1<k<l+2 \\ \frac{8(l+1)}{l-1}b_{l+2}^{\text{odd}} & k=l+2 \end{cases} \tag{B13}$$

With these in hand, we can write power series for $\tilde{\xi}_{e,I}^\pm$,

$$\tilde{\xi}_{e,I}^- = M^2\rho^2 \sum_{k=0}^{l} a_k^I \rho^k, \qquad \tilde{\xi}_{e,I}^+ = \tilde{\xi}_{e,I}^- \ln f + \beta\tilde{\xi}_{H0}^- \ln f + M^2 \sum_{k=0}^{l+1} b_k^I \rho^k, \tag{B14}$$

where $\beta \equiv -3072(l(l+1)-7)/[l^4(l+1)^4(l+7)(l+2)(l-1)]$. The coefficients follow from the recurrences

$$a_0^I = -\frac{12}{(l+2)(l+1)l(l-1)}, \qquad a_1^I = -\frac{2}{l(l+1)},$$

$$4k(k-1)(k+2)^2 a_k^I = y_{k-1}^- - (k-l-2)(k-l)(k+l-1)(k+l+1)a_{k-2}^I - 2(l+l^2-2-k^3-2k^4+k(1+l+l^2)$$
$$+2k^2(2+l+l^2))a_{k-1}^I, \tag{B15}$$

$$b_0^I = \sum_{k=0}^{l} \frac{2^{k+2}}{k+2} a_k^I + \beta \sum_{k=1}^{l} \frac{2^k}{k} a_k^{H0}, \qquad b_1^I = \frac{1}{4}(-3l(l+1)\beta + 2\beta a_1^{H0} - 2l(l+1)b_0^I) + \frac{1}{8}y_0^+,$$

$$b_2^I = \beta\left[\frac{3}{32}(2-3l-2l^2+2l^3+l^4) + \frac{1}{2l(l+1)}\left(-\frac{2-3l-2l^2+2l^3+l^4}{8}a_1^{H0} + \frac{2+5l+5l^2}{2}a_2^{H0} + 9a_3^{H0}\right)\right]$$
$$+\frac{l(l+1)(l+2)(l-1)}{16}b_0^I + \frac{1}{2l(l+1)}\left(\frac{2+5l+5l^2}{2}a_0^I + 9a_1^I - \frac{2-3l-2l^2+2l^3+l^4}{32}y_0^+ - \frac{1}{8}y_1^+ + \frac{1}{4}y_2^+\right),$$

$$b_3^I = \sum_{k=2}^{l} \frac{2^{k-1}}{k-1} a_k^I + \beta \sum_{k=4}^{l} \frac{2^{k-3}}{k-3} a_k^{H0},$$

$$8k^2(k-2)(k-3)b_k^I$$
$$= 2y_{k-1}^+ - y_{k-2}^+ + 8(-3+k)[8+(-6+k)k-l(1+l)]a_{k-4}^I$$
$$+4[51k^2-8k^3-7(-8+l+l^2)+k(-99+4l(1+l))]a_{k-3}^I + 8k[-4+4(-2+k)^2+k]a_{k-2}^I$$
$$-2[128-33k^3+3k^4+(-5+l)l(1+l)(6+l)-2k^2(-65+2l(1+l))+3k(-72+7l(1+l))]b_{k-2}^I$$
$$+4[24+(-4+k)k(17+3(-4+k)k)-7l+(7-2k)kl+(-7+(7-2k)k)l^2]b_{k-1}^I$$
$$+(-5+k-l)(-3+k-l)(-4+k+l)(-2+k+l)b_{k-3}^I + 8\beta(-3+k)[8+(-6+k)k-l(1+l)]a_{k-2}^{H0}$$
$$+4\beta[51k^2-8k^3-7(-8+l+l^2)+k(-99+4l(1+l))]a_{k-1}^{H0} + 8\beta k[12+k(-15+4k)]a_k^{H0}. \tag{B16}$$

We have found the expressions for $S_\xi^+$ and $\tilde{\xi}_{e,I}^+$ in Eqs. (B13) and (B14) to also be impractical for numerical use at large $r$. Again, we replace them with infinite series. For the source term, we have

$$S_\xi^+ = \frac{1}{M^2 \rho^{l+4} f^2} \sum_{k=0}^{\infty} \frac{v_k}{\rho^k}, \qquad v_k = \frac{2^{2l+k+4} l(l+k)[(l+k-1)!]^2 \Gamma(l+3/2)}{(l+2)k!(l-1)!(2l+k+1)!\sqrt{\pi}}, \tag{B17}$$

while for $\tilde{\xi}_{e,I}^+$ we use

$$\tilde{\xi}_{e,I}^+ = \frac{M^2}{\rho^{l-1}} \sum_{k=0}^{\infty} d_k^I \frac{1}{\rho^k},$$

$$d_0^I = \frac{2-l^2}{4l(l+1)}v_0 + \frac{1}{4l}v_1, \qquad d_1^I = -\frac{l^3-3l+2}{4l^2}v_0 + \frac{l(l+1)-1}{4l^2}v_1, \qquad d_2^I = 0,$$

$$k(k-2)(-1+k+2l)(1+k+2l)d_k^I = v_{k-1} - 4(-3+k+l)^2(-1+k+l)(k+l)d_{k-2}^I$$
$$+2[(k-2)k(1+k(2k-5))+(-1+k)(6+k(-21+8k))l+2(-2+k)(-3+5k)l^2+2(-3+2k)l^3]d_{k-1}^I, \tag{B18}$$

which agrees with (B14) up to a constant factor and linear combination with $\tilde{\xi}_{H0}^+$. It is important when constructing the "plus-side" solutions to use either Eqs. (4.7), (B8), and (B14) or Eqs. (B4), (B11), and (B18). Mixing these sets of equations will introduce an inconsistency.

## APPENDIX C: EXPLICIT FORM OF THE FORCE TERMS $f_n^\alpha$

Here, we give the explicit form of the various force terms $f_n^\alpha$ defined in Sec. II E. Only the $t$ and $r$ components are necessary. The $\theta$ component vanishes, and the $\varphi$ component can be derived from the other two. These functions depend upon the position on the orbit, the constants of motion, and the MP amplitudes and their first derivatives. There is implied dependence on $l$ and $m$:

$$f_0^t = \left[\frac{im\mathcal{E}\mathcal{L}(3f_p + U_p^2 - 2\mathcal{E}^2)}{4f_p^3} - \frac{M\mathcal{E}^2(3f_p + U_p^2 - 4\mathcal{E}^2)\dot{r}_p}{2f_p^5}\right]h_{tt} + \frac{r_p^2(f_p(U_p^2 + \mathcal{E}^2) - f_p^2 + \mathcal{E}^2(U_p^2 - 2\mathcal{E}^2))}{4f_p^4}\partial_t h_{tt}$$

$$+ \frac{r_p^2\mathcal{E}^2(3f_p + U_p^2 - 2\mathcal{E}^2)\dot{r}_p}{4f_p^4}\partial_r h_{tt} + \left[\frac{im\mathcal{E}\mathcal{L}(f_p + U_p^2 - 2\mathcal{E}^2)}{4f_p} + \frac{M\mathcal{E}^2(f_p + U_p^2)\dot{r}_p}{2f_p^3}\right]h_{rr}$$

$$+ \frac{r_p^2(f_p + \mathcal{E}^2)(f_p + U_p^2 - 2\mathcal{E}^2)}{4f_p^2}\partial_t h_{rr} + \frac{r_p^2\mathcal{E}^2(f_p + U_p^2 - 2\mathcal{E}^2)\dot{r}_p}{4f_p^2}\partial_r h_{rr}$$

$$+ \left[-\frac{M(f_p U_p^2 + \mathcal{E}^2 U_p^2 - 2\mathcal{E}^4)}{f_p^3} + \frac{im\mathcal{E}\mathcal{L}(f_p - \mathcal{E}^2)\dot{r}_p}{f_p^3}\right]h_{tr} - \frac{r_p^2\mathcal{E}^4\dot{r}_p}{f_p^4}\partial_t h_{tr} + \frac{r_p^2(f_p - \mathcal{E}^2)(\mathcal{E}^2 - U_p^2)}{f_p^2}\partial_r h_{tr}$$

$$+ \left[-\frac{m^2\mathcal{L}^2(f_p - \mathcal{E}^2)}{r_p^2 f_p^2} + \frac{im\mathcal{E}\mathcal{L}(\mathcal{E}^2 f_p - 2f_p^2 + \mathcal{E}^2)\dot{r}_p}{r_p f_p^4}\right]j_t - \frac{im\mathcal{E}^3\mathcal{L}}{f_p^3}\partial_t j_t + \frac{im\mathcal{E}\mathcal{L}(f_p - \mathcal{E}^2)\dot{r}_p}{f_p^3}\partial_r j_t$$

$$+ \left[\frac{im\mathcal{E}\mathcal{L}(-5f_p U_p^2 + 4\mathcal{E}^2 f_p + U_p^2)}{2r_p f_p^2} + \frac{m^2\mathcal{E}^2\mathcal{L}^2\dot{r}_p}{r_p^2 f_p^2}\right]j_r - \frac{im\mathcal{E}\mathcal{L}(f_p + \mathcal{E}^2)\dot{r}_p}{f_p^3}\partial_t j_r - \frac{im\mathcal{E}\mathcal{L}(\mathcal{E}^2 - U_p^2)}{f_p}\partial_r j_r$$

$$+ \frac{im\mathcal{E}\mathcal{L}(f_p - U_p^2)}{2f_p^2}K + \frac{r_p^2(f_p - U_p^2)(f_p + \mathcal{E}^2)}{2f_p^3}\partial_t K + \frac{r_p^2\mathcal{E}^2(f_p - U_p^2)\dot{r}_p}{2f_p^3}\partial_r K$$

$$+ \left[\frac{im(m^2 + 4)\mathcal{E}\mathcal{L}^3}{4r_p^2 f_p} - \frac{m^2\mathcal{E}^2\mathcal{L}^2\dot{r}_p}{r_p f_p^2}\right]G + \frac{m^2\mathcal{L}^2(f_p + \mathcal{E}^2)}{4f_p^2}\partial_t G + \frac{m^2\mathcal{E}^2\mathcal{L}^2\dot{r}_p}{4f_p^2}\partial_r G, \tag{C1}$$

$$f_1^t = \left[-\frac{im\mathcal{E}\mathcal{L}^3}{4r_p^2 f_p^2} + \frac{M\mathcal{E}^2\mathcal{L}^2\dot{r}_p}{2r_p^2 f_p^4}\right]h_{tt} - \frac{\mathcal{L}^2(f_p + \mathcal{E}^2)}{4f_p^3}\partial_t h_{tt} - \frac{\mathcal{E}^2\mathcal{L}^2\dot{r}_p}{4f_p^3}\partial_r h_{tt}$$

$$+ \left[\frac{im\mathcal{E}\mathcal{L}^3}{4r_p^2} + \frac{\mathcal{E}^2\mathcal{L}^2(1 - 5f_p)\dot{r}_p}{4r_p f_p^2}\right]h_{rr} + \frac{\mathcal{L}^2(f_p + \mathcal{E}^2)}{4f_p}\partial_t h_{rr} + \frac{\mathcal{E}^2\mathcal{L}^2\dot{r}_p}{4f_p}\partial_r h_{rr}$$

$$+ \frac{\mathcal{L}^2(f_p - \mathcal{E}^2)}{r_p f_p}h_{tr} - \frac{im\mathcal{E}\mathcal{L}^3}{r_p^3}j_r + \frac{\mathcal{E}^2\mathcal{L}^2\dot{r}_p}{r_p f_p^2}K + \left[-\frac{im\mathcal{E}\mathcal{L}^3}{r_p^2 f_p} + \frac{l(l+1)\mathcal{E}^2\mathcal{L}^2\dot{r}_p}{2r_p f_p^2}\right]G, \tag{C2}$$

$$f_2^t = \frac{\mathcal{L}^2(f_p - \mathcal{E}^2)}{r_p^2 f_p^2}j_t - \frac{\mathcal{E}^2\mathcal{L}^2\dot{r}_p}{r_p^2 f_p^2}j_r + \left[-\frac{5im\mathcal{E}\mathcal{L}^3}{4r_p^2 f_p} + \frac{\mathcal{E}^2\mathcal{L}^2\dot{r}_p}{r_p f_p^2}\right]G - \frac{\mathcal{L}^2(f_p + \mathcal{E}^2)}{4f_p^2}\partial_t G - \frac{\mathcal{E}^2\mathcal{L}^2\dot{r}_p}{4f_p^2}\partial_r G, \tag{C3}$$

$$f_3^t = \frac{im\mathcal{E}\mathcal{L}^3}{4r_p^2 f_p}G + \frac{\mathcal{L}^2(f_p + \mathcal{E}^2)}{4f_p^2}\partial_t G + \frac{\mathcal{E}^2\mathcal{L}^2\dot{r}_p}{4f_p^2}\partial_r G, \tag{C4}$$

$$f_4^t = \frac{im\mathcal{L}^2(\mathcal{E}^2 - f_p)}{r_p^2 f_p^2}h_t + \frac{im\mathcal{E}^2\mathcal{L}^2\dot{r}_p}{r_p^2 f_p^2}h_r - \left[\frac{m^2\mathcal{E}\mathcal{L}^3}{r_p^4 f_p} + \frac{2im\mathcal{E}^2\mathcal{L}^2\dot{r}_p}{r_p^3 f_p^2}\right]h_2 + \frac{im\mathcal{L}^2(f_p + \mathcal{E}^2)}{2r_p^2 f_p^2}\partial_t h_2 + \frac{im\mathcal{E}^2\mathcal{L}^2\dot{r}_p}{2r_p^2 f_p^2}\partial_r h_2, \tag{C5}$$

$$f_5^t = \frac{\mathcal{E}\mathcal{L}(\mathcal{E}^2 f_p - 2f_p^2 + \mathcal{E}^2)\dot{r}_p}{r_p f_p^4}h_t - \frac{\mathcal{E}^3\mathcal{L}}{f_p^3}\partial_t h_t + \frac{\mathcal{E}\mathcal{L}(f_p - \mathcal{E}^2)\dot{r}_p}{f_p^3}\partial_r h_t + \frac{\mathcal{E}\mathcal{L}(-5f_p U_p^2 + 4\mathcal{E}^2 f_p + U_p^2)}{2r_p f_p^2}h_r$$

$$- \frac{\mathcal{E}\mathcal{L}(f_p + \mathcal{E}^2)\dot{r}_p}{f_p^3}\partial_t h_r + \frac{\mathcal{E}\mathcal{L}(U_p^2 - \mathcal{E}^2)}{f_p}\partial_r h_r - \frac{(m^2 - 1)\mathcal{E}\mathcal{L}^3}{2r_p^4 f_p}h_2, \tag{C6}$$

$$f_6^t = -\frac{\mathcal{E}\mathcal{L}^3}{r_p^3}h_r - \frac{\mathcal{E}\mathcal{L}^3}{2r_p^4 f_p}h_2, \tag{C7}$$

$$f_7^t = -\frac{\mathcal{E}\mathcal{L}^3}{2r_p^4 f_p}h_2, \tag{C8}$$

$$f_0^r = \left[ \frac{M(\mathcal{E}^2 f_p - f_p^2 - (5\mathcal{E}^2 - U_p^2)U_p^2 + 4\mathcal{E}^4)}{2f_p^3} - \frac{im\mathcal{E}\mathcal{L}(f_p - U_p^2 + 2\mathcal{E}^2)\dot{r}_p}{4f_p^3} \right] h_{tt} - \frac{r_p^2 \mathcal{E}^2 (f_p - U_p^2 + 2\mathcal{E}^2)\dot{r}_p}{4f_p^4} \partial_t h_{tt}$$

$$+ \frac{r_p^2(\mathcal{E}^2 f_p + f_p^2 + (3\mathcal{E}^2 - U_p^2)U_p^2 - 2\mathcal{E}^4)}{4f_p^2} \partial_r h_{tt}$$

$$+ \left[ -\frac{M(-f_p(2U_p^2 + \mathcal{E}^2) + f_p^2 + (U_p^2 - \mathcal{E}^2)U_p^2)}{2f_p} - \frac{im\mathcal{E}\mathcal{L}(3f_p - U_p^2 + 2\mathcal{E}^2)\dot{r}_p}{4f_p} \right] h_{rr}$$

$$- \frac{r_p^2 \mathcal{E}^2 (3f_p - U_p^2 + 2\mathcal{E}^2)\dot{r}_p}{4f_p^2} \partial_t h_{rr} + \frac{r_p^2(2f_p U_p^2 - \mathcal{E}^2 f_p - f_p^2 + (3\mathcal{E}^2 - U_p^2)U_p^2 - 2\mathcal{E}^4)}{4} \partial_r h_{rr}$$

$$+ \left[ \frac{im\mathcal{E}\mathcal{L}(U_p^2 - \mathcal{E}^2 - f_p)}{f_p} + \frac{M\mathcal{E}^2(2f_p - U_p^2 + 2\mathcal{E}^2)\dot{r}_p}{f_p^3} \right] h_{tr} - \frac{r_p^2 \mathcal{E}^2(f_p - U_p^2 + \mathcal{E}^2)}{f_p^2} \partial_t h_{tr}$$

$$+ \frac{r_p^2 \mathcal{E}^2(U_p^2 - \mathcal{E}^2)\dot{r}_p}{f_p^2} \partial_r h_{tr} + \left[ \frac{im\mathcal{E}\mathcal{L}(f_p + 1)(\mathcal{E}^2 - U_p^2)}{r_p f_p^2} + \frac{m^2 \mathcal{E}^2 \mathcal{L}^2 \dot{r}_p}{r_p^2 f_p^2} \right] j_t - \frac{im\mathcal{E}^3 \mathcal{L}\dot{r}_p}{f_p^3} \partial_t j_t$$

$$+ \frac{im\mathcal{E}\mathcal{L}(f_p + U_p^2 - \mathcal{E}^2)}{f_p} \partial_r j_t + \left[ \frac{m^2 \mathcal{L}^2(f_p - U_p^2 + \mathcal{E}^2)}{r_p^2} + \frac{im\mathcal{E}\mathcal{L}(-5f_p U_p^2 + 4\mathcal{E}^2 f_p + 4f_p^2 + U_p^2)\dot{r}_p}{2r_p f_p^2} \right] j_r$$

$$- \frac{im\mathcal{E}\mathcal{L}(f_p - U_p^2 + \mathcal{E}^2)}{f_p} \partial_t j_r - \frac{im\mathcal{E}\mathcal{L}(\mathcal{E}^2 - U_p^2)\dot{r}_p}{f_p} \partial_r j_r + \frac{im\mathcal{E}\mathcal{L}(f_p - U_p^2)\dot{r}_p}{2f_p^2} K + \frac{r_p^2 \mathcal{E}^2 (f_p - U_p^2)\dot{r}_p}{2f_p^3} \partial_t K$$

$$- \frac{r_p^2(f_p - U_p^2)(f_p + U_p^2 - \mathcal{E}^2)}{2f_p} \partial_r K + \left[ -\frac{m^2 \mathcal{L}^2(f_p - U_p^2 + \mathcal{E}^2)}{r_p} + \frac{im(m^2 + 4)\mathcal{E}\mathcal{L}^3 \dot{r}_p}{4r_p^2 f_p} \right] G + \frac{m^2 \mathcal{E}^2 \mathcal{L}^2 \dot{r}_p}{4f_p^2} \partial_t G$$

$$- \frac{m^2 \mathcal{L}^2(f_p + U_p^2 - \mathcal{E}^2)}{4} \partial_r G, \tag{C9}$$

$$f_1^r = \left[ -\frac{M\mathcal{L}^2(f_p + U_p^2 - \mathcal{E}^2)}{2r_p^2 f_p^2} - \frac{im\mathcal{E}\mathcal{L}^3 \dot{r}_p}{4r_p^2 f_p^2} \right] h_{tt} - \frac{\mathcal{E}^2 \mathcal{L}^2 \dot{r}_p}{4f_p^3} \partial_t h_{tt} + \frac{\mathcal{L}^2(f_p + U_p^2 - \mathcal{E}^2)}{4f_p} \partial_r h_{tt}$$

$$+ \left[ \frac{\mathcal{L}^2(5f_p(U_p^2 - \mathcal{E}^2) - 3f_p^2 - f_p - U_p^2 + \mathcal{E}^2)}{4r_p} + \frac{im\mathcal{E}\mathcal{L}^3 \dot{r}_p}{4r_p^2} \right] h_{rr} + \frac{\mathcal{E}^2 \mathcal{L}^2 \dot{r}_p}{4f_p} \partial_t h_{rr} - \frac{\mathcal{L}^2 f_p(f_p + U_p^2 - \mathcal{E}^2)}{4} \partial_r h_{rr}$$

$$- \frac{\mathcal{E}^2 \mathcal{L}^2 \dot{r}_p}{r_p f_p} h_{tr} - \frac{im\mathcal{E}\mathcal{L}^3 \dot{r}_p}{r_p^3} j_r + \frac{\mathcal{L}^2(f_p - U_p^2 + \mathcal{E}^2)}{r_p} K + \left[ \frac{l(l+1)\mathcal{L}^2(f_p - U_p^2 + \mathcal{E}^2)}{2r_p} - \frac{im\mathcal{E}\mathcal{L}^3 \dot{r}_p}{r_p^2 f_p} \right] G, \tag{C10}$$

$$f_2^r = -\frac{\mathcal{E}^2 \mathcal{L}^2 \dot{r}_p}{r_p^2 f_p^2} j_t - \frac{\mathcal{L}^2(f_p - U_p^2 + \mathcal{E}^2)}{r_p^2} j_r + \left[ \frac{\mathcal{L}^2(f_p - U_p^2 + \mathcal{E}^2)}{r_p} - \frac{5im\mathcal{E}\mathcal{L}^3 \dot{r}_p}{4r_p^2 f_p} \right] G - \frac{\mathcal{E}^2 \mathcal{L}^2 \dot{r}_p}{4f_p^2} \partial_t G + \frac{\mathcal{L}^2(f_p + U_p^2 - \mathcal{E}^2)}{4} \partial_r G, \tag{C11}$$

$$f_3^r = \frac{im\mathcal{E}\mathcal{L}^3 \dot{r}_p}{4r_p^2 f_p} G + \frac{\mathcal{E}^2 \mathcal{L}^2 \dot{r}_p}{4f_p^2} \partial_t G - \frac{\mathcal{L}^2(f_p + U_p^2 - \mathcal{E}^2)}{4} \partial_r G, \tag{C12}$$

$$f_4^r = \frac{im\mathcal{E}^2 \mathcal{L}^2 \dot{r}_p}{r_p^2 f_p^2} h_t + \frac{im\mathcal{L}^2(f_p - U_p^2 + \mathcal{E}^2)}{r_p^2} h_r + \left[ \frac{2im\mathcal{L}^2(U_p^2 - \mathcal{E}^2)}{r_p^3} - \frac{m^2 \mathcal{E}\mathcal{L}^3 \dot{r}_p}{r_p^4 f_p} \right] h_2 + \frac{im\mathcal{E}^2 \mathcal{L}^2 \dot{r}_p}{2r_p^2 f_p^2} \partial_t h_2 - \frac{im\mathcal{L}^2(f_p + U_p^2 - \mathcal{E}^2)}{2r_p^2} \partial_r h_2, \tag{C13}$$

$$f_5^r = \frac{\mathcal{E}\mathcal{L}(f_p + 1)(\mathcal{E}^2 - U_p^2)}{r_p f_p^2} h_t - \frac{\mathcal{E}^3 \mathcal{L}\dot{r}_p}{f_p^3} \partial_t h_t + \frac{\mathcal{E}\mathcal{L}(f_p + U_p^2 - \mathcal{E}^2)}{f_p} \partial_r h_t - \frac{\mathcal{E}\mathcal{L}(5f_p U_p^2 - 4\mathcal{E}^2 f_p - 4f_p^2 - U_p^2)\dot{r}_p}{2r_p f_p^2} h_r$$

$$- \frac{\mathcal{E}\mathcal{L}(f_p - U_p^2 + \mathcal{E}^2)}{f_p} \partial_t h_r + \frac{\mathcal{E}\mathcal{L}(U_p^2 - \mathcal{E}^2)\dot{r}_p}{f_p} \partial_r h_r - \frac{(m^2 - 1)\mathcal{E}\mathcal{L}^3 \dot{r}_p}{2r_p^4 f_p} h_2, \tag{C14}$$

$$f_6^r = -\frac{\mathcal{E}\mathcal{L}^3 \dot{r}_p}{r_p^3} h_r - \frac{\mathcal{E}\mathcal{L}^3 \dot{r}_p}{2r_p^4 f_p} h_2, \tag{C15}$$

$$f_7^r = -\frac{\mathcal{E}\mathcal{L}^3 \dot{r}_p}{2r_p^4 f_p} h_2. \tag{C16}$$

## APPENDIX D: ADDITIONAL SELF-FORCE VALUES

The following two tables (Tables VI and VII provide GSF data that complements that presented in Tables III and IV

TABLE VI.   Same as Table III with $e = 0.3$.

|   | $\chi$ | $p = 10$ | $p = 20$ | $p = 30$ | $p = 60$ | $p = 90$ |
|---|---|---|---|---|---|---|
| | 0 | $-1.02425 \times 10^{-3}$ | $-2.195889 \times 10^{-5}$ | $-2.619956 \times 10^{-6}$ | $-7.6424003 \times 10^{-8}$ | $-9.94261928 \times 10^{-9}$ |
| | $\pi/4$ | $7.93725 \times 10^{-4}$ | $2.611011 \times 10^{-4}$ | $1.056357 \times 10^{-4}$ | $2.0516060 \times 10^{-5}$ | $7.66603327 \times 10^{-6}$ |
| | $\pi/2$ | $1.12072 \times 10^{-3}$ | $2.704049 \times 10^{-4}$ | $1.061464 \times 10^{-4}$ | $2.0147891 \times 10^{-5}$ | $7.47715975 \times 10^{-6}$ |
| $F^t$ | $3\pi/4$ | $5.23325 \times 10^{-4}$ | $1.237182 \times 10^{-4}$ | $4.795782 \times 10^{-5}$ | $8.9766821 \times 10^{-6}$ | $3.31514100 \times 10^{-6}$ |
| | $\pi$ | $2.83617 \times 10^{-7}$ | $-3.146284 \times 10^{-8}$ | $-4.916581 \times 10^{-9}$ | $-1.5203069 \times 10^{-10}$ | $-1.85477251 \times 10^{-11}$ |
| | $5\pi/4$ | $-5.01242 \times 10^{-4}$ | $-1.234054 \times 10^{-4}$ | $-4.792378 \times 10^{-5}$ | $-8.9756562 \times 10^{-6}$ | $-3.31499843 \times 10^{-6}$ |
| | $3\pi/2$ | $-1.05385 \times 10^{-3}$ | $-2.698687 \times 10^{-4}$ | $-1.061119 \times 10^{-4}$ | $-2.0147281 \times 10^{-5}$ | $-7.47706856 \times 10^{-6}$ |
| | $7\pi/4$ | $-1.52944 \times 10^{-3}$ | $-2.782552 \times 10^{-4}$ | $-1.077562 \times 10^{-4}$ | $-2.0579481 \times 10^{-5}$ | $-7.67431383 \times 10^{-6}$ |
| | 0 | $2.30316 \times 10^{-2}$ | $6.836866 \times 10^{-3}$ | $3.254304 \times 10^{-3}$ | $8.7346506 \times 10^{-4}$ | $3.97631238 \times 10^{-4}$ |
| | $\pi/4$ | $2.10318 \times 10^{-2}$ | $6.042486 \times 10^{-3}$ | $2.859673 \times 10^{-3}$ | $7.6346290 \times 10^{-4}$ | $3.46940757 \times 10^{-4}$ |
| | $\pi/2$ | $1.41875 \times 10^{-2}$ | $4.215713 \times 10^{-3}$ | $1.985131 \times 10^{-3}$ | $5.2535511 \times 10^{-4}$ | $2.37910729 \times 10^{-4}$ |
| $F^r$ | $3\pi/4$ | $8.91644 \times 10^{-3}$ | $2.676966 \times 10^{-3}$ | $1.253239 \times 10^{-3}$ | $3.2907620 \times 10^{-4}$ | $1.48590757 \times 10^{-4}$ |
| | $\pi$ | $7.11090 \times 10^{-3}$ | $2.131279 \times 10^{-3}$ | $9.953187 \times 10^{-4}$ | $2.6059554 \times 10^{-4}$ | $1.17547270 \times 10^{-4}$ |
| | $5\pi/4$ | $8.70369 \times 10^{-3}$ | $2.669408 \times 10^{-3}$ | $1.252041 \times 10^{-3}$ | $3.2902233 \times 10^{-4}$ | $1.48581907 \times 10^{-4}$ |
| | $3\pi/2$ | $1.30565 \times 10^{-2}$ | $4.179240 \times 10^{-3}$ | $1.979557 \times 10^{-3}$ | $5.2511220 \times 10^{-4}$ | $2.37871148 \times 10^{-4}$ |
| | $7\pi/4$ | $1.86761 \times 10^{-2}$ | $5.972195 \times 10^{-3}$ | $2.849306 \times 10^{-3}$ | $7.6302517 \times 10^{-4}$ | $3.46870034 \times 10^{-4}$ |

TABLE VII.   Same as Table III with $e = 0.7$.

|   | $\chi$ | $p = 10$ | $p = 20$ | $p = 30$ | $p = 60$ | $p = 90$ |
|---|---|---|---|---|---|---|
| | 0 | $-1.12 \times 10^{-2}$ | $-2.101 \times 10^{-4}$ | $-2.3435 \times 10^{-5}$ | $-6.4473 \times 10^{-7}$ | $-1.97 \times 10^{-7}$ |
| | $\pi/4$ | $6.33 \times 10^{-3}$ | $9.829 \times 10^{-4}$ | $3.7436 \times 10^{-4}$ | $7.1857 \times 10^{-5}$ | $2.68 \times 10^{-5}$ |
| | $\pi/2$ | $3.53 \times 10^{-3}$ | $6.765 \times 10^{-4}$ | $2.5715 \times 10^{-4}$ | $4.7747 \times 10^{-5}$ | $1.76 \times 10^{-5}$ |
| | $3\pi/4$ | $6.28 \times 10^{-4}$ | $1.300 \times 10^{-4}$ | $4.8732 \times 10^{-5}$ | $8.8491 \times 10^{-6}$ | $3.24 \times 10^{-6}$ |
| $F^t$ | $\pi$ | $9.81 \times 10^{-8}$ | $1.933 \times 10^{-9}$ | $2.2050 \times 10^{-10}$ | $6.4536 \times 10^{-12}$ | $-3.01 \times 10^{-11}$ |
| | $5\pi/4$ | $-6.10 \times 10^{-4}$ | $-1.296 \times 10^{-4}$ | $-4.8678 \times 10^{-5}$ | $-8.8474 \times 10^{-6}$ | $-3.24 \times 10^{-6}$ |
| | $3\pi/2$ | $-2.15 \times 10^{-3}$ | $-6.524 \times 10^{-4}$ | $-2.5435 \times 10^{-4}$ | $-4.7665 \times 10^{-5}$ | $-1.76 \times 10^{-5}$ |
| | $7\pi/4$ | $-6.48 \times 10^{-3}$ | $-9.957 \times 10^{-4}$ | $-3.7692 \times 10^{-4}$ | $-7.1956 \times 10^{-5}$ | $-2.68 \times 10^{-5}$ |
| | 0 | $5.24 \times 10^{-2}$ | $1.185 \times 10^{-2}$ | $5.5084 \times 10^{-3}$ | $1.4758 \times 10^{-3}$ | $6.74 \times 10^{-4}$ |
| | $\pi/4$ | $4.66 \times 10^{-2}$ | $9.581 \times 10^{-3}$ | $4.3877 \times 10^{-3}$ | $1.1591 \times 10^{-3}$ | $5.27 \times 10^{-4}$ |
| | $\pi/2$ | $1.62 \times 10^{-2}$ | $4.435 \times 10^{-3}$ | $2.0476 \times 10^{-3}$ | $5.3292 \times 10^{-4}$ | $2.40 \times 10^{-4}$ |
| $F^r$ | $3\pi/4$ | $4.22 \times 10^{-3}$ | $1.180 \times 10^{-3}$ | $5.3937 \times 10^{-4}$ | $1.3833 \times 10^{-4}$ | $6.20 \times 10^{-5}$ |
| | $\pi$ | $1.55 \times 10^{-3}$ | $4.224 \times 10^{-4}$ | $1.9202 \times 10^{-4}$ | $4.9022 \times 10^{-5}$ | $2.19 \times 10^{-5}$ |
| | $5\pi/4$ | $4.19 \times 10^{-3}$ | $1.179 \times 10^{-3}$ | $5.3905 \times 10^{-4}$ | $1.3832 \times 10^{-4}$ | $6.20 \times 10^{-5}$ |
| | $3\pi/2$ | $1.35 \times 10^{-2}$ | $4.348 \times 10^{-3}$ | $2.0342 \times 10^{-3}$ | $5.3232 \times 10^{-4}$ | $2.40 \times 10^{-4}$ |
| | $7\pi/4$ | $2.68 \times 10^{-2}$ | $9.061 \times 10^{-3}$ | $4.3148 \times 10^{-3}$ | $1.1561 \times 10^{-3}$ | $5.26 \times 10^{-4}$ |

[1] T. W. Baumgarte and S. L. Shapiro, *Numerical Relativity: Solving Einstein's Equations on the Computer* (Cambridge University Press, Cambridge, England, 2010).

[2] L. Lehner and F. Pretorius, Annu. Rev. Astron. Astrophys. **52**, 661 (2014).

[3] L. Blanchet, Living Rev. Relativity **17**, 2 (2014).

[4] L. Barack, Classical Quantum Gravity **26**, 213001 (2009).

[5] E. Poisson, A. Pound, and I. Vega, Living Rev. Relativity **14**, 7 (2011).

[6] P. Amaro-Seoane, B. Schutz, and J. Thornburg, GW Notes, Vol. **5**, pp. 3–53, http://brownbag.lisascience.org/files/2011/02/GW_Notes_Number_05.pdf.

[7] A. Buonanno and T. Damour, Phys. Rev. D **59**, 084006 (1999).

[8] A. Buonanno, Y. Pan, H. P. Pfeiffer, M. A. Scheel, L. T. Buchman, and L. E. Kidder, Phys. Rev. D **79**, 124028 (2009).

[9] T. Damour, Phys. Rev. D **81**, 024017 (2010).

[10] Y. Mino, M. Sasaki, and T. Tanaka, Phys. Rev. D **55**, 3457 (1997).

[11] T. C. Quinn and R. M. Wald, Phys. Rev. D **56**, 3381 (1997).

[12] S. E. Gralla, Phys. Rev. D **85**, 124011 (2012).

[13] A. Pound, Phys. Rev. Lett. **109**, 051101 (2012).

[14] L. Barack and A. Ori, Phys. Rev. D **61**, 061502 (2000).

[15] S. L. Detweiler and B. F. Whiting, Phys. Rev. D **67**, 024025 (2003).

[16] S. E. Gralla and R. M. Wald, Classical Quantum Gravity **25**, 205009 (2008).

[17] A. Pound, Phys. Rev. D **81**, 024023 (2010).

[18] P. Amaro-Seoane *et al.*, GW Notes **6**, 4 (2013).

[19] NASA, http://lisa.nasa.gov.

[20] European Space Agency, http://sci.esa.int/science-e/www/object/index.cfm?fobjectid=48728.

[21] M. C. Miller and E. J. M. Colbert, Int. J. Mod. Phys. D **13**, 1 (2004).

[22] D. A. Brown, J. Brink, H. Fang, J. R. Gair, C. Li, G. Lovelace, I. Mandel, and K. S. Thorne, Phys. Rev. Lett. **99**, 201102 (2007).

[23] P. Amaro-Seoane, J. R. Gair, M. Freitag, M. C. Miller, I. Mandel, C. J. Cutler, and S. Babak, Classical Quantum Gravity **24**, R113 (2007).

[24] S. J. Vigeland and S. A. Hughes, Phys. Rev. D **81**, 024030 (2010).

[25] L. Barack and C. Cutler, Phys. Rev. D **75**, 042003 (2007).

[26] K. Martel, Phys. Rev. D **69**, 044025 (2004).

[27] L. Barack and N. Sago, Phys. Rev. D **75**, 064021 (2007).

[28] S. E. Field, J. S. Hesthaven, and S. R. Lau, Classical Quantum Gravity **26**, 165010 (2009).

[29] P. Canizares and C. F. Sopuerta, arXiv:1406.7154.

[30] S. Detweiler, Phys. Rev. D **77**, 124026 (2008).

[31] S. Hopper and C. R. Evans, Phys. Rev. D **82**, 084010 (2010).

[32] S. Akcay, Phys. Rev. D **83**, 124026 (2011).

[33] L. Barack and N. Sago, Phys. Rev. Lett. **102**, 191101 (2009).

[34] L. Barack and N. Sago, Phys. Rev. D **81**, 084021 (2010).

[35] L. Barack and N. Sago, Phys. Rev. D **83**, 084023 (2011).

[36] N. Warburton, S. Akcay, L. Barack, J. R. Gair, and N. Sago, Phys. Rev. D **85**, 061501 (2012).

[37] S. Akcay, N. Warburton, and L. Barack, Phys. Rev. D **88**, 104009 (2013).

[38] S. Detweiler, E. Messaritaki, and B. F. Whiting, Phys. Rev. D **67**, 104016 (2003).

[39] R. Haas, Phys. Rev. D **75**, 124011 (2007).

[40] L. Barack, A. Ori, and N. Sago, Phys. Rev. D **78**, 084021 (2008).

[41] L. Barack, D. A. Golbourn, and N. Sago, Phys. Rev. D **76**, 124036 (2007).

[42] N. Warburton and L. Barack, Phys. Rev. D **81**, 084039 (2010).

[43] T. S. Keidl, A. G. Shah, J. L. Friedman, D.-H. Kim, and L. R. Price, Phys. Rev. D **82**, 124012 (2010).

[44] S. R. Dolan, L. Barack, and B. Wardell, Phys. Rev. D **84**, 084001 (2011).

[45] A. G. Shah, J. L. Friedman, and T. S. Keidl, Phys. Rev. D **86**, 084059 (2012).

[46] S. R. Dolan and L. Barack, Phys. Rev. D **87**, 084066 (2013).

[47] S. Isoyama, L. Barack, S. R. Dolan, A. Le Tiec, H. Nakano, A. G. Shah, T. Tanaka, and N. Warburton, arXiv:1404.6133.

[48] N. Warburton, arXiv:1408.2885.

[49] A. Heffernan, A. Ottewill, and B. Wardell, Phys. Rev. D **86**, 104023 (2012).

[50] A. Heffernan, A. Ottewill, and B. Wardell, Phys. Rev. D **89**, 024030 (2014).

[51] R. Fujita, Prog. Theor. Phys. **128**, 971 (2012).

[52] A. G. Shah, J. L. Friedman, and B. F. Whiting, Phys. Rev. D **89**, 064042 (2014).

[53] A. G. Shah, Phys. Rev. D **90**, 044025 (2014).

[54] E. Forseth, C. R. Evans, and S. Hopper (unpublished).

[55] L. Blanchet, S. Detweiler, A. Le Tiec, and B. F. Whiting, Phys. Rev. D **81**, 084033 (2010).

[56] I. Vega and S. Detweiler, Phys. Rev. D **77**, 084008 (2008).

[57] I. Vega, B. Wardell, and P. Diener, Classical Quantum Gravity **28**, 134010 (2011).

[58] B. Wardell, I. Vega, J. Thornburg, and P. Diener, Phys. Rev. D **85**, 104044 (2012).

[59] M. Casals, S. Dolan, A. C. Ottewill, and B. Wardell, Phys. Rev. D **79**, 124043 (2009).

[60] M. Casals, S. Dolan, A. C. Ottewill, and B. Wardell, Phys. Rev. D **88**, 044022 (2013).

[61] B. Wardell, C. R. Galley, A. Zenginoğlu, M. Casals, S. R. Dolan, and A. C. Ottewill, Phys. Rev. D **89**, 084021 (2014).

[62] D. A. Golbourn, Ph.D. thesis, University of Southampton, 2009.

[63] C. R. Evans, T. Osburn, and E. Forseth, in 15th Capra Meeting, University of Maryland, College Park, MD, 2012 (unpublished), http://www2.cscamm.umd.edu/programs/capra12/schedule.php; T. Osburn, in 16th Capra Meeting, University College Dublin, Dublin, Ireland, 2013 (unpublished), http://maths.ucd.ie/capra16/schedule/; E. Forseth, in 16th Capra Meeting, University College Dublin, Dublin, Ireland, 2013 (unpublished), http://maths.ucd.ie/capra16/schedule/; T. Osburn, in 17th Capra Meeting, Caltech, Pasadena, CA, 2014 (unpublished).

[64] L. Barack and C. O. Lousto, Phys. Rev. D **72**, 104026 (2005).
[65] T. Hinderer and E. E. Flanagan, Phys. Rev. D **78**, 064028 (2008).
[66] E. E. Flanagan and T. Hinderer, Phys. Rev. Lett. **109**, 071102 (2012).
[67] M. van de Meent, Phys. Rev. D **90**, 044027 (2014).
[68] E. Poisson, in 5th Capra Meeting on Radiation Reaction in General Relativity, Penn State University, State College, PA, 2002 (unpublished).
[69] E. Rosenthal, Phys. Rev. D **73**, 044034 (2006).
[70] E. Rosenthal, Phys. Rev. D **74**, 084018 (2006).
[71] L. M. Burko and G. Khanna, Phys. Rev. D **88**, 024002 (2013).
[72] P. Diener, I. Vega, B. Wardell, and S. Detweiler, Phys. Rev. Lett. **108**, 191102 (2012).
[73] P. Diener, A. Pound, N. Warburton, and B. Wardell (unpublished).
[74] N. Warburton, in 17th Capra Meeting, Caltech, Pasadena, CA, 2014.
[75] N. Warburton (private communication).
[76] C. Hopman and T. Alexander, Astrophys. J. **629**, 362 (2005).
[77] C. Misner, K. Thorne, and J. Wheeler, *Gravitation* (Freeman, San Francisco, 1973).
[78] K. Martel and E. Poisson, Phys. Rev. D **71**, 104003 (2005).
[79] C. Cutler, D. Kennefick, and E. Poisson, Phys. Rev. D **50**, 3816 (1994).
[80] C. Darwin, Proc. R. Soc. A **249**, 180 (1959).
[81] T. Regge and J. Wheeler, Phys. Rev. **108**, 1063 (1957).
[82] L. Barack, Y. Mino, H. Nakano, A. Ori, and M. Sasaki, Phys. Rev. Lett. **88**, 091101 (2002).
[83] Y. Mino, Phys. Rev. D **67**, 084027 (2003).
[84] N. Warburton and L. Barack, Phys. Rev. D **83**, 124038 (2011).
[85] S. Hopper and C. R. Evans, Phys. Rev. D **87**, 064008 (2013).
[86] L. Barack, in 15th Capra Meeting, University of Maryland, College Park, MD, 2012, http://www2.cscamm.umd.edu/programs/capra12/schedule.php.
[87] N. Warburton, in 15th Capra Meeting, University of Maryland, College Park, MD, 2012, http://www2.cscamm.umd.edu/programs/capra12/schedule.php.
[88] E. Cheney and D. Kincaid, *Numerical Mathematics and Computing* (Cengage Learning, Toebben Drive, 2012).
[89] G. Golub and C. Van Loan, *Matrix Computations* (Johns Hopkins University Press, Baltimore, MD, 1996).
[90] P. Prince and J. Dormand, J. Comput. Appl. Math. **7**, 67 (1981).
[91] GNU scientific library, http://www.gnu.org/software/gsl/.
[92] W. H. Press, S. A. Teukolsky, W. T. Vetterling, and B. P. Flannery, *Numerical Recipes in C: The Art of Scientific Computing*, 2nd ed. (Cambridge University Press, Cambridge, England, 1993).
[93] P. Nolan, A. Ottewill, and N. Warburton (private communication).
[94] C. Cunningham, R. Price, and V. Moncrief, Astrophys. J. **224**, 643 (1978).
[95] S. Chandrasekhar, Proc. R. Soc. A **343**, 289 (1975).
[96] S. Chandrasekhar and S. Detweiler, Proc. R. Soc. A **345**, 145 (1975).
[97] S. Chandrasekhar, *The Mathematical Theory of Black Holes*, The International Series of Monographs on Physics, Vol. 69 (Clarendon, Oxford, 1983).
[98] F. Zerilli, Phys. Rev. D **2**, 2141 (1970).
[99] S. L. Detweiler and E. Poisson, Phys. Rev. D **69**, 084019 (2004).
[100] M. Berndston, Ph.D. thesis, University of Colorado, 2007, arXiv:0904.0033v1.
[101] N. Sago, L. Barack, and S. L. Detweiler, Phys. Rev. D **78**, 124024 (2008).
[102] R. Fujita, W. Hikida, and H. Tagoshi, Prog. Theor. Phys. **121**, 843 (2009).
[103] A. Pound and E. Poisson, Phys. Rev. D **77**, 044013 (2008).
[104] A. Pound, Phys. Rev. D **86**, 084019 (2012).
[105] N. Warburton and B. Wardell, Phys. Rev. D **89**, 044046 (2014).
[106] S. R. Dolan, N. Warburton, A. I. Harte, A. Le Tiec, B. Wardell, and L. Barack, Phys. Rev. D **89**, 064011 (2014).
[107] S. R. Dolan, P. Nolan, A. C. Ottewill, N. Warburton, and B. Wardell, arXiv:1406.4890.